# THE ATMOSPHERE ABOVE MAUNA KEA AT MID-INFRARED WAVELENGTHS

IAN MYLES CHAPMAN

**B. Sc. Physics, University of Alberta, 2000**

A Thesis
Submitted to the School of Graduate Studies
of the University of Lethbridge
in Partial Fulfilment of the
Requirements of the Degree

**MASTER OF SCIENCE**

Department of Physics
LETHBRIDGE, ALBERTA, CANADA

**Dedication**

To Cork,

whose love and patience gave me strength,

and to Natalie,

for being so kind to your Daddy during those last days of writing.

## Abstract

The performance of astronomical interferometer arrays operating at (sub)millimeter wavelengths is seriously compromised by rapid variations of atmospheric water vapour content that distort the phase coherence of incoming celestial signals. Unless corrected, these phase distortions, which vary rapidly with time and from antenna to antenna, seriously compromise the sensitivity and image quality of these arrays. Building on the success of a prototype infrared radiometer for millimeter astronomy (IRMA I), which was used to measure atmospheric water vapour column abundance, this thesis presents results from a second generation radiometer (IRMA II) operating at the James Clerk Maxwell Telescope (JCMT) on Mauna Kea, Hawaii from December, 2000 to March, 2001. These results include comparisons with other measures of water vapour abundance available on the summit of Mauna Kea and a comparison with a theoretical curve-of-growth calculated from a new radiative transfer model, ULTRAM, developed specifically for the purpose. Plans for a third generation radiometer (IRMA III) are also be discussed.

## Acknowledgements

I would like to thank David Naylor for taking a chance on a stranger and offering me IRMA as a thesis project. I am also grateful for, among many other things, his patience and guidance as I spent time familiarizing myself with the project and with the IDL programming language. Thank you also for the hours and hours of proof-reading, despite being so busy with the new projects. I am especially grateful for being able to spend so much time with my daughter during the first few weeks of her life.

I would also like to thank the following people:

Graeme Smith - for leaving the IRMA project in such great shape for me to pick up, and for all of his hard work on his thesis, on which much of mine was based.

Brad Gom - for imparting to me some of his vast knowledge of IDL.

Ian Schofield - for his help with bagging all of the IRMA data, and for his computer expertise in general.

Dr. Lorne Avery - for inviting me to come work with him in Victoria, and for his help in getting ULTRAM up and running.

Greg Tompkins - for all of his work on the IRMA project, and for keeping some humour in the group.

Alexandra Pope - for allowing me to borrow some of her early programs.

Dr. Jim Chetwynd - for providing me with the latest version of FASCODE.

Dr. S. Anthony Clough - for sharing his expertise in radiative transfer modelling.

Dr. David Siminovitch and Dr. Rene Boere - for their assistance as members of my supervisory committee.

Dr. Arvid Schultz - for his help around the lab, and for his assistance as a proof-reader.

I would also like to thank the Director and staff of the JCMT for all of their assistance in operating IRMA at the JCMT.

I am especially grateful for the financial support of NSERC and the University of Lethbridge.

# Contents

# List of Figures

# List of Tables

# Chapter 1

# Introduction

## 1.1 Overview

Within the next decade a number of large baseline, submillimeter wavelength interferometers, such as the Atacama Large Millimeter Array (ALMA), which will be deployed on the Chajnantor plateau in the high Chilean Andes (altitude $\simeq$ 5000 m), will begin operating. These interferometers will provide imaging capabilities in the 10 milliarcsecond range when operating at their highest frequencies. The principle of interferometry, which governs the operation of these telescopes, requires that the time delay between the reception of the electromagnetic wavefronts arriving at antennae composing the array be measured accurately.

Electronic instrumentation has advanced to the point where the spatial resolution of a modern radio interferometer is limited by variations in electromagnetic path length

caused by atmospheric inhomogeneities. At (sub)millimeter wavelengths the main contributing factor to these path length variations is the variable line-of-sight atmospheric water vapour content. If the line-of-sight water vapour content can be measured accurately, then, in principle, these path length variations can be determined and used to correct the associated phase error of the wavefront received at each antenna.

There are a number of techniques already used in atmospheric phase correction. Two of these techniques are known as *fast switching* and *paired array*. In the fast switching technique [3], radio antennae are repeatedly moved from pointing at an astronomical source to pointing at a nearby calibration source such as a quasar. Observed deviations of the calibration source from the expected circular symmetry of the Airy diffraction profile are due to atmospheric phase errors which can be determined and compensated for in the signal from the astronomical source. The main advantage of this technique is that it gives a true measure of the phase error at each antenna since a quasar is known to be a point source. There are also several drawbacks to this technique: calibration measurements are made along different lines-of-sight than those of the astronomical source, thereby sampling different portions of the atmosphere which may contain different amounts of water vapour. Secondly, observations of the astronomical source must be interrupted by the calibration measurements, reducing the effective observing efficiency. Thirdly, since calibration sources will not, in general, be located close to astronomical sources, the fast switching technique results in long calibration cycles during which time it is implicitly assumed that the atmosphere is stable.

In the paired array technique [3], calibration is performed at the same time as

the observation of the astronomical source. Several antennae in the array continuously observe the calibration source while the remainder of the antennae are used to observe the astronomical source. This technique has the advantage over the fast switching technique of avoiding frequent interruptions of astronomical source observations. The paired array technique suffers from the same drawback as the fast switching technique, namely calibrating along different lines-of-sight than those of the astronomical source. Moreover, since the calibration measurements involve a small number of antennae, the phase correction that has to be applied to antennae observing the astronomical source must be extrapolated from this limited subset of calibration data. To be effective, this extrapolation again requires that the atmosphere be stable and can be well-modeled over the large area of the array, which is, in general, unlikely to be the case. A major financial drawback to this technique is the high cost of devoting several antennae (~$10 million) to calibration measurements.

A more recent method used to compensate for water vapour induced phase delay is to equip each antenna with a multi-channel radiometer observing the 183 GHz water vapour spectral line [4]. This technique offers the advantage of simultaneously observing the astronomical source at one frequency and atmospheric water vapour at 183 GHz along the same line-of-sight as the astronomical source. There are two main drawbacks to this technique. The first drawback is the presence of a local oscillator in the multi-channel radiometer which can introduce radio frequency (rf) noise into the telescope receiver cabin where it may interfere with the sensitive astronomical receivers. The second main drawback is the low flux emitted by this water vapour line (§ 1.3).

This thesis will present and discuss results obtained with an infrared radiometer for

the measurement of atmospheric water vapour, developed at the University of Lethbridge by Mr. Graeme Smith under the direction of Dr. David Naylor [2]. The prototype Infrared Radiometer for Millimeter Astronomy (IRMA) was tested at the James Clerk Maxwell Telescope (JCMT) on Mauna Kea, Hawaii in December of 1999. The infrared radiometer uses a passive mode of observation and thus poses no threat of interference with the sensitive astronomical receivers. It also takes advantage of the higher flux emitted by water vapour in the infrared spectral region (§ 1.3). Analysis of data obtained using the prototype radiometer (IRMA I) showed that this technique held much promise as a method of phase correcting (sub)millimeter interferometric astronomical data [5]. Several upgrades were subsequently made to the instrument, and IRMA II operated at the JCMT from December, 2000 to March, 2001. This thesis will present the analysis of data obtained with IRMA II; a key component of the thesis has been the development of a radiative transfer model of the earth's atmosphere, used to provide a theoretical basis for analyzing the IRMA II data.

The remainder of this introductory chapter addresses the following topics: Section 1.2: Tropospheric Phase Delay explains the cause of phase delay in the atmosphere. Section 1.3: Infrared Radiometer Concept compares and contrasts the infrared and radio frequency methods of atmospheric water vapour measurement. Section 1.4: Phase Compensation Requirements of ALMA discusses the design requirements of the phase compensation for ALMA. Section 1.5: Radiative Transfer modelling discusses the rationale for the development of an atmospheric radiative transfer model. Section 1.6: Summary summarizes the content of individual thesis chapters.

## 1.2 Tropospheric Phase Delay

The troposphere is the lowest layer of the atmosphere, extending from the ground to an altitude of about 10 km. Most of the water vapour in the atmosphere is located in the troposphere. Since the temperature usually decreases with altitude in this layer, most of the water vapour is concentrated in the lower altitudes of the troposphere. However, even above high-altitude sites such as Mauna Kea (4092 m) and Chajnantor, Chile (~5000 m), water vapour exists in sufficient quantities to introduce a significant phase delay into (sub)millimeter astronomical signals.

If water vapour was distributed uniformly in the atmosphere (like the major atmospheric constituents, $N_2$ and $O_2$) then the phase delay of an electromagnetic wave would also be uniform across its wavefront, giving a constant signal phase delay at each antenna in the array. Due to the polar nature of the water molecule, under typical atmospheric temperatures and pressures, water can co-exist in its three states and thus water vapour can be present in varying concentrations in the troposphere. Furthermore, these concentrations can be highly variable over small distances (~m) and short time intervals (~s). This variation of water vapour concentration and hence, phase delay, poses a major problem for the next generation of radio telescope arrays with baselines on the order of 10 km. If the water vapour above each antenna can be measured accurately, then the resulting phase delay can be corrected for, allowing (sub)millimeter interferometers to achieve diffraction-limited performance.

Figure 1.1 illustrates the effect of atmospheric water vapour, represented by the

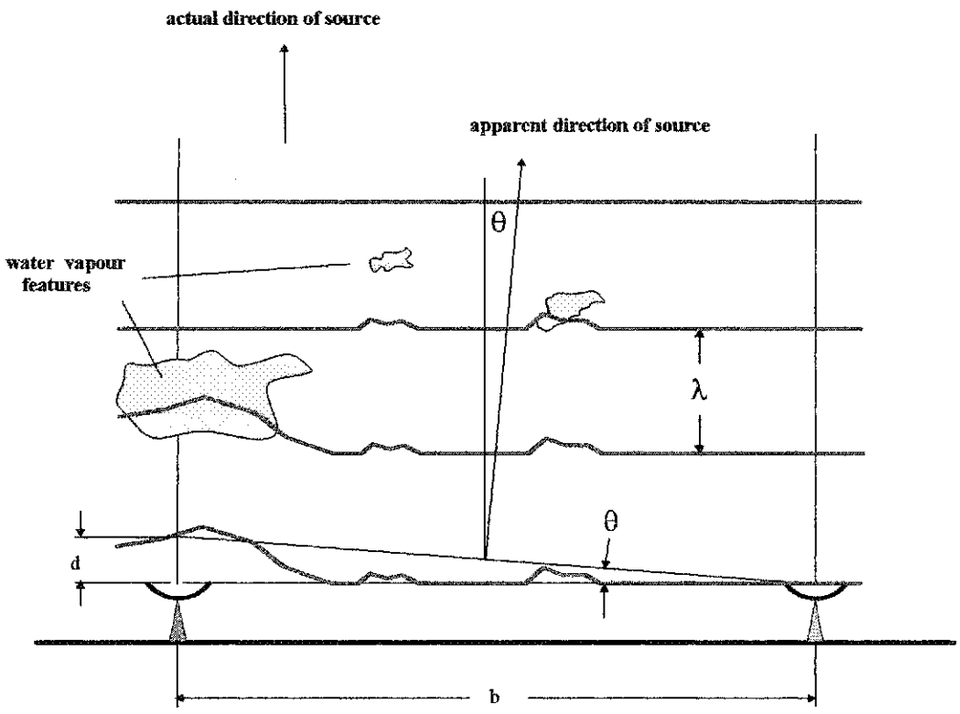


Figure 1.1: Distortion in an electromagnetic wavefront is caused by variations in atmospheric water vapour abundance.

blue clouds, on an electromagnetic wavefront, represented by the red lines, travelling through the atmosphere above two radio interferometer antennae. The apparent angular location of an astronomical source, $\theta$, as determined by the radio interferometer can be expressed in terms of the baseline, $b$, of the interferometer and the additional electromagnetic path length, $d$ in the small-angle expression

$$\theta = \frac{d}{b} \tag{1.1}$$

The angular location can also be expressed in terms of the phase change, $\phi$, caused by water

vapour using the expression

$$\theta = \frac{\phi\lambda}{2\pi b} \tag{1.2}$$

where $\theta$ and $\phi$ are given in radians.

From equations 1.1 and 1.2, the additional path length, $d$, due to water vapour is

$$d = \frac{\lambda\phi}{2\pi} \tag{1.3}$$

Changes in the refractive index of the atmosphere are related to variation in atmospheric water vapour content. The excess path length, $d$, is related to the line-of-sight water vapour abundance, $w$, expressed in units of millimeters of precipitable water vapour (mm pwv) by [3]

$$d = \frac{1.73 \times 10^3}{T_{atm}} \times w \tag{1.4}$$

where $T_{atm}$ is the average temperature of the atmosphere in K. For an atmosphere of average temperature of 260 K, the excess path length is given by

$$d \simeq 6.5 \times w \tag{1.5}$$

From equations 1.3, 1.4, and 1.5, the wavelength dependent phase variation is given by

$$\phi = \frac{13\pi}{\lambda} \times w \tag{1.6}$$

## 1.3 IRMA Concept

In order to make an accurate infrared radiometric measurement of atmospheric water vapour abundance, water vapour must be spectrally isolated from other emitting

species. Previous measurements of atmospheric emission by a Fourier transform spectrometer on the summit of Mauna Kea [1] have shown that the emission in the 20 $\mu$m (500 cm$^{-1}$) spectral region is dominated by water vapour.

There are several factors which make the 20 $\mu$m spectral region an attractive spectral region for the development of a radiometer. First, as was mentioned above, water vapour emission is spectrally isolated in this region. By comparison, the (sub)millimeter region which is observed by instruments such as SCUBA, also contains contributions to emission from species such as ozone and oxygen. Secondly, since strongly absorbing molecules emit as blackbodies, the radiance from water vapour in the infrared region is far greater than that in the (sub)millimeter region, a point emphasized by the fact that the wavelength of 20 $\mu$m is close to the peak of the Planck blackbody function for typical atmospheric temperatures. Thirdly, the large spectral bandpass in the infrared region allows a greater flux of radiation from water vapour emission to be collected by the radiometer. This increase of flux allows for more sensitive measurements, faster operation, smaller instrument size, or a combination thereof. Fourthly, photoconductive detectors operating at infrared wavelengths offer high operating speeds, stability, and simple instrumentation. Finally, an infrared radiometer is a passive device, free of radio frequency interference. This allows IRMA to be placed in close proximity to antennae in an interferometer array without the risk of interference with observations.

The factors discussed above make a powerful case for IRMA as an alternative method of phase correction. IRMA is a sensitive, high speed, and compact device, which can be readily incorporated into both existing and future radio telescope antennae.

### 1.3.1 Infrared Radiometer Advantages

#### Spectral Isolation of Water Vapour Emission

In order to measure radiometrically atmospheric water vapour, it is essential to choose a spectral range where water vapour is the only emitting species. If possible, it is also advantageous to have that spectral region near the peak of the Planck curve in order to maximize sensitivity to changes in water vapour content. Atmospheric emission at infrared wavelengths has been measured above Mauna Kea using a Fourier transform spectrometer over the spectral range 455 to 635 $cm^{-1}$ [1], shown as the lowest curves in figures 1.2, 1.3, and 1.4. The figures also show the simulated emissions from $N_2O$, $CO_2$, and $H_2O$ (upper three curves) modeled for the atmosphere above Mauna Kea. The vertical axes in the figures have arbitrary scales.

Figures 1.2 and 1.3 show that water vapour is the sole contributor to emission in the region from 455 to 520 $cm^{-1}$ and that it is the dominant contributor to emission from 520 to 544 $cm^{-1}$. At 544 $cm^{-1}$ emissions from $N_2O$ and $CO_2$ become increasingly significant until 575 $cm^{-1}$, where emission from $CO_2$ begins to dominate the spectrum. Futhermore, the measured spectrum is well described by the theoretical model. This spectral isolation of water vapour emission in the 455 to 544 $cm^{-1}$ region makes it ideal for the development of a water vapour radiometer.

A second consideration is the saturation of the emission lines in the region. Unsaturated emission lines are the most sensitive to changes in water vapour column abundance

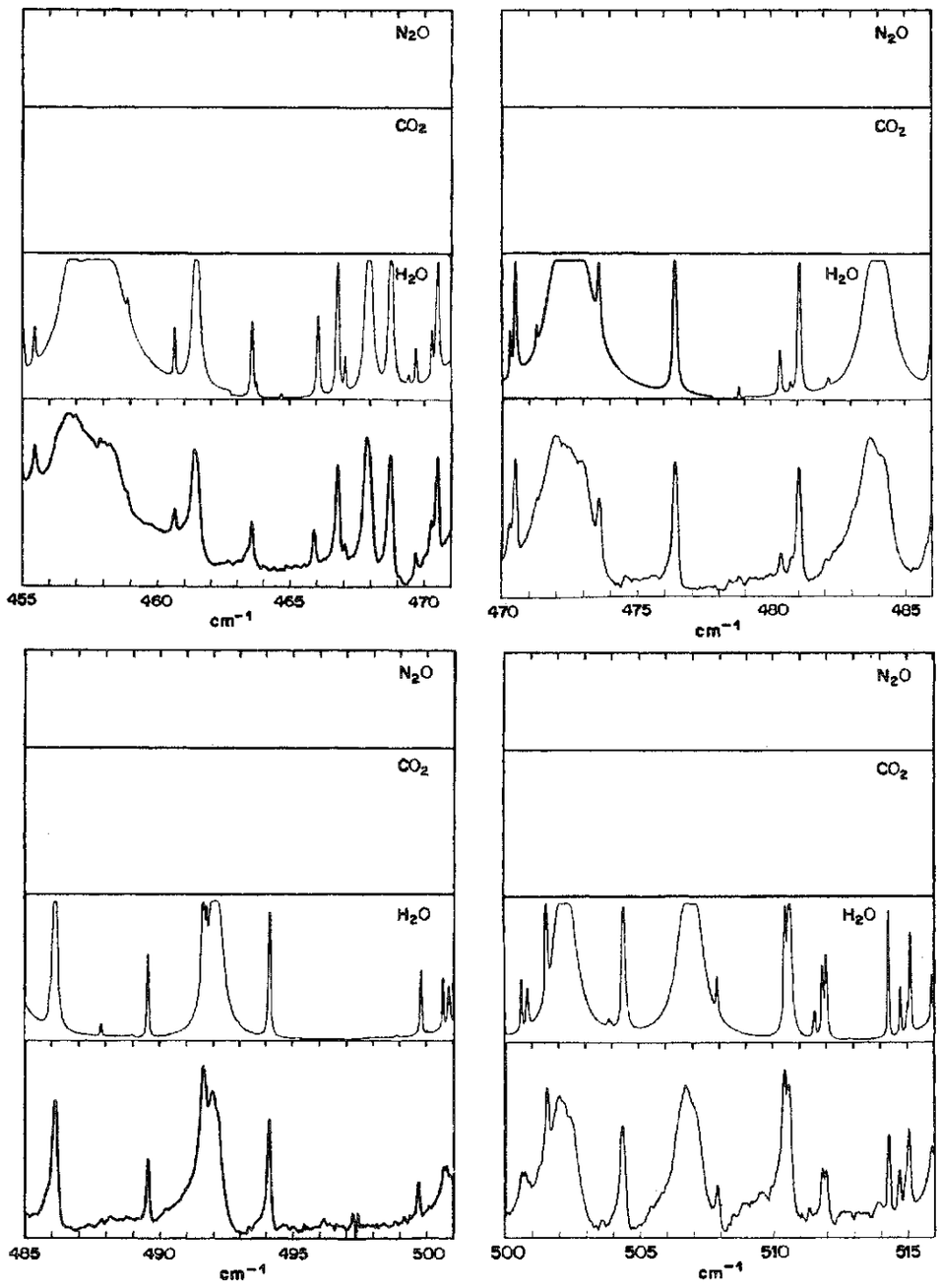


Figure 1.2: Measured and simulated atmospheric emission in spectral region near from $\sigma = 455$ cm$^{-1}$ to $\sigma = 515$ cm$^{-1}$. Upper three curves show computer simulated emission from $N_2O$, $CO_2$, and $H_2O$. Lowest curve shows emission measured by a Fourier Transform Spectrometer [1].

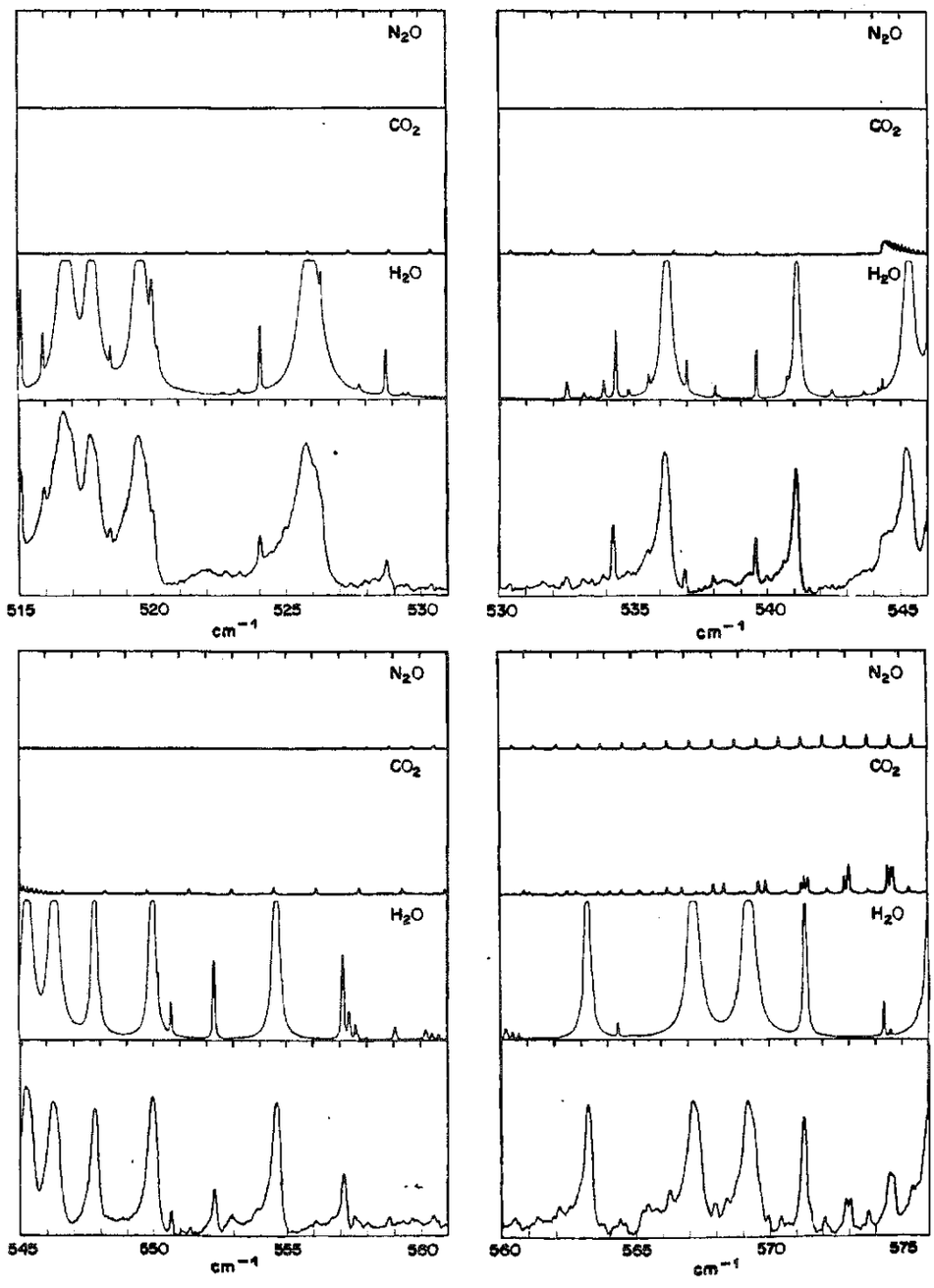


Figure 1.3: Measured and simulated atmospheric emission in spectral region near from $\sigma = 515$ cm$^{-1}$ to $\sigma = 575$ cm$^{-1}$. Upper three curves show computer simulated emission from $N_2O$, $CO_2$, and $H_2O$. Lowest curve shows emission measured by a Fourier Transform Spectrometer [1].

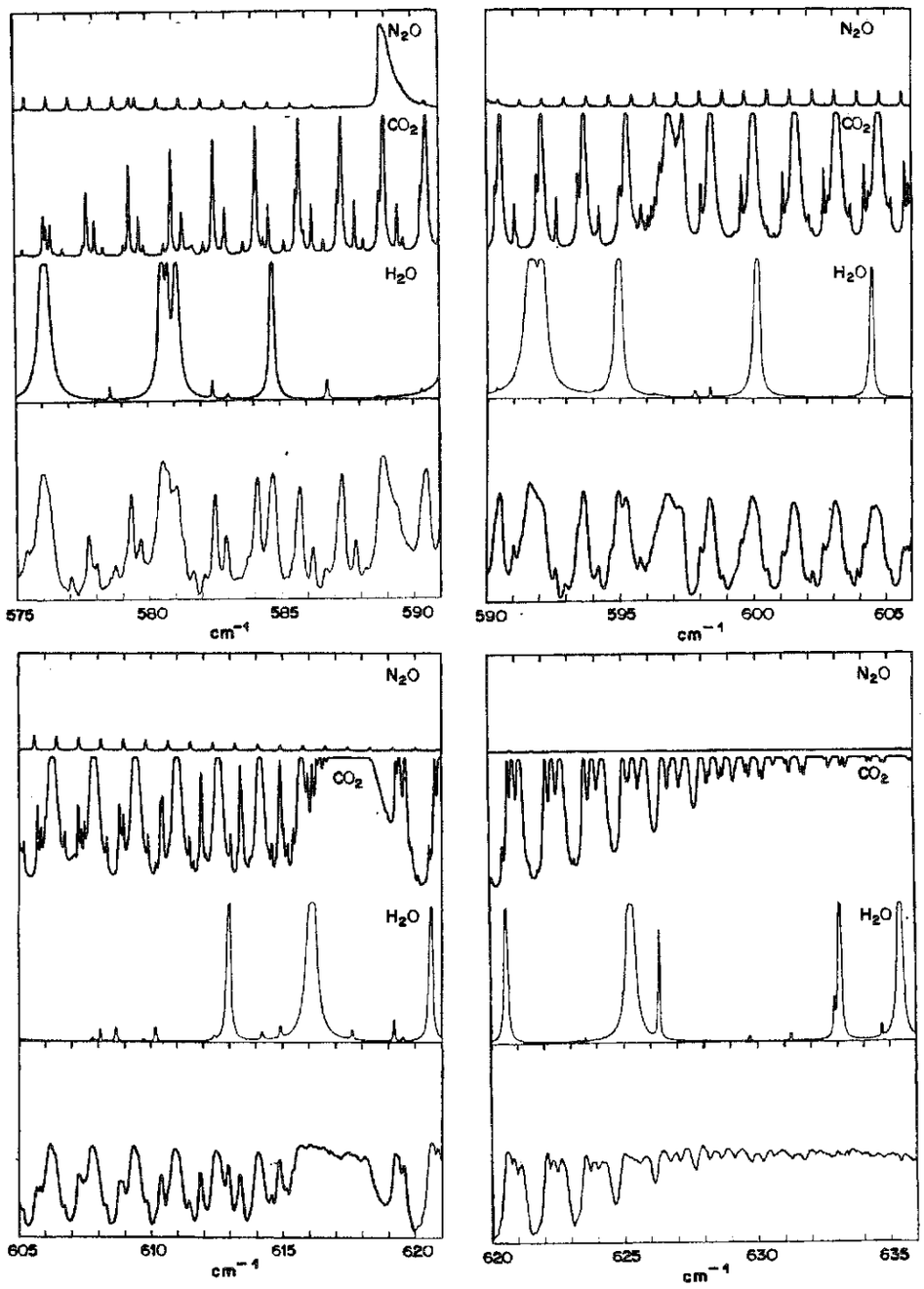


Figure 1.4: Measured and simulated atmospheric emission in spectral region near from $\sigma = 575$ cm$^{-1}$ to $\sigma = 635$ cm$^{-1}$. Upper three curves show computer simulated emission from $N_2O$, $CO_2$, and $H_2O$. Lowest curve shows emission measured by a Fourier Transform Spectrometer [1].

because the integrated line emission increases linearly with water vapour column abundance. After an emission line becomes saturated, the integrated line emission varies as the square root of water vapour abundance (see §2.5.1), reflecting the increased emission in the wings of the line. In order to be most sensitive to changes in water vapour abundance, a spectral region with many unsaturated emission lines is desirable. A detailed analysis of the data in figures 1.2, 1.3, and 1.4 [1] shows that most of these lines are unsaturated for column abundances less than 1 mm pwv, making this region well suited for sensitive radiometric measurements of water vapour.

### Radiance of Water Vapour at Infrared Wavelengths

The total flux, $\Phi$, collected by a water vapour radiometer is the product of the throughput, $A\,\Omega$, of the instrument and the radiance from the atmosphere, $L$, as expressed by

$$\Phi = A\,\Omega\,L \qquad \mathrm{W} \tag{1.7}$$

where $A$ is the area of the aperture, $\Omega$ is the solid angle of acceptance of the aperture, and $L$ is the spectral radiance of water vapour integrated over the spectral bandpass of the system. Although water vapour emission as measured by both a 183 GHz radiometer and a 20 $\mu$m radiometer will not be saturated for column abundances on the order of 1 mm pwv, saturated emission will be assumed for the purposes of this comparison between the two systems. In the case of saturation, the radiant emission from atmospheric water vapour is given by the Planck function

$$L_\sigma(T_{atm}) = B_\sigma(T_{atm}) = (2hc^2 100^4 \sigma^3)\left(e^{\frac{hc100\sigma}{kT_{atm}}} - 1\right)^{-1} \qquad \mathrm{W\ m^{-2}\ sr^{-1}\ (cm^{-1})^{-1}} \tag{1.8}$$

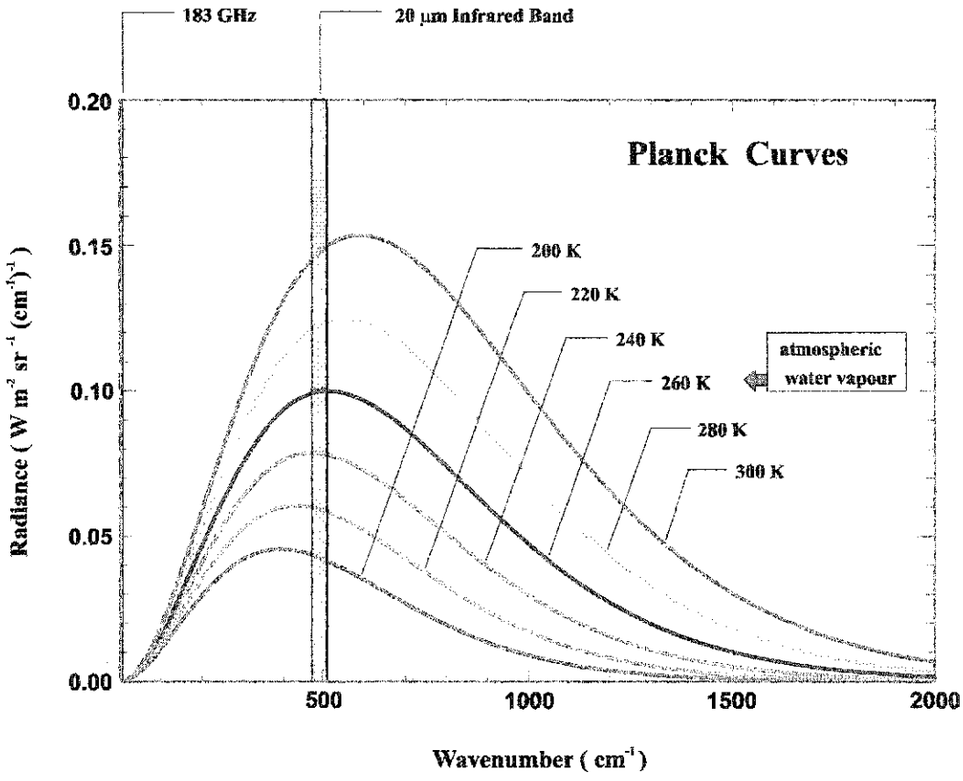


Figure 1.5: Blackbody emission curves evaluated at a range of temperatures typically found in the atmosphere.

where $T_{atm}$ is the temperature of the atmosphere in K and $\sigma$ is the wavenumber in $cm^{-1}$.

Figure 1.5 shows Planck curves for several different temperatures. At a typical atmospheric temperature of 260 K, maximum emission occurs near 20 $\mu$m (500 $cm^{-1}$) and is approximately three orders of magnitude greater than the emission at radio frequencies. For example, for a temperature of 260 K, the Planck spectral radiances at 500 $cm^{-1}$ and 183 GHz ($\sim$6.1 $cm^{-1}$) are:

$$L_{500\ cm^{-1}} = 9.98 \times 10^{-2}\ W\ m^{-2}\ sr^{-1}\ (cm^{-1})^{-1} \tag{1.9}$$

$$L_{6.1\ \mathrm{cm}^{-1}} = 7.87 \times 10^{-5}\ \mathrm{W\ m^{-2}\ sr^{-1}\ (cm^{-1})^{-1}} \tag{1.10}$$

Hence, the radiance ratio between these spectral regions is

$$\frac{L_{500\ \mathrm{cm}^{-1}}}{L_{6.1\ \mathrm{cm}^{-1}}} \simeq 1270 \tag{1.11}$$

The advantage of greater spectral radiance available to the infrared radiometer is offset by the fact that the 183 GHz water vapour radiometer uses the antenna itself as the collecting aperture. If the 15 m JCMT antenna is used as the aperture, then the collecting area is

$$A_{183\ \mathrm{GHz}} = \frac{\pi \cdot 15^2}{4} \simeq 177\ \mathrm{m^2} \tag{1.12}$$

On the other hand, IRMA was constructed with a primary optic of 125 mm diameter. In this case, the collecting area is

$$A_{\mathrm{IRMA}} = \frac{\pi \cdot (.125)^2}{4} \simeq 1.23 \times 10^{-2}\ \mathrm{m^2} \tag{1.13}$$

The collecting area of the antenna is seen to be ~14, 300 times larger than the collecting area of the IRMA instrument.

The field of view of IRMA was designed to sample a 10 m patch of atmosphere at a range of 10 km and thus corresponds to a solid angle of

$$\Omega_{\mathrm{IRMA}} = \frac{A}{r^2} = \frac{\pi d^2}{4r^2} = \frac{\pi \cdot (10)^2}{4 \cdot (10000)^2} = 7.9 \times 10^{-5}\ \mathrm{sr} \tag{1.14}$$

Assuming that the 183 GHz ($\lambda = 1.6$ mm) system operates at the diffraction limit of the JCMT antenna, the field of view of the antenna, out to the first dark ring of the Airy disk [6], subtends an angle of

$$\theta = \frac{2.44\ \lambda}{d} = \frac{2.44 \cdot (1.6 \times 10^{-3})}{15} = 2.6 \times 10^{-4}\ \mathrm{rad} \tag{1.15}$$

This corresponds to a solid angle of

$$\Omega_{183\text{ GHz}} = \frac{\pi\theta^2}{4} = \frac{\pi \cdot (2.6 \times 10^{-4})^2}{4} = 5.3 \times 10^{-8}\text{ sr} \tag{1.16}$$

When taking into account the large focal length of typical radio telescopes, the water vapour emitting region will occur in the near field and the solid angle given in equation 1.16 will no longer be valid. Calculation of the field of view of the radio antenna in this case will depend on the height of the emitting region and, while difficult to calculate, will tend to approach the solid angle given in equation 1.14.

If water vapour is assumed to emit as a blackbody then the integrated radiance is given by

$$L = \int_{\sigma_{lower}}^{\sigma_{upper}} L_\sigma \, d\sigma = \int_{\sigma_{lower}}^{\sigma_{upper}} B_\sigma \, d\sigma \text{ W m}^{-2}\text{ sr}^{-1} \tag{1.17}$$

which can be approximated as $L = B_\sigma \, \Delta\sigma = B_\sigma \, (\sigma_{upper} - \sigma_{lower})$ if the spectral radiance is considered constant over the range from $\sigma_{lower}$ to $\sigma_{upper}$.

The spectral bandwidth of IRMA, defined by the infrared filter was $\sim 500 - 550$ $\text{cm}^{-1}$, and thus $\Delta\sigma = 50\text{ cm}^{-1}$.

The 183 GHz radiometer measures water vapour emission in several discrete frequency channels placed along the line profile (figure 1.6). Each channel is on the order of 1.0 GHz wide, corresponding to $\Delta\sigma = 3.33 \times 10^{-2}\text{ cm}^{-1}$.

From the Planck spectral radiance calculated above for 183 GHz and assuming it is constant over the spectral bandwidth, a total flux for one channel can be calculated for

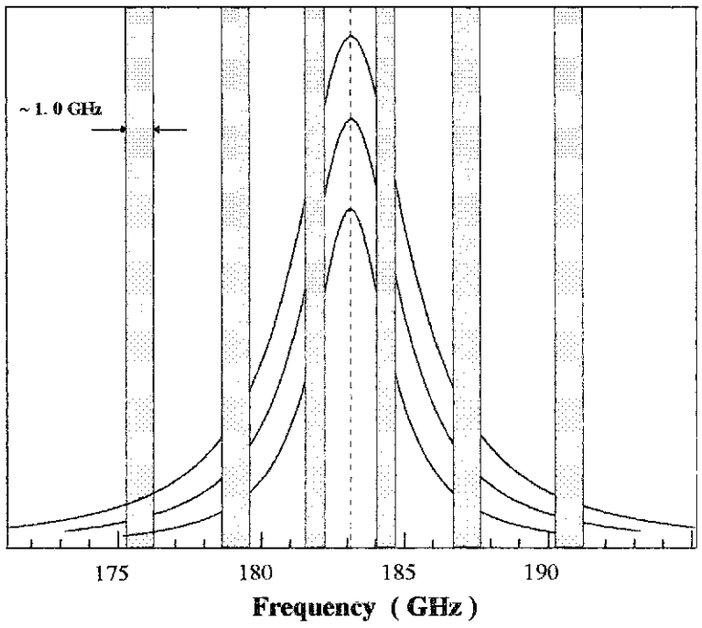


Figure 1.6: Six discrete channels are placed along the 183 GHz line profile in the radio frequency approach to measuring water vapour emission. Each channel provides a different sensitivity under different degrees of saturation.

a single measurement of water vapour abundance using the 183 GHz system

$$\begin{aligned} \Phi_{183\ \mathrm{GHz}} &= A\,\Omega\,L_{183\ \mathrm{GHz}}\,\Delta\sigma \\ &= (176)(7.9\times10^{-5})(7.87\times10^{-5})(3.33\times10^{-2}) \\ &= 3.6\times10^{-8}\ \mathrm{W} \end{aligned} \tag{1.18}$$

when, as discussed above, the solid angle of the 183 GHz system is taken to be the same as the IRMA instrument.

The flux available to the infrared radiometer is

$$\Phi_{\mathrm{IRMA}} = A\,\Omega\,L_{\mathrm{IRMA}}\,\Delta\sigma$$

$$= (0.0123)(7.9 \times 10^{-5})(9.98 \times 10^{-2})(50)$$

$$= 4.85 \times 10^{-6} \text{ W} \quad (1.19)$$

It should be remembered that the above calculations are only approximate since the radiances are overestimated in both cases (water vapour emission will not be fully saturated over either spectral range) and system efficiencies have not been taken into account. Even so, the flux available to IRMA is seen to be $\sim 2$ orders of magnitude greater than that available to the 183 GHz system using a 15 m antenna. For interferometer arrays using smaller antennae, such as ALMA, this factor increases.

### 1.3.2 Infrared Radiometer Drawbacks

There are three potential drawbacks to measuring water vapour abundance with an infrared radiometer. The first is that the small aperture of the infrared radiometer does not sample the same atmospheric column as that viewed by the antenna. To address this problem, the optics can be designed so that the radiometer samples a patch of atmosphere of the same diameter as the radio antenna at an altitude corresponding to the scale height of water vapour. Another possible solution to this problem is to install multiple infrared radiometers on a single antenna, interpolating the signals from the radiometers to derive the water vapour abundance. The second potential problem arises from the fact that the emission from ice crystals in cirrus clouds is expected to have a greater impact at infrared than at (sub)millimeter wavelengths. The discussion of cirrus emission is complicated by

the lack of detailed information on the subject. The third drawback is that water vapour emission measurements in the 20 $\mu$m spectral region become unusable at lower altitudes due to the saturation of spectral lines in this region. This is not true for the 183 GHz radiometer which can still operate at lower altitudes. However, this is not expected to be a serious problem because the latest generation of radio interferometers, such as the Smithsonian Millimeter Array (SMA) on Mauna Kea and ALMA at Chajnantor, are located at high altitude sites where the infrared radiometer is expected to be effective.

### 1.3.3 Temporal Resolution

An estimate of the integration time required to compensate effectively for rapid variations in atmospheric water vapour content above an antenna can be made by considering the windspeed and antenna size, as depicted in figure 1.7. Windspeeds of 100 km $hr^{-1}$ are typical for high altitude sites. At this speed, the time for a water vapour feature to cross a 10 m diameter antenna is $\sim$ 0.36 s. Actual water vapour features are much more complicated than the one depicted in the figure, so a temporal resolution of 0.1 s was specified for IRMA.

## 1.4 Phase Correction Requirements for ALMA

Current plans for ALMA call for an array of 64 antennae, each of 12 m diameter arranged over a baseline of a 10 km ring. Due to its long baseline, ALMA promises sub-milli-arcsecond imaging under the best atmospheric conditions. At Chajnantor, the high

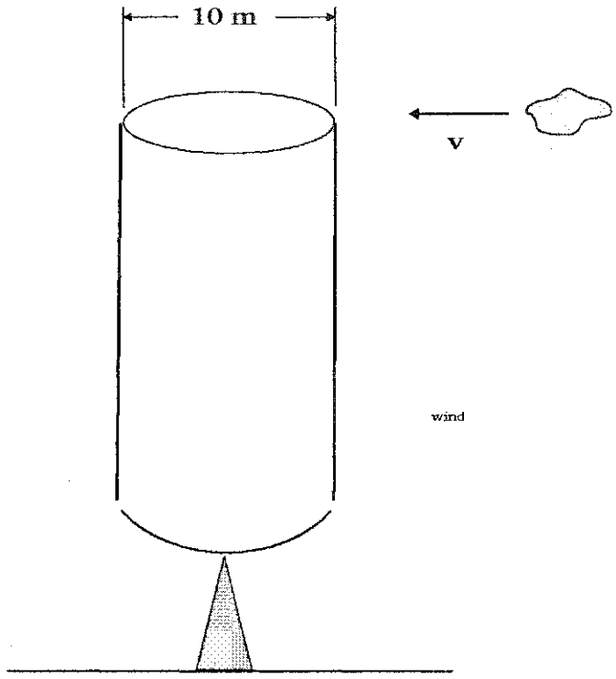


Figure 1.7: A simple model used to calculate the temporal resolution based on windspeed and antenna beam crossing time.

altitude site for ALMA, typical measurements of water vapour column abundance, $w$, show a range between 0.5 and 4 mm pwv with an average of 1 mm pwv. The ALMA site is shown in the photograph in figure 1.8 and an artist's conception of the finished ALMA interferometer is shown in figure 1.9.

The phase difference between signals from two antennae is expressed in terms of a visibility, $V$ [3]

$$V = V_0 e^{i\phi} \tag{1.20}$$

where $\phi$ is the phase difference between the signals at a given operating frequency and $V_0$ is

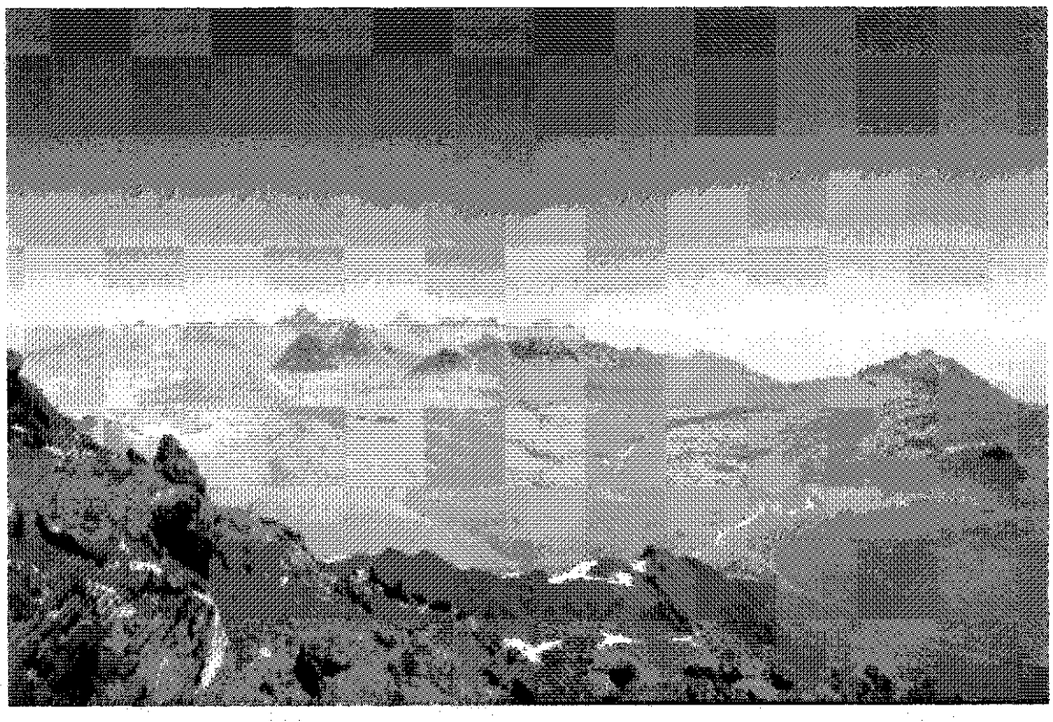

Figure 1.8: A view of the Atacama plateau, future site of the Atacama Large Millimeter Array (ALMA).

the maximum visibility occurring at zero phase delay. The effect on the average amplitude of $V$ due to phase noise is [3]

$$\langle V \rangle = V_0 \left\langle e^{i\phi} \right\rangle = V_0 e^{\frac{-\phi_{rms}^2}{2}} \tag{1.21}$$

where $\phi_{rms}$ is the rms phase fluctuation due to variation in water vapour abundance. This equation can be expressed in terms of the array baseline, $b$, using theoretical models of turbulence, for example, that due to Kolmogorov [3]. Thus, a phase error of 1 radian gives a coherence of

$$\frac{\langle V \rangle}{V_0} = 0.6 \tag{1.22}$$

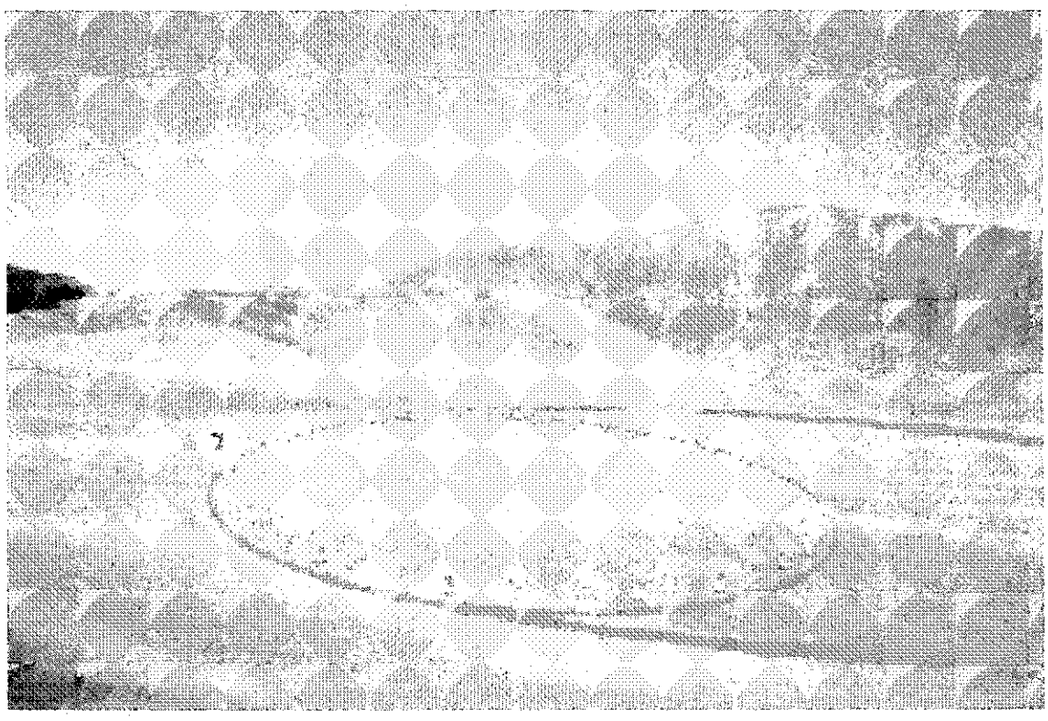

Figure 1.9: Artist's conception of the ALMA array.

According to a recent ALMA memo [7], the target electromagnetic path resolution is 50 $\mu$m. Using equation 1.5, this translates into a column abundance resolution of 7.7 $\mu$m pwv, leading to a coherence of $\sim$ 95 % at 300 GHz and 85 % at 600 GHz. Another memo [8] suggests a target path resolution at 11.5 $\mu$m (1.8 $\mu$m pwv), but concedes that this is '*setting the bar very high*'.

The goal for IRMA II was to measure water vapour column abundances to a resolution of $\pm 1$ $\mu$m pwv (6.5 $\mu$m path length resolution) in an integration time of 1 s. This thesis will discuss the results obtained with IRMA II operating at the JCMT from December 2000 to March 2001.

## 1.5 Radiative Transfer Modelling

As was seen in § 1.3, atmospheric spectra can be modeled to a high degree of accuracy. The radiative transfer model used to produce the spectrum in figures 1.2, 1.3, and 1.4 was the Fast Atmospheric Signature Code (FASCODE) [9], a massive (71,000 lines) Fortran program. While this program is excellent for modelling atmospheric emission for general locations and observing geometries, it is difficult to modify it to model a specific location, such as Mauna Kea. The desire for a flexible atmospheric radiative transfer model provided the impetus for the development of a new model, written in the fourth generation computer language, Interactive Data Language (IDL®) [10] (IDL® is an ideal language for this purpose because of its many array handling routines and graphical interfaces). This model, known as the University of Lethbridge Transmission Radiance Atmospheric Model (ULTRAM), is described in Chapter 3 of this thesis. The model readily accommodates user-definable atmospheres.

## 1.6 Summary

Chapter 2 of the thesis contains a review of the radiative transfer theory behind the operation of IRMA. Chapter 3 describes the underlying principles involved with basic atmospheric modelling and discusses the development of ULTRAM, a new radiative transfer model developed to compute atmospheric emission and/or transmission spectra from above Mauna Kea. Chapter 4 reviews the development of the infrared radiometer and discusses the upgrades made after the initial tests of IRMA in December 1999. Chapter 5 details

the analysis of data obtained with IRMA II from December, 2000 to March, 2001, using the radiative transfer model, ULTRAM. Over 1000 data files were used in the analysis and were compared to various other measures of water vapour abundance above Mauna Kea. This chapter concludes with a theoretical explanation of some of the results obtained from the comparisons. Chapter 6 concludes the thesis with a review of the results obtained with IRMA II and the future direction of the IRMA project, including the development of IRMA III which is slated for deployment to Mauna Kea and Chajnantor in 2003.

# Chapter 2

# Radiative Transfer Theory

## 2.1 Overview

This chapter deals with radiative transfer through the atmosphere of the earth. Section 2.2: Radiative Transfer Definitions introduces the basic quantities calculated or derived in radiative transfer. Section 2.3: Radiative Transfer Through a Single Layer describes the equations of absorption and emission through a single layer atmosphere. Section 2.4: Absorption Coefficient explains the calculation of the absorption coefficient, including discussions of spectral line broadening mechanisms and calculation of integrated line strength. Section 2.5: Curve-of-Growth discusses the synthesis of a curve-of-growth of a spectral line.

## 2.2 Radiative Transfer Definitions

The propagation of electromagnetic radiation through a medium, such as the atmosphere, is described by the equations of radiative transfer. Molecules in the atmosphere

scatter, absorb, and emit electromagnetic radiation. Radiation can be scattered by particulates. Scattering is a continuous phenomenon that is strongly dependent on the particle size and radiation wavelength. Since the effects of scattering decrease with increasing wavelength they have not been considered in the theoretical model developed in this thesis.

Processes such as absorption and emission of radiation are the result of a change in the quantum state of an atom or molecule. When photons of a specific energy (which is directly proportional to their frequency) encounter an atom or molecule in a low energy quantum state, they can be absorbed by the atom or molecule, thereby raising the quantum state to a higher energy level. To be absorbed, a photon must possess the same energy as the difference in energy of an allowed transition between quantum states. Emission is the inverse process of absorption; an atom or molecule in a high energy quantum state will drop to a lower energy quantum state, thereby emitting a photon with the same energy as the difference in energy between the two states. A photon emitted due to a quantum state change has a discrete frequency which is associated with the energy difference between the two quantum states. Each atomic or molecular species has its own unique spectral signature which can be used in remote sensing applications.

Infrared absorption and emission lines in the atmosphere are mainly due to transitions in the energy states of *molecules*. Molecular energy states are associated with three different modes. The greatest amount of energy is associated with the electronic configuration of the molecules. Energy is absorbed and emitted when electrons make transitions between quantized energy levels. Energy is also associated with the vibrational state of a molecule. In this case, energy transitions cause a quantized change in the frequency of

vibrations of atoms in the molecules. Less energy is associated with the vibrational state than the electronic configuration of the molecule. While electronic transitions give rise to spectral lines at visible wavelengths, vibrational transitions are associated with spectral lines at near-infrared wavelengths. Finally, energy is associated with the rotational state of a molecule. An increase in the rotational energy of a molecule results in a quantized increase in the frequency of rotation. The rotational states of a molecule have the smallest energy scale structure. Rotational transitions are responsible for the spectral lines in the far-infrared part of the spectrum. In general, energy can be distributed in all three modes. This thesis involves the mid-infrared, and thus the pure rotational spectrum of water vapour.

The formulae of radiative transfer are often expressed in terms of frequency, $\nu$ (Hz), or wavelength, $\lambda$ ($\mu$m). In this thesis, formulae will be given in terms of *wavenumber*, $\sigma$, which is the reciprocal of wavelength, $1/\lambda$, and has units of $\mathrm{cm}^{-1}$. Using the wave equation for the speed of light in a vacuum, $c = \nu\lambda$, the wavenumber is related to frequency by

$$\sigma = \frac{\nu}{c} \quad \mathrm{cm}^{-1} \tag{2.1}$$

where $\nu$ is the frequency in Hz and $c = 2.998 \times 10^{10}$ cm·s$^{-1}$ is the speed of light in a vacuum.

The analysis of radiative transfer is formulated in terms of spectral energy, $E_\sigma$, spectral power, $\Phi_\sigma$, spectral radiant intensity, $I_\sigma$, and spectral radiance, $L_\sigma$. The subscript, $\sigma$, denotes that the quantity is a differential with respect to wavenumber such as $E_\sigma = \frac{dE}{d\sigma}$. Thus, the total energy, power, intensity, and radiance are obtained by integrating over a

| Radiometric Quantity | Symbol | Units |
|---|---|---|
| Spectral energy | $E_\sigma$ | J $(\text{cm}^{-1})^{-1}$ |
| Spectral power | $\Phi_\sigma$ | W $(\text{cm}^{-1})^{-1}$ |
| Spectral intensity | $I_\sigma$ | W $\text{sr}^{-1}$ $(\text{cm}^{-1})^{-1}$ |
| Spectral radiance | $L_\sigma$ | W $\text{m}^{-2}$ $\text{sr}^{-1}$ $(\text{cm}^{-1})^{-1}$ |

Table 2.1: Radiometric quantities and associated units.

spectral range of interest. These quantities are defined in table 2.1.

As shown in figure 2.1, the spectral intensity, $I_\sigma$, describes the emission of radiant power, $\Phi_\sigma$, emanating from a source area $dA$, or an equivalent projected area $dA_P = dA\cos\theta$, contained within a solid angle $d\Omega$, labelled as travelling in a direction centered on solid angle $d\Omega$, and normalized to a unit solid angle

$$I_\sigma = \frac{d\Phi_\sigma}{d\Omega} \qquad \text{W sr}^{-1}\ (\text{cm}^{-1})^{-1} \tag{2.2}$$

This emission is equivalent to that from a point source $P$ at a distance $r$ from the surface $dA$. Spectral radiance, $L_\sigma$, normalizes the emitted spectral energy to unit *projected* area element $dA_P$ in addition to unit solid angle

$$L_\sigma = \frac{dI_\sigma}{dA_P} = \frac{d^2\Phi_\sigma}{dA_P\, d\Omega} \qquad \text{W m}^{-2}\ \text{sr}^{-1}\ (\text{cm}^{-1})^{-1} \tag{2.3}$$

Using these basic quantities, a general formula expressing the transfer of radiant energy from one physical surface to another, as in figure 2.2, is given by

$$d^2\Phi_{\sigma 1,2} = L_{\sigma 1}\frac{dA_1\cos\theta_1 dA_2\cos\theta_2}{r^2} \tag{2.4}$$

where $\Phi_{\sigma 1,2}$ is the spectral power transferred from surface $A_1$ to surface $A_2$ and $L_{\sigma 1}$ is the spectral radiance of surface $A_1$. Area elements $A_1$ and $A_2$ are arbitrarily shaped and

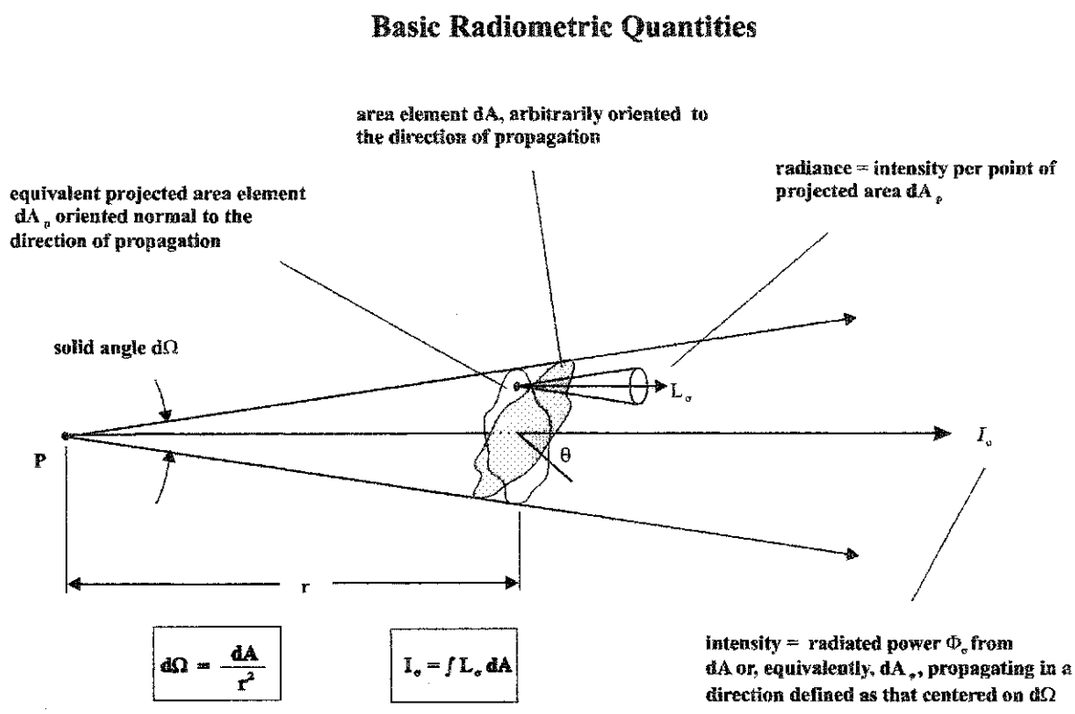


Figure 2.1: Illustration of basic radiometric quantities.

oriented surfaces whose normal vectors subtend the angles $\theta_1$ and $\theta_2$ with respect to the distance between differential elements $dA_1$ and $dA_2$. In this thesis, the surfaces are assumed to be planar and parallel to each other (i.e. $\theta_1 = \theta_2 = 0$) thus simplifying the analysis.

The quantities of spectral intensity and spectral radiance are important in the following sections that deal with radiative transfer through the atmosphere.

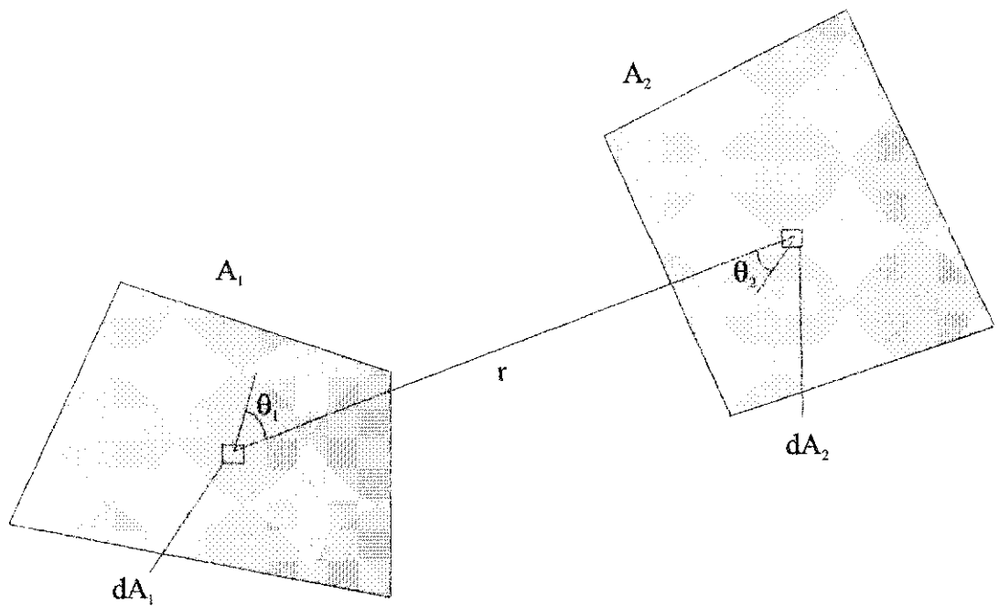


Figure 2.2: Radiative transfer between two arbitrary surfaces.

## 2.3 Radiative Transfer Through a Single Layer

### 2.3.1 Absorption by a Single Layer

The net loss of spectral intensity of electromagnetic radiation through absorption in a layer, shown in figure 2.3, is given by the equation [11]

$$dI_a = -Ik_\sigma n dz = -Ik_\sigma du \tag{2.5}$$

where $k_\sigma$ is the absorption coefficient in $cm^2$-$molecule^{-1}$, $n$ is the number density of the absorber in molecules-$cm^{-3}$, $dz$ is the thickness of the layer in cm, and $du = ndz$ is the *absorber column density* or *absorber column amount* in units of molecules-$cm^{-2}$. The term

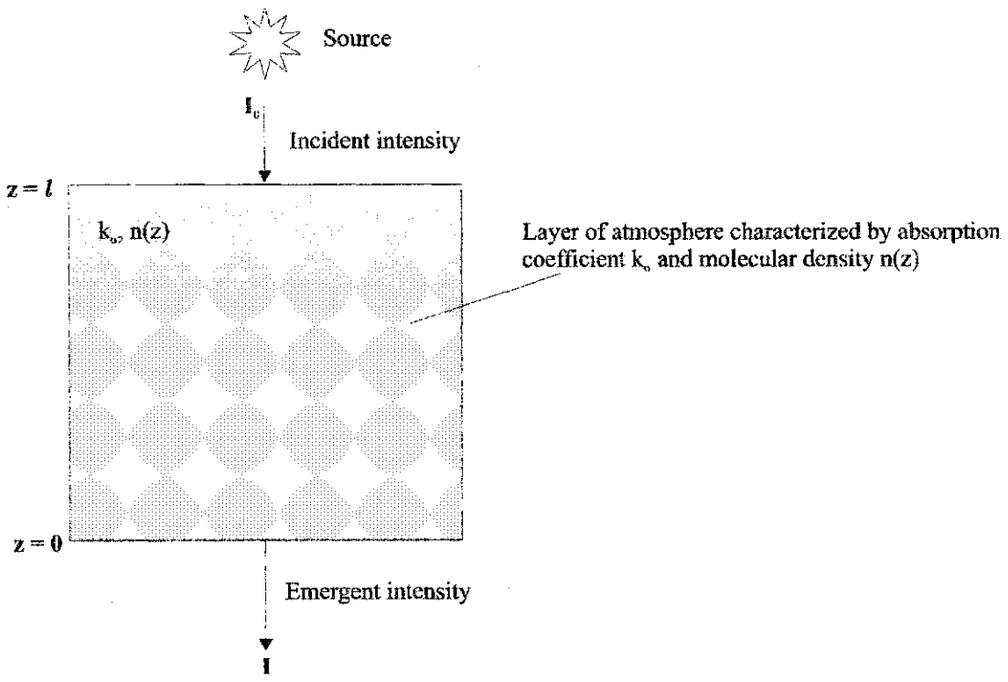


Figure 2.3: Absorption of radiation by an atmospheric layer.

$k_\sigma n$ gives absorption per cm in the propagation direction. This means that the absorption is specified for a column of the atmosphere extending in the direction of propagation.

The transmission of radiation through the layer can be readily obtained by integration of equation 2.5. For transmission of incident radiation of spectral intensity $I_0$ through a layer of thickness $l$, absorber density $n$, and absorption coefficient $k_\sigma$, the spectral intensity transmitted can be written as

$$I = I_0 e^{-\int_0^l k_\sigma n dz} \qquad \text{W sr}^{-1}\ (\text{cm}^{-1})^{-1} \tag{2.6}$$

In the case of a layer of constant absorber density $n$, the spectral intensity of the

transmitted radiation is

$$I = I_0 e^{-k_\sigma nl} = I_0 e^{-k_\sigma u} \qquad \text{W sr}^{-1}\ (\text{cm}^{-1})^{-1} \tag{2.7}$$

where $u = nl$ is the *absorber column abundance* in molecules·cm$^{-2}$.

In the real atmosphere the molecular density decays exponentially with height, so the absorption must be calculated for a layer in which the molecular density, $n(z)$, varies with height, $z$. In this case, the integral cannot be simplified and the transmitted intensity is written as

$$I = I_0 e^{-\int_0^l k_\sigma n(z)dz} \qquad \text{W sr}^{-1}\ (\text{cm}^{-1})^{-1} \tag{2.8}$$

The quantity $e^{-\int_0^l k_\sigma n(z)dz}$ in equations 2.6 and 2.8 is known as the *fractional transmission*, T, i.e. the fraction of the incident radiation that is transmitted through the layer. A measure of the *opacity* of the layer, known as the *optical path* [11] is given by

$$\tau = \int_0^l k_\sigma n(z)dz \tag{2.9}$$

which is equivalent to

$$\tau = k_\sigma n_{av} l \tag{2.10}$$

If the opacity is measured from the top of the atmosphere downwards, it is known as the *optical depth.*

### 2.3.2 Emission by a Single Layer

The process of emission in the atmosphere is, in essence, the inverse process of absorption. Instead of photons of an appropriate energy being used to increase the energy

state of molecules, emission of radiation results when molecules undergo a transition from an excited to a lower energy state.

The spectral intensity of electromagnetic radiation emitted per unit area by a layer can be written as [11]

$$dI_e = k_\sigma J(\sigma, T) n(z) dz \qquad \text{W sr}^{-1} \text{ (cm}^{-1})^{-1} \tag{2.11}$$

where $J(\sigma, T)$ is the *radiation source function* in units of W m$^{-2}$ sr$^{-1}$ (cm$^{-1}$)$^{-1}$ and the other terms have been defined previously in § 2.3.1. The term $dI_e$ represents a net gain to the radiation field.

Since collisions between molecules occur frequently in the troposphere, redistributing energy between the various modes, it is reasonable to assume that the individual layers of the atmosphere are in *Local Thermodynamic Equilibrium (LTE)* at characteristic layer temperatures. This assumption of LTE means that the radiation entering a layer is balanced by the radiation exiting the layer. Under LTE, the source function $J(\sigma, T)$ is equal to the *Planck function* for blackbody emission at temperature $T$ [11]

$$J(\sigma, T) = B(\sigma, T) = 100^4 \left( \frac{2hc^2\sigma^3}{e^{\frac{hc100\sigma}{k_B T}} - 1} \right) \qquad \text{W m}^{-2} \text{ sr}^{-1} \text{ (cm}^{-1})^{-1} \tag{2.12}$$

where $h = 6.626 \times 10^{-34}$J·s is the Planck constant, $k_B = 1.381 \times 10^{-23}$ J·K$^{-1}$ is the Boltzmann constant, and $c$ is the speed of light in cm·s$^{-1}$.

### 2.3.3 Radiative Transfer Through a Single-Layer

Until this point, the processes of absorption and emission in the atmosphere have been treated separately. In reality, the processes of emission and absorption occur simul-

taneously within a layer, as shown in figure 2.4. The *total* change in spectral intensity is found by combining equation 2.5 with equation 2.11 to give

$$dI = dI_e - dI_a = k_\sigma B(\sigma, T)n(z)dz - k_\sigma I_\sigma n(z)dz \tag{2.13}$$

This equation can be simplified further by dividing by the *optical depth* of the layer

$$d\tau = k_\sigma n(z)dz \tag{2.14}$$

to give

$$\frac{dI}{d\tau} = B - I \tag{2.15}$$

which is known as the *Schwarzchild equation* [11], the differential form of the equation of radiative transfer. Note that the subscripts have been dropped for clarity. This equation can be integrated by use of an integrating factor $e^\tau$

$$e^\tau \frac{dI}{d\tau} = e^\tau B - e^\tau I \tag{2.16}$$

which can be rewritten as

$$e^\tau \frac{dI}{d\tau} + e^\tau I = e^\tau B \tag{2.17}$$

which is equivalent to

$$\frac{d(e^\tau I)}{d\tau} = e^\tau B \tag{2.18}$$

since $\frac{d(e^\tau)}{d\tau} = e^\tau$.

Equation 2.18 is integrated from $\tau = 0$ at the top of the layer to an arbitrary $\tau$ which gives

$$\int_0^\tau \frac{d}{d\tau}(e^\tau I)d\tau = \int_0^\tau e^\tau B d\tau \tag{2.19}$$

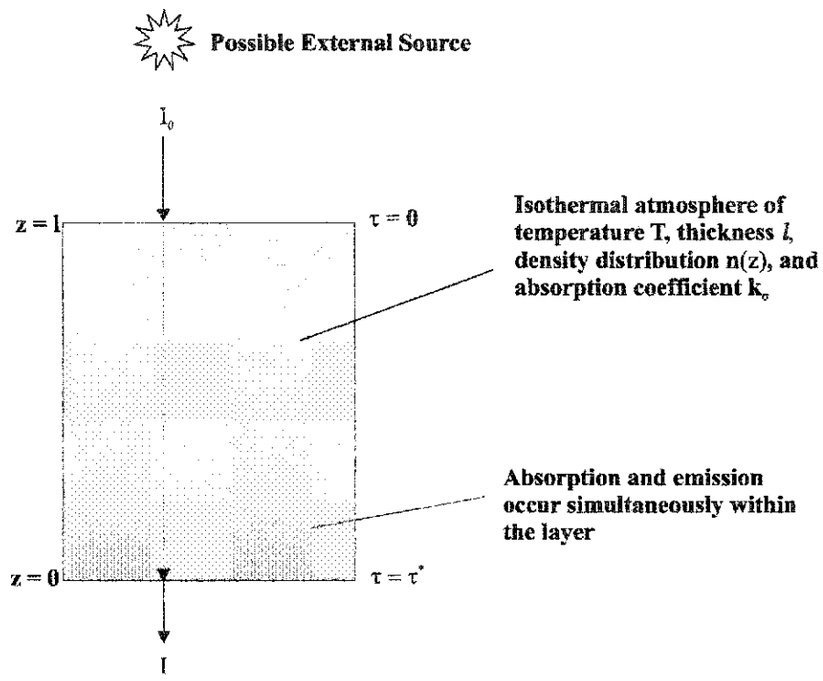


Figure 2.4: The absorption and emission of radiation in an atmospheric layer.

which becomes

$$(e^{\tau} I)|_0^{\tau} = (e^{\tau} B)|_0^{\tau} \tag{2.20}$$

which expands to

$$e^{\tau} I - I_0 = B(e^{\tau} - 1) \tag{2.21}$$

where $I_0$ is the intensity at the top of the layer. Equation 2.21 is then divided by $e^{\tau}$ to give the intensity of the radiation exiting the bottom of the layer as

$$I = I_0 e^{-\tau} + B(1 - e^{-\tau}) \qquad \text{W sr}^{-1} \text{ (cm}^{-1})^{-1} \tag{2.22}$$

Finally, equation 2.22 can be combined with equation 2.14 to give the intensity at

the bottom of the layer as

$$I = I_0 \left( e^{-\int_0^l k_\sigma n(z) dz} \right) + B \left( 1 - e^{-\int_0^l k_\sigma n(z) dz} \right) \qquad \text{W sr}^{-1} \ (\text{cm}^{-1})^{-1} \tag{2.23}$$

The first term in equation 2.23 represents the spectral intensity of radiation transmitted through the layer. The second term represents the spectral intensity of the radiation emitted by the layer. The contribution of these terms to the spectral intensity at the bottom of the layer therefore depends on the opacity, $\tau$. There exist two limiting cases: when the opacity is low, most of the incident radiation is transmitted through the layer, but little radiation is emitted by the layer. In the case where opacity is high, most of the incident radiation is absorbed by the layer, which then emits as a blackbody of the characteristic layer temperature.

### 2.3.4 Radiance of a Single Spectral Line

Radiometer measurements are commonly given in terms of radiance. The conversion to radiance is easily accomplished by dividing the intensity by the projected area of the source and thus equation 2.22 becomes

$$L_\sigma = L_{\sigma 0} e^{-\tau} + B_\sigma (1 - e^{-\tau}) \qquad \text{W m}^{-2} \ \text{sr}^{-1} \ (\text{cm}^{-1})^{-1} \tag{2.24}$$

If it is assumed that the radiometer is not observing a celestial object, the spectral radiance incident at the top of the atmosphere, $L_{\sigma 0}$, is due to the 3 K cosmic microwave background radiation [12]. From equation 2.12, it can be shown that this contribution

is negligible at the infrared wavelengths observed by the radiometer. Thus equation 2.24 becomes

$$L_\sigma = B_\sigma(1 - e^{-\int_0^l k_\sigma n(z)dz}) \qquad \text{W m}^{-2}\ \text{sr}^{-1}\ (\text{cm}^{-1})^{-1} \tag{2.25}$$

using equation 2.9. Finally, using equation 2.10, the spectral radiance observed by the radiometer is

$$L_\sigma = B_\sigma(1 - e^{-k_\sigma n_{av} l}) \qquad \text{W m}^{-2}\ \text{sr}^{-1}\ (\text{cm}^{-1})^{-1} \tag{2.26}$$

A molecular species present in fully saturated conditions (i.e. $k_\sigma n_{av} l \gg 1$) is seen to emit at a maximum radiance given by the Planck function evaluated at the atmospheric temperature at which the species resides.

## 2.4 Absorption Coefficient

### 2.4.1 Absorption Coefficient Components

In the case of radiative transfer of a single spectral line, the absorption coefficient, $k_\sigma$ has the form [11]

$$k_\sigma = S\ f(\sigma - \sigma_0) \qquad \text{cm}^2\ \text{molecule}^{-1} \tag{2.27}$$

where $S$ is the *integrated line strength* described in § 2.4.3 and $f(\sigma - \sigma_0)$ is a normalized line shape function such that

$$\int_0^\infty f(\sigma - \sigma_0)d\sigma = 1 \tag{2.28}$$

The exact form of the line shape function, $f(\sigma - \sigma_0)$, depends on the line broadening mechanism. Each line shape is associated with a characteristic *half-width at half maximum*

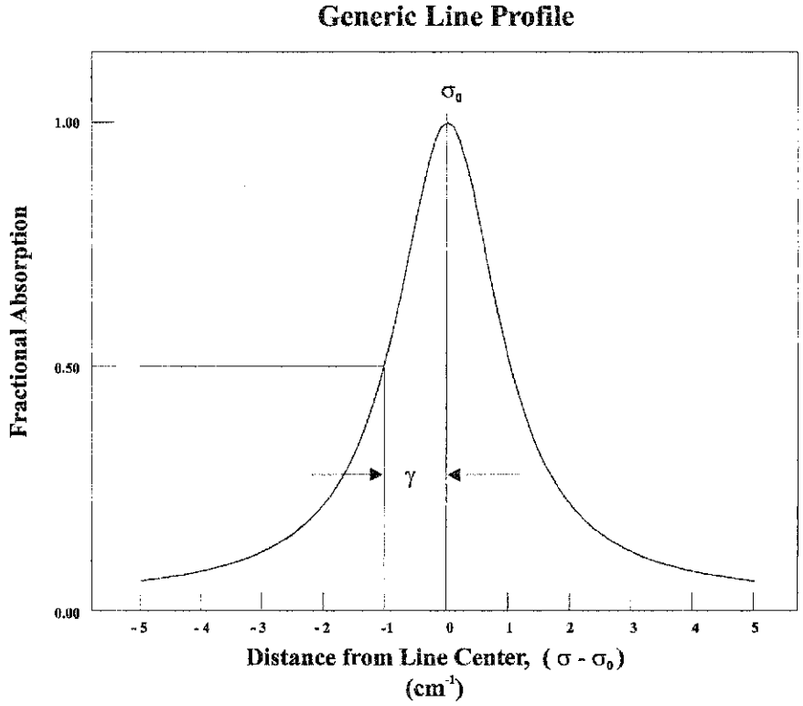


Figure 2.5: A generic spectral line shape, characterized by the Half-Width at Half Maximum (HWHM), $\gamma$, the distance from the line center at which the absorption is half of the maximum absorption.

(or HWHM), $\gamma$, which is shown in figure 2.5. This half-width is the distance, in units of wavenumbers, from the line center, $\sigma_0$, to the points on either side of the line center where the absorption falls to one half of its maximum value (i.e. $f(\gamma) = \frac{f(\sigma_0)}{2}$). The line shape function is a result of the broadening mechanism determined by the local conditions of temperature and pressure. If there is a change in the broadening regime, the line shape changes in response.

In the case where more than one spectral line is involved, it is necessary to adjust

$k_\sigma$ to account for the presence of other lines. If $n$ lines are being considered then

$$k_\sigma = \sum_{i=1}^{n} k_i(\sigma) \qquad \text{cm}^2 \text{ molecule}^{-1} \tag{2.29}$$

where

$$k_i(\sigma) = S_i \; f_i(\sigma - \sigma_{0,i}) \qquad \text{cm}^2 \text{ molecule}^{-1} \tag{2.30}$$

### 2.4.2 Broadening Mechanisms

There are three principal broadening mechanisms that cause a spectral line to have a finite width.

The *natural line width* arises from the variability in quantum energy levels due to the Heisenberg uncertainty principle. According to the Heisenberg uncertainty principle, there is an uncertainty in the energy level of a quantum state that is related to the lifetime of the quantum state through the equation, $\Delta E \simeq \frac{\hbar}{\Delta t}$ [13], where $\Delta E$ is the uncertainty in energy and $\Delta t$ is the lifetime of the quantum state. This results in an uncertainty in the line center of

$$\Delta\sigma = \frac{\Delta E}{\hbar c} \qquad \text{cm}^{-1} \tag{2.31}$$

where $\hbar = \frac{h}{2\pi}$, $h$ is Planck's constant, and $c$ is the speed of light. A typical lifetime for an excited molecular rotational energy state in the mid-infrared region is about $10^{-2}$ s [14]. The uncertainty in energy is then

$$\Delta E \simeq \frac{1.055 \times 10^{-34} \; J \cdot s}{10^{-2} \; s} = 1.055 \times 10^{-32} \; J$$

And hence, the natural line width is

$$\Delta\sigma = \frac{1.055 \times 10^{-32}\ J}{1.055 \times 10^{-34}\ J \cdot s \times 2.998 \times 10^{10}\ cm\ s^{-1}} \simeq 3.336 \times 10^{-9}\ \text{cm}^{-1}$$

Since the natural width is insignificant when compared to the widths given by the other broadening mechanisms, it can be neglected in atmospheric modelling.

The second broadening mechanism arises from the Doppler shift in frequency due to motions of molecules towards or away from the observer. These relative velocities give rise to small frequency shifts in the emitted radiation. Since the velocity components along the line of sight have a Maxwellian distribution, the Doppler line shape is Gaussian and can be expressed as [15]

$$f(\sigma - \sigma_0) = \sqrt{\frac{\ln 2}{\pi}} \frac{1}{\gamma_D} \exp - \left[ \ln 2 \left( \frac{\sigma - \sigma_0}{\gamma_D} \right)^2 \right] \quad \text{cm} \tag{2.32}$$

where $\gamma_D$ is the Doppler half-width given by [15]

$$\gamma_D = \frac{\sigma_0}{c} \left( \frac{2 \ln 2\ k_B T}{(M/N_A)} \right)^{1/2} \quad \text{cm}^{-1} \tag{2.33}$$

where $M$ is the molar mass of the molecule in kg and $N_A = 6.022 \times 10^{23}$ mol$^{-1}$ is Avogadro's number.

As can be seen in equation 2.33, the Doppler broadening mechanism becomes important as the temperature of the gas in a layer increases. Equation 2.33 also shows that Doppler broadening becomes more important for spectral lines at high frequencies and for molecular species with low molar masses.

The third broadening mechanism arises from collisions between molecules and is dominant in the lower atmosphere. At higher pressures, molecules collide with one another more frequently and thus interrupt the quantum state transitions, producing a uniquely broadened line shape, known as the *Lorentz profile* . The Lorentz profile can be written as [11]

$$f(\sigma - \sigma_0) = \frac{S\gamma_L}{\pi} \frac{1}{(\sigma - \sigma_0)^2 + \gamma_L^2} \quad \text{cm} \tag{2.34}$$

where $\gamma_L$ is the Lorentz half-width given by [11]

$$\gamma_L = \frac{1}{4\pi\tau c} = \gamma_0 \frac{P}{P_0} \sqrt{\frac{T_0}{T}} \quad \text{cm}^{-1} \tag{2.35}$$

where $\tau$ is the mean time between collisions, $P$ is the pressure, $T$ is the temperature, and $\gamma_0$ is a reference half-width tabulated in the literature from spectroscopic measurements made under standard conditions $P_0 = 1.013 \times 10^5$ Pa and $T_0 = 296$ K.

Figure 2.6 shows a comparison of the Doppler and Lorentz line shapes of identical half-width and were normalized to unit area so that each line represents the same total absorption. The Lorentz line shape has much broader line wings while the Doppler line shape features a more strongly absorbing line center.

In the atmosphere of the earth, there are two spectral line broadening regimes. In the upper atmosphere, where pressures are low and molecular collisions are less frequent, the Doppler line shape is dominant. In the lower atmosphere, where pressure is greater and molecular collisions occur more frequently, the Lorentz profile dominates. Between these two extremes, both line shapes contribute to the overall line profile. The amount that each profile contributes to the overall shape depends on the temperature and pressure of

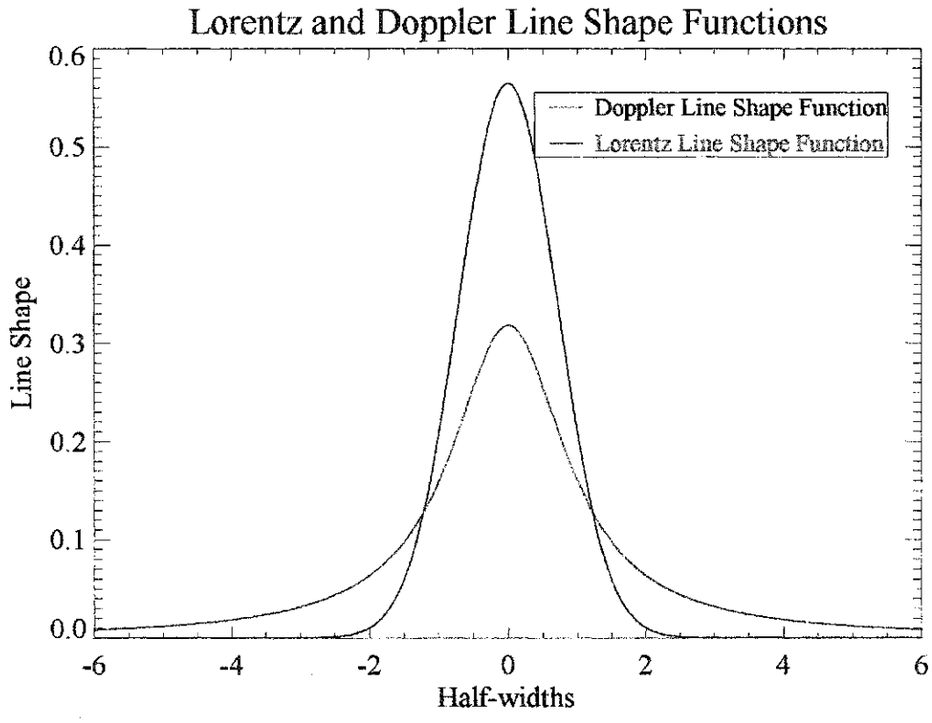


Figure 2.6: A comparison of the Doppler (black) and Lorentz (red) line shape functions having the same half-width.

the atmosphere at the altitude considered. To account for the contributions of the Lorentz and Doppler profiles, a new profile, known as the *Voigt*, can be defined. The Voigt profile, which is discussed in further detail in §3.4.1, represents a convolution of the two other line profiles and can be written as

$$f_V = f_D * f_L \tag{2.36}$$

### 2.4.3 Spectral Line Strength

The line strength, $S$ in equation 2.27 is given by [11]

$$S = \int_0^\infty k_o \, d\sigma \tag{2.37}$$

in units of $\text{cm}^{-1}$ $(\text{molecules}\cdot\text{cm}^{-2})^{-1}$. For a given temperature, the line strength is a fundamental property of the absorbing molecule, dependent on the probability of the quantum transition which, in general, cannot be calculated *ab initio*. To simplify matters, spectral line strengths are determined from experimental measurements usually made in a multi-pass gas cell of known pressure, temperature, and path length. These empirically determined line strengths are catalogued for general use in databases such as HITRAN [16] and JPL [17].

Spectral line strengths are usually tabulated for the reference temperature of $T_0 = 296$ K. The line strength can be corrected for temperature, $T$, and for stimulated emission with [18]

$$S(T) = S_0 \left(\frac{T_0}{T}\right)^m \left(\frac{\sigma}{\sigma_0}\right) \left(\frac{1-\exp(\frac{-hc\sigma}{k_B T})}{1-\exp(\frac{-hc\sigma_0}{k_B T_0})}\right) \left(\frac{1+\exp(\frac{-hc\sigma_0}{k_B T_0})}{1+\exp(\frac{-hc\sigma}{k_B T})}\right) \left(\frac{\exp(\frac{-E}{k_B T})}{\exp(\frac{-E}{k_B T_0})}\right) \tag{2.38}$$

in units of $\text{cm}^{-1}(\text{molecules}\cdot\text{cm}^{-2})^{-1}$ and where $S_0$ is the tabulated line strength, $k_B$ is Boltzmann's constant, $h$ is Planck's constant, and $E$ is the lower energy state of the transition in $\text{cm}^{-1}$. The value, $m$ describes the temperature dependence of the rotation partition function, and depends on the molecular species [19]. The $m$ values for several common species are given in table 2.2.

| Molecule | m |
|---|---|
| $H_2O$ | 1.5 |
| $CO_2$ | 1.0 |
| $O_3$ | 1.5 |
| $N_2O$ | 1.0 |
| CO | 1.0 |
| $CH_4$ | 1.5 |
| $O_2$ | 1.0 |

Table 2.2: Temperature dependence of rotational partition function for common molecular species.

Using equations 2.23 and 2.27 and the definitions of line shape and line strength given above, the transmission and emission of radiation in individual layers in a model atmosphere can be calculated. The results from individual layers can be combined to produce a spectrum for a multi-layer atmosphere. The development of the multi-line, multi-layer radiative transfer model of the atmosphere is discussed in Chapter 3.

## 2.5 Curve-of-Growth

### 2.5.1 Curve-of-Growth: Theory

The total radiance measured by a radiometer is found by integrating equation 2.26 over the spectral range of interest. In the case where the integral is taken over all wavenumbers, the total radiance is

$$L = \int_0^\infty B_\sigma (1 - e^{-k_\sigma n_{av} l})\, d\sigma \qquad \text{W m}^{-2}\,\text{sr}^{-1}\,(\text{cm}^{-1})^{-1} \tag{2.39}$$

In the optically thin, or low opacity limit, $\tau \gg 1$, the ground-level radiance is found from equation 2.39 by taking $e^{-\tau} \cong 1 - \tau = 1 - k_\sigma n_{av} l$. The total radiance of a

spectral line then becomes [20]

$$L = S\ n_{av}\ l \int_0^{\infty} B_\sigma\ d\sigma \qquad \text{W m}^{-2}\ \text{sr}^{-1}\ (\text{cm}^{-1})^{-1} \tag{2.40}$$

The *equivalent width* or *integrated absorptance*, $W$, of a spectral line in the optically thin limit or weak regime is given by [11]

$$W = S\ n_{av}\ l \qquad \text{cm}^{-1} \tag{2.41}$$

In the optically thick, or high opacity limit, $\tau >> 1$, the radiance has the form [20]

$$L = 2\sqrt{S\ \gamma\ n_{av}\ l} \int_0^{\infty} B_\sigma\ d\sigma \qquad \text{W m}^{-2}\ \text{sr}^{-1}\ (\text{cm}^{-1})^{-1} \tag{2.42}$$

where $\gamma$ is the half-width of the spectral line under standard conditions (STP). This half-width is usually the same as the Lorentz half-width, $\gamma_L$. The equivalent width, $W$, of a spectral line in the optically thick limit or strong regime is given by [11]

$$W = 2\sqrt{S\ \gamma\ n_{av}\ l} \qquad \text{cm}^{-1}$$

For cases between these extremes, the integral in equation 2.39 can be evaluated analytically, and the result is known as the Ladenberg-Reiche equation [20]

$$L = 2\pi\gamma x e^{-x}[J_0(x) + J_1(x)] \qquad \text{W m}^{-2}\ \text{sr}^{-1}\ (\text{cm}^{-1})^{-1} \tag{2.43}$$

where $J_0(x)$ and $J_1(x)$ are the Bessel functions of order zero and one respectively, and imaginary argument. The quantity $x$ is given by

$$x = \frac{Su}{2\pi\gamma} \tag{2.44}$$

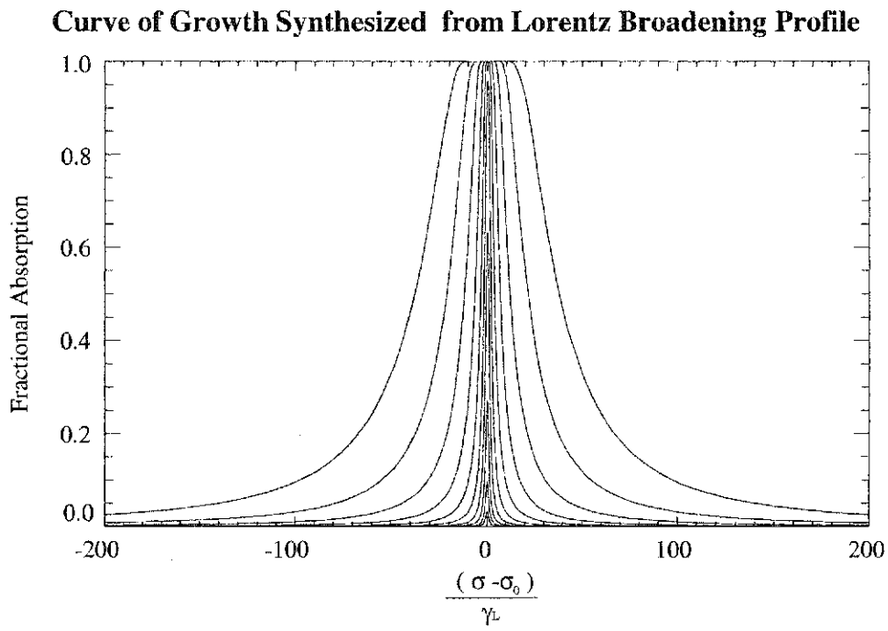


Figure 2.7: The simulated emission from a Lorentz broadened line at increasing absorber amounts.

where

$$u = \int_0^l n(z)\, dz = n_{av} l \qquad \text{molecules} \cdot \text{cm}^{-2} \tag{2.45}$$

is the absorber amount along an atmospheric path of length $l$ and average absorber density $n_{av}$.

The integrals in equations 2.39, 2.40, and 2.42 are for the wavenumber range of $[0,\infty]$, but in practice, for a band limited optical system, these integrals are only evaluated over the passband of the system as determined by the combined detector-filter response.

The total radiance of a spectral line can be plotted as a function of the abundance of the emitting species, or absorber amount. This plot is known as a *curve-of-growth*. An

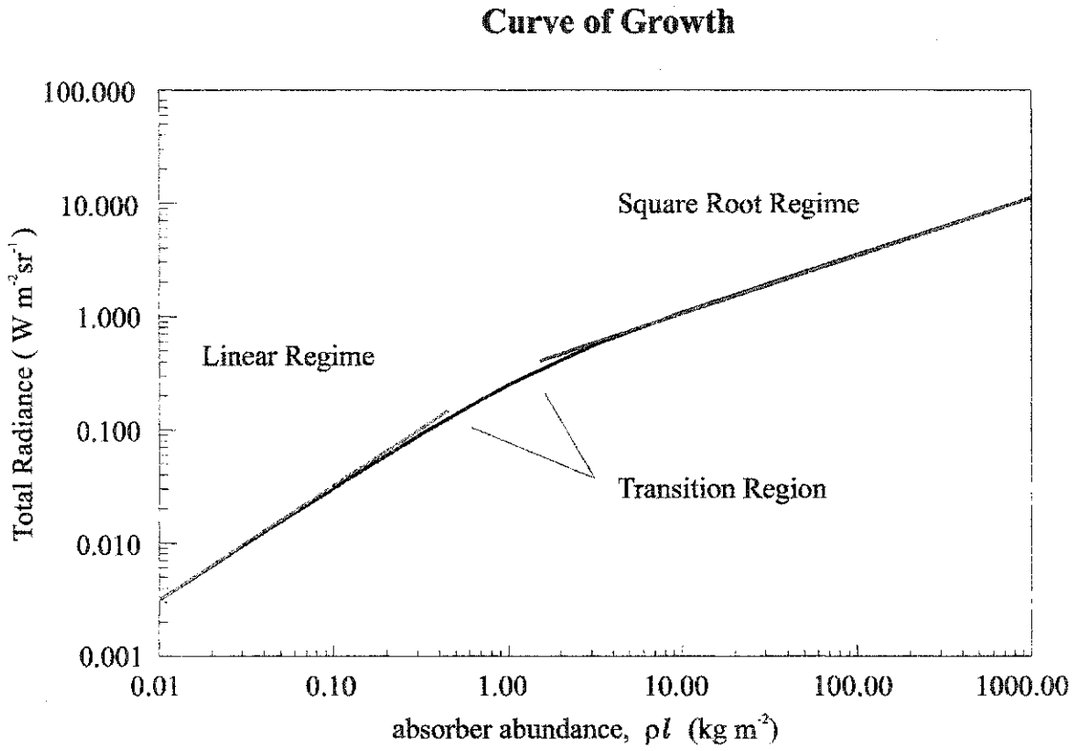


Figure 2.8: The curve-of-growth generated from a Lorentz broadened emission line for increasing absorber amounts.

IDL® program was written to compute the curve-of-growth of a single Lorentz broadened spectral line. A Lorentz half-width of 0.1 $cm^{-1}$ and a normalized Planck radiance of 1 were arbitrarily selected for use in the numerical simulation. Absorber amount was varied by increasing the path length, $l$, and leaving all other parameters (i.e. $P$, $T$, $n$) constant. Figure 2.7 shows the simulated spectral line for increasing absorber amounts while figure 2.8 shows the corresponding curve-of-growth.

When the emission and absorber amount are plotted on logarithmic scales, the curve-of-growth clearly shows the two limiting regimes from equations 2.40 and 2.42. These

equations describe a weak and a strong regime. In the weak regime, the area under the emission line grows linearly with increasing absorber amount. As the absorber amount continues to increase, the line eventually saturates as it reaches the Planck curve evaluated at the local atmospheric temperature. Further increase in the absorber amount only widens the saturated spectral line. At high levels of saturation (i.e. in the strong regime), the integrated area of the emission line increases as the square root of the absorber abundance.

Because of the reduction in sensitivity to changes in absorber amount in the strong regime, radiometers are most effective when small amounts of the absorbing species are present, ensuring that the emission occurs in the weak regime. These conditions are frequently met for water vapour at high altitude sites, such as Mauna Kea and the Atacama plateau.

The sensitivity of an infrared radiometer can be enhanced by selecting a bandpass that includes a large number of spectral lines. In the case of IRMA, the 20 $\mu$m region was selected for its numerous water vapour lines. The curve-of-growth associated with this region can be quite complicated, as many of the spectral lines saturate at different absorber amounts. Although the curve-of-growth can not be described analytically, it will have the same general form as that displayed in figure 2.8.

### 2.5.2 Obtaining a Curve-of-Growth With an Infrared Radiometer

To obtain a curve-of-growth, the absorber amount viewed by a radiometer must be varied in a known way and plotted against the corresponding signal. In the laboratory,

this can be accomplished using a multi-pass gas cell, varying either the absorber amount in the cell, or increasing the number of passes. Using a gas cell has the advantage of keeping broadening conditions constant while the absorber amount is varied in a well-known way. In the atmosphere, there is no way to arbitrarily choose the amount of absorber (water vapour in the case of IRMA) viewed by the radiometer. Variation of water vapour amount in the atmosphere is accomplished using a method known as *skydipping*. If the vertical pressure, temperature, and absorber amount profiles can be assumed to be constant for a local section of atmosphere, then the observed absorber amount can be varied by tipping the radiometer through a range of zenith angles, thereby increasing the path length.

Figure 2.9 illustrates the skydipping technique of obtaining a curve-of-growth with a radiometer. In this figure the effective path length is defined by the zenith angle, $\theta$, is given by

$$l = \frac{h}{\cos\theta} \tag{2.46}$$

where $h$ is the height of the atmosphere. By definition, the radiometer views 1 airmass, corresponding to a path length of $h$, when it points to the zenith. For arbitrary zenith angles the path length can then be written as

$$l = \mathrm{A}h \tag{2.47}$$

where $\mathrm{A} = \frac{1}{\cos\theta}$ is airmass. If the atmosphere is horizontally homogeneous and is characterized by an average absorber number density of $n_{av}$, then the absorber column abundance, $u$ (molecules·cm$^{-2}$), viewed by the radiometer along the line-of-sight at any zenith angle is

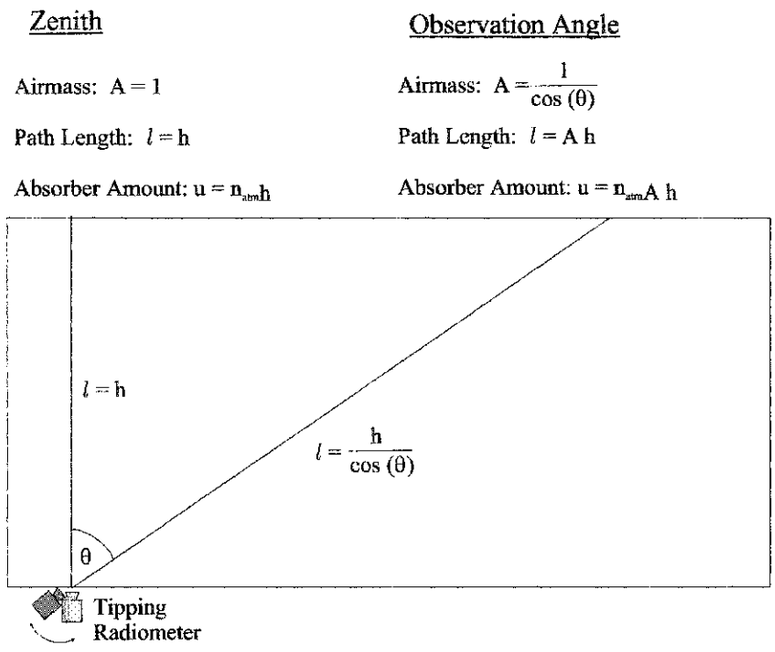


Figure 2.9: A curve-of-growth is obtained using the skydip method, in which a radiometer tips through a range of zenith angles through a horizontally homogeneous atmosphere.

related to the zenith absorber amount, $u_{zenith}$, by

$$u = u_{zenith}\ \mathrm{A} \qquad (\mathrm{molecules} \cdot \mathrm{cm}^{-2}) \tag{2.48}$$

where

$$u_{zenith} = n_{av}\ h \qquad (\mathrm{molecules} \cdot \mathrm{cm}^{-2}) \tag{2.49}$$

IRMA II was operated between December, 2000 to March, 2001 at the James Clerk Maxwell Telescope (JCMT) on the summit of Mauna Kea. During this time ~2000 skydips were obtained. The analysis of these skydips and the construction of a curve-of-growth are discussed in Chapter 5.

# Chapter 3

# Atmospheric Radiative Transfer Model

## 3.1 Overview

This chapter deals with the development of a radiative transfer model of the atmosphere of the earth in IDL®. Section 3.2: FASCODE Radiative Transfer Model describes the FASCODE radiative transfer model and discusses its strengths and weaknesses. Section 3.3: Atmospheric Modelling describes the methods used to calculate pressure, temperature, and density for the individual layers of the atmospheric model. Section 3.4: Line Shape Modelling describes the process of calculating the Voigt line shape, the water vapour line shape, and water vapour continuum. Section 3.5: University of Lethbridge Transmittance and Radiance Model discusses the line-by-line, layer-by-layer algorithm of the model and presents results of the modelling program, including a comparison with the FASCODE

model.

## 3.2 FASCODE Radiative Transfer Model

Beginning in the 1970's, there was an effort to develop a fast radiative transfer model for the purposes of analyzing the spectral characteristics of the atmosphere. This model is known as the Fast Atmospheric Signature Code or by its acronym, FASCODE [9]. The FASCODE radiative transfer model has its origins in the atmospheric research division of the United States Air Force. Its original purpose was to allow for the identification of the spectral signatures of the exhaust emissions of enemy weapon systems.

FASCODE is a well known radiative transfer model of the atmosphere which finds frequent use by researchers. The model has some flexibility with six different built-in atmospheric profiles of pressure, temperature, and molecular densities as a function of altitude. These atmospheric profiles are specific to certain geographic regions such as the tropics or mid-latitudes. The model also allows for a user defined atmospheric profile. FASCODE is also flexible in terms of the atmospheric path travelled by the radiation (e.g. ground to sky, sky to ground, sky to sky); the path can start and end at any altitude along any zenith angle.

While FASCODE is a general purpose tool for radiative transfer modelling, it has two principal limitations that reduce its effectiveness for modelling the transmission spectrum of the atmosphere above Mauna Kea. The first limitation is that the program is general, rather than location-specific, because it was developed to model the atmosphere in any geographic area of the world. In particular, as shown in § 3.3.4, the atmosphere above

Mauna Kea is significantly different than the tropical atmospheric profile in the FASCODE database.

The second principal limitation of FASCODE is that it was developed with the goal of simulating essentially an infinite number of observing geometries. As a result of this flexibility, FASCODE is well over 1000 pages of user-unfriendly Fortran code. The main program itself has 71,000 lines of code and is 700 pages long. Because of its size, it is not easy to make sensible changes to FASCODE and understand their impact throughout the program.

FASCODE has proven useful as a radiative transfer model; however, it is too general to model accurately the atmosphere above Mauna Kea. These limitations created the impetus for the development of a simpler radiative transfer model in a modern computer language. The goals of developing a new model were to allow for a *user-definable model atmosphere* and to produce a well documented, user-friendly code. The development of the radiative transfer model, which was written in the fourth generation language Interactive Data Language (IDL®) [10], found in many active research environments, will be detailed in the following sections of this chapter.

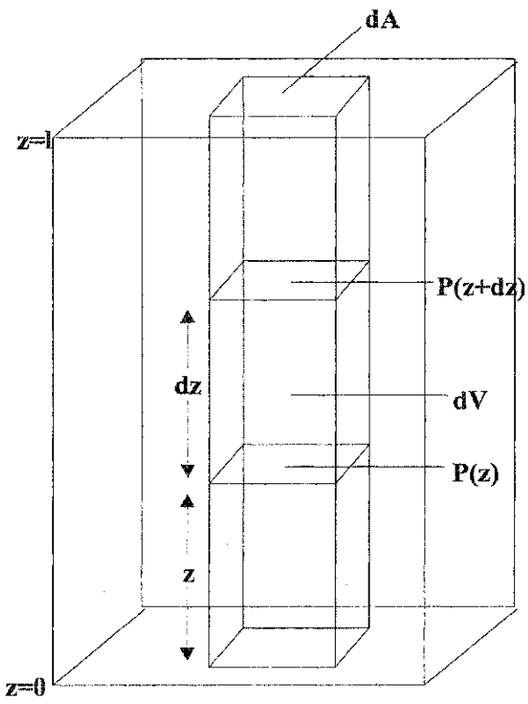


**Definition of pressure differential**
$dP = P(z+dz) - P(z)$

**Buoyant force on volume element dV**
$F_B = [P(z) - P(z+dz)]\, dA$
$= -dP\, dA$

**Gravitational force on volume element dV**
$F_g = -mg = -\rho(z)\, dz\, dA\, g$

**Equilibrium condition $F_B + F_g = 0$ yields the hydrostatic equation:**
$dP = -g\, \rho(z)\, dz$

Figure 3.1: The hydrostatic equation describes the gravitationally induced vertical density profile $\rho = \rho(z)$ where $z$ is the altitude measured from ground level.

## 3.3 Atmospheric Modelling

### 3.3.1 Pressure, Density, and the Hydrostatic Equation

The atmosphere is bound to the earth by the gravitational field such that its pressure and density both decrease with increasing altitude. In the following analysis the atmosphere is assumed to be in static equilibrium. Under this assumption, the pressure, $p$, of the atmosphere at an altitude $z$ can be found from the hydrostatic equation [11]

$$dp = -g\rho dz \tag{3.1}$$

where

$$g(z) = \frac{GM_E}{(R_E + z)^2} \qquad \mathrm{m \cdot s^{-2}} \tag{3.2}$$

is the acceleration due to gravity at altitude $z$. In equation 3.2, $G = 6.673 \times 10^{-11}$ $\mathrm{m^3 \cdot kg^{-1} \cdot s^{-2}}$ is the Newtonian constant of gravitation, $M_E = 5.974 \times 10^{24}$ kg is the mass of the earth, and $R_E = 6.378 \times 10^6$ m is the radius of the earth. At sea level, $g(0) = 9.800$ $\mathrm{m \cdot s^{-2}}$. As one moves upwards in the atmosphere, the value of $g$ declines. At the summit of Mauna Kea, at an altitude of 4092 m, $g(4092) = 9.787$ $\mathrm{m \cdot s^{-2}}$. In the upper-most part of the atmosphere, at an altitude of 50 km, the acceleration due to gravity is $g(50\ \mathrm{km}) = 9.648$ $\mathrm{m \cdot s^{-2}}$.

From the equation of state for a perfect gas, the density, $\rho$, of the atmosphere is

$$\rho = \frac{M_r p}{RT} \qquad \mathrm{kg \cdot m^{-3}} \tag{3.3}$$

where $M_r$ is the molar mass of the gas in $\mathrm{kg \cdot mol^{-1}}$, $p$ is the pressure in Pa, $R = 8.314$ $\mathrm{J \cdot mol^{-1} \cdot K^{-1}}$ is the universal gas constant, and $T$ is the temperature in Kelvin.

Expressed in terms of density, equation 3.1 becomes

$$\frac{dp}{p} = \frac{-dz}{H} \tag{3.4}$$

where $H = \frac{RT}{M_r g}$ is known as the *scale height* in m. This scale height represents the increase in altitude corresponding to a decrease in pressure by a factor of $e$, and is itself a function of altitude since $M_r$, $g$, and $T$ are all altitude dependent. The variation of temperature, $T$, with altitude is discussed in § 3.3.2.

Equation 3.4 can be integrated to give the pressure at an altitude of $z$ as

$$p(z) = p_0 e^{\int_{z_0}^{z} \frac{dz}{H(z)}} \quad \text{mbar} \tag{3.5}$$

where $p_0$ is the pressure at a reference altitude. Since the density of the gas is directly proportional to the pressure, it can be calculated using the formula

$$\rho(z) = \rho_0 e^{\int_{z_0}^{z} \frac{dz}{H(z)}} \quad \text{kg} \cdot \text{m}^{-3} \tag{3.6}$$

where $\rho_0$ is the density at the reference altitude of $z_0$.

Finally, *number density, n(z)* is related to pressure by the equation

$$n(z) = \frac{p(z)}{k_B T(z)} \quad \text{molecules} \cdot \text{m}^{-3} \tag{3.7}$$

where $k_B = 1.381 \times 10^{-23}$ J·K$^{-1}$ is the Boltzmann constant, and $T(z)$ is the temperature in K.

Using equations 3.5 and 3.7, it is straight forward to calculate the pressure and molecular number density at any altitude in the atmosphere. However, in order to calculate the overall transmission and emission, it is necessary to divide the atmosphere into layers such that several layers span each scale-height-sized section in the atmosphere. Furthermore, the atmosphere in each layer is treated as being homogeneous throughout the layer by finding *equivalent values* for each of the atmospheric parameters.

Since pressure and number density do not vary linearly through the layer, a simple average of the layer boundary values of these quantities is, in general, not adequate to describe the overall conditions of the layer. An equivalent pressure can be found for each

layer by calculating a *weighted average* of the pressure throughout the layer. The weighted average of pressure in a layer is found by [11]

$$\overline{P} = \frac{\int p \; du}{\int du} \qquad \text{mbar} \tag{3.8}$$

where $du = n(z) \; dz$. This averaging procedure is known as the *Curtis-Godson approximation.*

In essence, equation 3.8 accounts for the fact that pressure is not linearly dependent on altitude. From the equivalent pressure, an equivalent density, $\overline{\rho}$, can be calculated from equation 3.3 and an equivalent number density, $\overline{n}$, can be calculated from equation 3.7 using the average temperature from equation 3.19 in the next section. The equivalent layer values of pressure, temperature, and density define the *physical characteristics* of the layer and are the inputs to the radiative transfer program.

### 3.3.2 Atmospheric Temperature Profile

If an element of gas moves adiabatically in the atmosphere, the first law of thermodynamics requires that

$$c_v \; dT = -p \; dV \tag{3.9}$$

where $c_v$ is the specific heat capacity of the atmosphere at a constant volume in $\text{J}\cdot\text{kg}^{-1}\cdot\text{K}^{-1}$. If $V$ is the *specific volume* containing a gram of molecules, then the ideal gas law gives

$$dV = \frac{N_0 k_B}{p} \; dT - \frac{N_0 k_B T}{p^2} \; dp \tag{3.10}$$

where $N_0 = 1/M$ and $M$ is the molecular mass of the atmosphere. Since $c_p = c_v + N_0 k_B$, equation 3.10 can be rewritten as

$$c_p \, dT = \frac{N_0 k_B T}{p} \, dp = V \, dp = \frac{1}{\rho} \, dp \tag{3.11}$$

Using the hydrostatic equation (equation 3.1), a relation between height and atmospheric temperature can be defined [11]

$$\frac{dT}{dz} = \frac{-g}{c_p} = -\Gamma_d \qquad \mathrm{K \cdot m^{-1}} \tag{3.12}$$

where $c_p$ is the specific heat capacity of the atmosphere at constant pressure in $\mathrm{J{\cdot}kg^{-1}{\cdot}K^{-1}}$ and $\Gamma_d$ is known as the *adiabatic lapse rate*. For dry air, $c_p = 1005$ $\mathrm{J{\cdot}kg^{-1}{\cdot}K^{-1}}$, which gives an adiabatic lapse rate of $\Gamma_d \simeq 10$ $\mathrm{K{\cdot}km^{-1}}$. This means that for every increase in altitude of 1 km, the temperature of the atmosphere drops by 10 K.

Equation 3.12 excludes water vapour from the atmosphere. Water can exist as solid, liquid, or gas in the atmosphere. When the presence of water in the atmosphere is taken into account, a *wet adiabatic lapse rate* is given by [21]

$$\frac{dT}{dz} = \frac{-g/c_p}{1 + (L/c_p)(dw_s/dT)} = -\Gamma \qquad \mathrm{K \cdot m^{-1}} \tag{3.13}$$

where $w_s$ is the mass of saturated water per mass of air and $L$ is the latent heat of vaporization. The wet lapse rate is about half the dry lapse rate, around 5 $\mathrm{K{\cdot}km^{-1}}$.

The sizable temperature gradient in the atmosphere leads to convection of both dry air and wet air, resulting in a mix of temperature gradients. Due to this convective mixing, the troposphere has an average lapse rate of 6.5 $\mathrm{K{\cdot}km^{-1}}$ [21]. Recent measurements by balloon-borne radiosondes launched from Hilo, Hawaii have shown that the atmosphere

above Mauna Kea has an average lapse rate of about 5.6 K $km^{-1}$ [22]. This was confirmed by an analysis of 80 radiosondes launched from Hilo airport in 1999. The radiosonde data were averaged together and an IDL program was written to find the lapse rate of the average pressure-temperature curve (shown as the black line in figure 3.2). The average lapse rate for the atmosphere above Mauna Kea was determined to be 5.7 $\pm$ 0.9 K·$km^{-1}$. The theoretical pressure-temperature curve with a lapse rate of 5.7 K $km^{-1}$ used by ULTRAM is shown in the figure as the green line, while the error is represented by the red curves. The pressure-temperature curve from the FASCODE tropical atmosphere profile is shown as a blue line in figure 3.2. The pressure-temperature curve used by ULTRAM is much closer to the average of the radiosonde data than the FASCODE curve.

In the lower atmosphere, the temperature decreases with increasing altitude. In the upper atmosphere, however, it is important to consider a number of reactions involving oxygen, known as the *Chapman reactions* [21]. Molecular oxygen is photodissociated by absorption in the Herzberg continuum according to

$$O_2 + h\nu \rightarrow 2O \tag{3.14}$$

The atomic oxygen then bonds to $O_2$ in the presence of an unspecified third body, M, to form ozone

$$O + O_2 + M \rightarrow O_3 + M \tag{3.15}$$

Both O and $O_3$ are destroyed by

$$O + O_3 \rightarrow 2O_2 \tag{3.16}$$

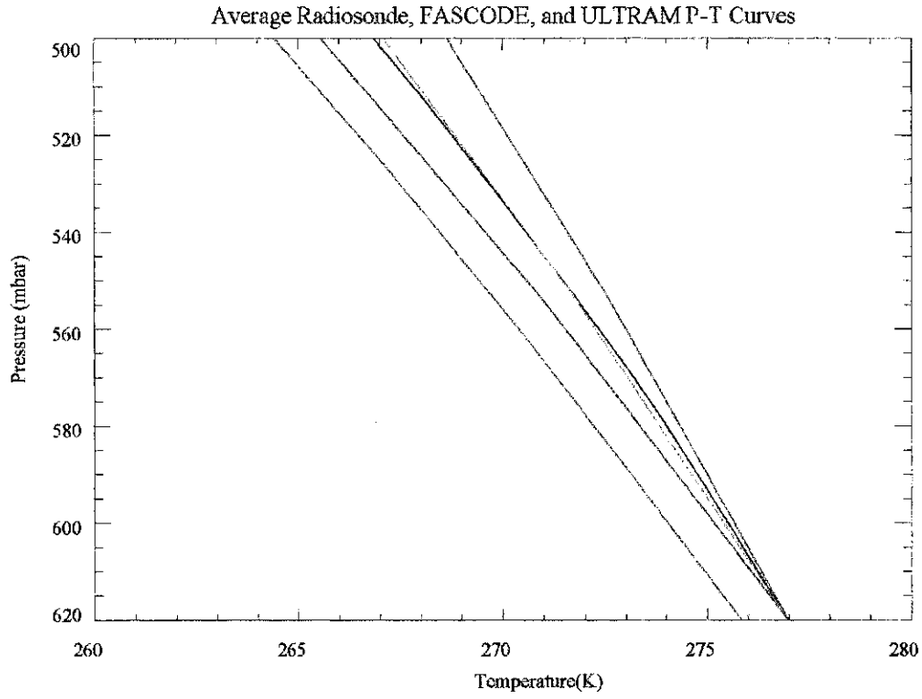


Figure 3.2: A comparison of the average of radiosonde data above Mauna Kea (black) with the pressure-temperature curves from the FASCODE tropical atmosphere profile (blue) and ULTRAM (green) calculated with a lapse rate of 5.7 $\pm$ 0.9 K/km. The error in the ULTRAM lapse rate is represented by the pair of red lines.

and $O_3$ is converted back to O by, among other processes

$$O_3 + h\nu \rightarrow O_2 + O \tag{3.17}$$

resulting in a temperature increase. This increased temperature creates an *inversion layer*, effectively decoupling the lower atmosphere (*troposphere*) from the *stratosphere*. The highest concentrations of ozone are found in the stratosphere (10 - 50 km) with peak ozone levels at an altitude of $\sim$25 km in the tropics. The principle source of heating in the ozone layer is due to the ozone dissociation as shown in equation 3.17. Since the increase in temperature is non-linear and dependent on latitude (as is the concentration of ozone),

modelling the temperature is difficult at these altitudes. In this thesis, the temperature of the atmosphere at altitudes where ozone heating is significant has been taken from the tabulated temperature data in the tropical atmosphere model in FASCODE.

In ULTRAM, the temperature at a layer boundary at altitude $z$ is given by

$$T(z) = T_0 - \Gamma \cdot z \qquad \text{K} \tag{3.18}$$

where $T_0$ is the base temperature and $\Gamma$ is the temperature lapse rate of 5.7 K·km$^{-1}$. Above an altitude of 12 km, heating due to the absorption of ultraviolet radiation by ozone leads to an increase in temperature and, as mentioned above, temperature data for this region have been taken from the tropical atmospheric model in FASCODE.

Other computations in the model are simplified if the temperature is constant through a layer. Since the temperature varies almost linearly with altitude, the equivalent temperature of a layer is found by taking the average of the temperatures at the layer boundaries

$$\overline{T} = \frac{T(z) + T(z+dz)}{2} \qquad \text{K} \tag{3.19}$$

This is the equivalent temperature of the layer mentioned in § 3.3.1.

### 3.3.3 Molecular Constituents in the Atmosphere

This thesis is primarily concerned with two spectral regions: the submillimeter region (5 cm$^{-1}$ – 35 cm$^{-1}$) and the mid-infrared region (475 cm$^{-1}$ – 575 cm$^{-1}$). The primary absorbing molecular species in the submillimeter region are water vapour, molecular

oxygen, and ozone. In the mid-infrared region, the primary absorbers are water vapour, carbon dioxide, and nitrous oxide ($N_2O$).

ULTRAM adopted the FASCODE formalism in which tabulated values of *mixing ratios* are stored in the atmospheric model database. The volume mixing ratio is defined as the ratio of the number of molecules of a certain species, $N_g$, to the total number molecules, $N_T$

$$r = \frac{N_g}{N_T} \tag{3.20}$$

The mixing ratio for a given absorber varies with height, so the mixing ratios at the boundaries of a layer have been determined through spline interpolation. By choosing sufficiently thin layers (i.e. with several per scale height), an equivalent mixing ratio, equal to the average of the mixing ratios at the layer boundaries, can be assigned to each layer

$$\overline{r} = \frac{r(z) + r(z+dz)}{2} \tag{3.21}$$

This mixing ratio is used to calculate the average number density of molecules of a certain species, $\overline{n_g}$, in a layer by

$$\overline{n_g} = \overline{r}\,\overline{n} \qquad \text{molecules} \cdot \text{cm}^{-3} \tag{3.22}$$

where $\overline{n}$ is the average number density of all molecules in the layer. A column abundance of a certain species, $du_g$, for the layer can then be calculated, giving

$$du_g = \overline{n_g}\, dz \qquad \text{molecules} \cdot \text{cm}^{-2} \tag{3.23}$$

ULTRAM determines the column abundances of oxygen, carbon dioxide, and ozone using the tabulated mixing ratios from the FASCODE tropical atmospheric model. First,

the mixing ratios at the layer boundaries are found by spline interpolation of the tabulated data. Average mixing ratios for each molecule are determined using equation 3.21 and these are used to determine average molecular number densities with equation 3.22. Finally, molecular column abundances for each molecule are determined from equation 3.23.

Water vapour is a minor constituent of the troposphere with concentrations often measured in parts per million. However, it is a major contributor in both spectral regions of interest. The distribution of water vapour is not well known; unlike the other gases discussed, water vapour is highly polar and can form strong intermolecular hydrogen bonds. These intermolecular hydrogen bonds often lead to the clustering of the water vapour molecules, forming polymers and, ultimately, raindrops. One might expect that water vapour should be distributed exponentially with a scale height found by

$$H_{H_2O} = \frac{RT}{gM_{H_2O}} \quad \text{km} \tag{3.24}$$

where $M_{H_2O} = 18.02$ g·mol$^{-1}$ is the molar mass of water. At the summit of Mauna Kea, where temperatures are typically near 270 K and $g = 9.787$ m·s$^{-2}$, equation 3.24 gives a scale height for water vapour of $H_{H_20} = 12.73$ km. However, this scale height is much larger than the scale height of water vapour observed in the real atmosphere, $H_{H_2O} \simeq 2$ km. This reduction in the scale height is due to the fact that water vapour precipitates out of the atmosphere at relatively high temperatures compared to other gases.

In this approximation, the number density of water vapour at height $z$ can be expressed as

$$n_{H_2O}(z) = n_{H_2O,0}\, e^{-\frac{z}{H_{H_2O}}} \quad \text{molecules} \cdot \text{cm}^{-3} \tag{3.25}$$

where $n_{H_2O,0}$ is the number density of water vapour at the base altitude and $H_{H_2O} = 2$ km. Following the previous analysis, a Curtis-Godson approximation can be used to give an average number density of water vapour in a layer.

Another measure of the amount of water vapour in the atmosphere is known as the *precipitable water vapour* (pwv). If all of the water vapour in a column of atmosphere above a unit area was condensed into a container, then the precipitable water vapour is the depth of the condensed water in millimeters (mm).

Another convenient measure of the amount of a species in the atmosphere is known as *partial pressure.* The partial pressure of a species is the pressure exerted only by molecules of the species of interest. The partial pressure, $e_g$, is related to the volume mixing ratio by

$$e_g(z) = r(z)\ p(z) \qquad \text{mbar} \tag{3.26}$$

where $p(z)$ is the pressure at the same altitude as the mixing ratio, $r(z)$. An average partial pressure can be computed by simply replacing the values in equation 3.26 with their respective averages.

### 3.3.4 Comparison of ULTRAM Atmosphere to Hilo Radiosondes

Figure 3.3 shows the average pressure-temperature curve determined from 80 radiosondes launched from Hilo airport, located nearby Mauna Kea. The black curve in the figure is the average pressure-temperature curve, while the red curves represent a $1\sigma$ error. The green curve in the figure shows the pressure-temperature curve from the atmospheric

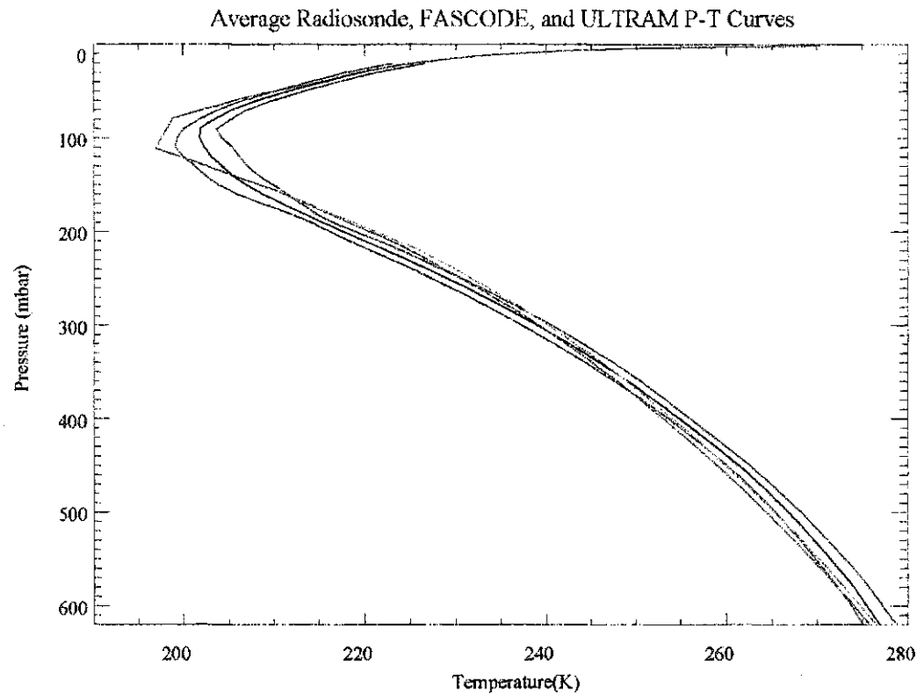


Figure 3.3: A comparison of the average of the radiosonde data (black) with the pressure-temperature curve from the FASCODE tropical atmosphere model (blue) and the pressure-temperature curve of ULTRAM (green). The standard deviation of the radiosonde data is shown in red.

model of ULTRAM. This curve was determined from equations 3.5 and 3.18 using a pressure of 625 mbar, an air temperature of 273 K, and a lapse rate of 5.7 K $km^{-1}$, typical conditions at the summit of Mauna Kea.

The theoretical pressure-temperature curve fits well with the average of the radiosonde data. From this, it can be seen that the atmospheric model used by ULTRAM is in close agreement with the measured profile of the atmosphere above Mauna Kea.

## 3.4 Radiative Transfer Model

### 3.4.1 Spectral Line Shape in the Real Atmosphere

In § 2.4.2, several broadening mechanisms and their associated line shapes were discussed. Both the Lorentz and Doppler line shapes must be considered when modelling spectral lines in the atmosphere. The Lorentz line shape is dominant at the lower altitudes where the pressure is high and molecular collisions occur more frequently. The Doppler line shape becomes dominant in the upper atmosphere where the pressure is lower, reducing the Lorentzian contribution to line width.

In the mid-altitude atmosphere, where neither Lorentz nor Doppler are dominant, the Voigt line shape, shown in figure 3.4, is used. The Voigt line shape, a convolution of the Lorentz and Doppler shapes, resembles the broad Lorentz shape at high pressures. At low pressures the Voigt shape closely resembles the thinner Doppler shape. Between the Doppler and Lorentz regimes, the Voigt shape is a mix of both line shapes, with a strong central component similar to the Doppler shape and broad wings reflecting the Lorentz component. The equation for the Voigt line shape is [23]

$$f(\sigma - \sigma_0) = \frac{a}{\gamma_D \sqrt{\pi^3}} \int_{-\infty}^{\infty} \frac{e^{-y^2}}{a^2 + (q - y)^2} dy \quad \text{cm} \tag{3.27}$$

where

$$a = \frac{\gamma_L}{\gamma_D} \tag{3.28}$$

and

$$q = \frac{\sigma - \sigma_0}{\gamma_D} \tag{3.29}$$

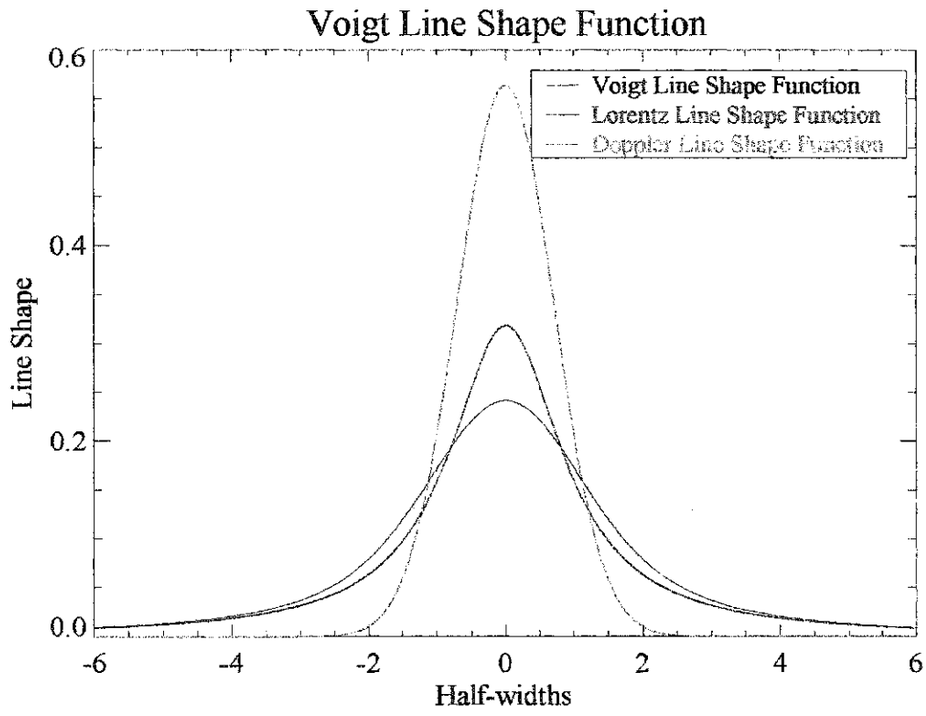


Figure 3.4: A comparison of the Voigt line shape function (black), the Doppler line shape function (orange), and the Lorentz line shape function (red).

In figure 3.4, the Voigt line shape function is calculated using Doppler and Lorentz line shapes of the same half-width. All three of the line shapes in the figure were normalized to unit area so that they all represent the same amount of absorption.

The Voigt line shape is the best representation of the actual line shape for most spectral lines in the atmosphere. It accurately reproduces the Doppler-dominated shape of ozone lines as well as the broad, Lorentz-dominated line shape of water vapour lines. It would be challenging to develop a numerical method of integration for this function. Fortunately, IDL® has a built in routine to calculate the value of the Voigt function at any distance from the line center and this has been used to calculate line shapes in the present

model.

One problem with the Voigt line profile is that is does not accurately model the behavior of water vapour lines [24]. The special line shape used to model water vapour is discussed in the next section.

### 3.4.2 Water Vapour Spectral Line Shape and Continuum

The shape of water vapour lines is radically different from that of any other species. Since water vapour is only found in the lower reaches of the atmosphere, its line shape somewhat resembles the pressure broadened Lorentzian profile. However, the line wings are significantly stronger than any other species. In fact, these line wings often extend beyond 25 $cm^{-1}$ from the line center.

The strong line wings of water vapour are thought to be due to the strong polar nature of this molecule [24] which allows it to form strong associations with other water molecules in the atmosphere. Due to their polar nature, water vapour molecules experience prolonged interactions during collisions. The Lorentz line shape is a good representation for those molecules where collisions are instantaneous but it cannot accurately describe the line shape of the spectral lines of water vapour.

Following the work of Clough, Kneizys, and Davies (CKD) [24], the water vapour line shape is expressed with an absorption coefficient of

$$k_{H_2O} = k_{line} + k_{cont} \tag{3.30}$$

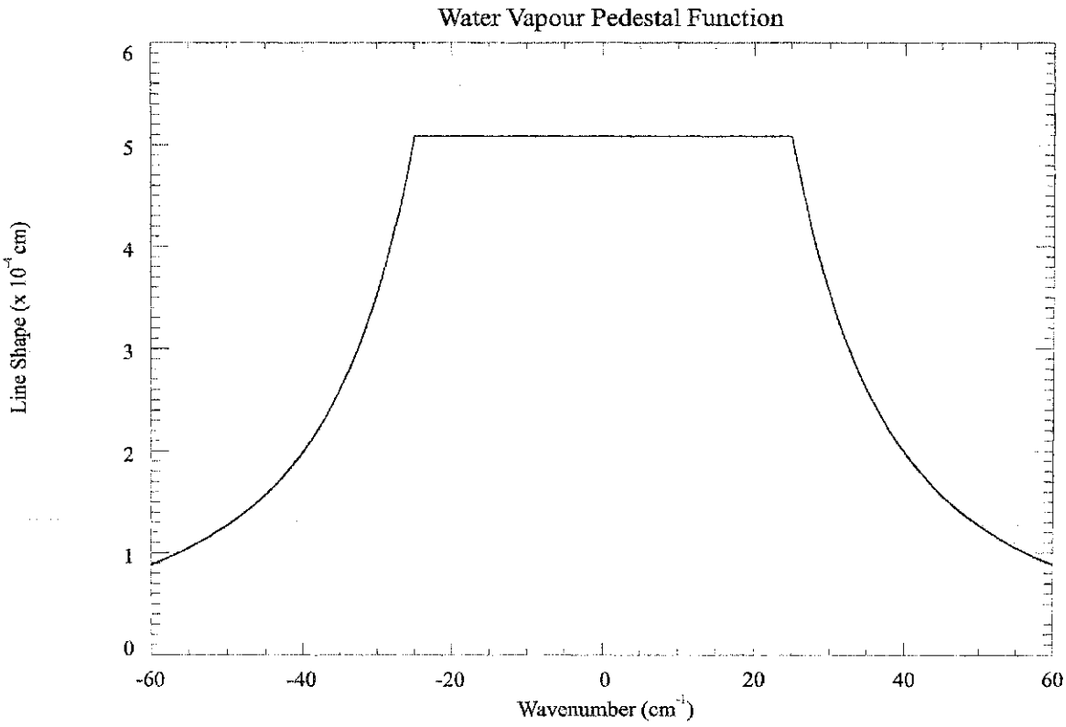


Figure 3.5: A plot of the pedestal function subtracted from the line shape function of water vapour.

where $k_{line}$ is the absorption coefficient for line shape and $k_{cont}$ is an empirical correction term known as the *water vapour continuum*. The CKD continuum coefficients used in this thesis were obtained from version 3 of the FASCODE program [25].

The theoretical portion of the water vapour line shape, $f_{line}$, is given by the Voigt line shape with a pedestal-shaped function subtracted from it. The pedestal shape function is given by [24]

$$f_{pedestal} = \frac{1}{\pi} \frac{\gamma_L}{25^2 + \gamma_L^2} \quad \text{cm} \tag{3.31}$$

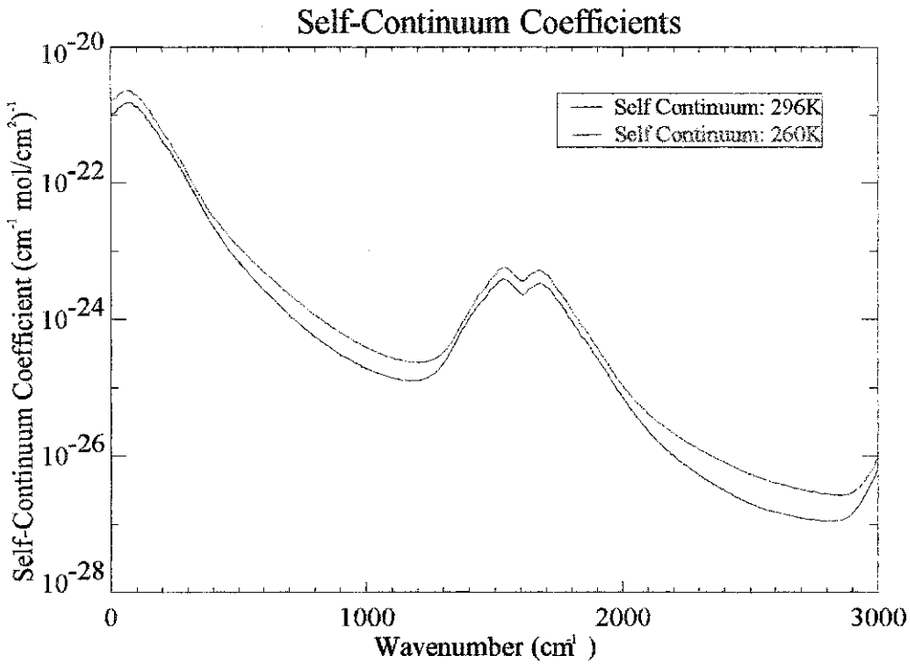


Figure 3.6: A plot of the CKD self-continuum coefficients.

for $|\sigma \mp \sigma_0| \leq 25$ cm$^{-1}$ and

$$f_{pedestal} = \frac{1}{\pi} \frac{\gamma_L}{(\sigma \mp \sigma_0)^2 + \gamma_L^2} \quad \text{cm} \tag{3.32}$$

for $|\sigma \mp \sigma_0| \geq 25$ cm$^{-1}$, where $\gamma_L$ is the half width of the Lorentz line shape and $\sigma_0$ is the line center wavenumber. Figure 3.5 shows the pedestal function for the Voigt line shape function defined above.

The subtraction of the pedestal function from the Voigt shape function removes the line wings from the water line. If the contributions of all real water vapour line wings are summed together, the result is a smoothly varying continuum curve. Since water

vapour lines are broadened by collisions with other water vapour molecules and foreign species, the line wings have both a *self-broadened* contribution and a *foreign-broadened* contribution. The contributions are quantified by two sets of coefficients, the self-coefficients shown in figure 3.6 and the foreign-coefficients shown in figure 3.7. Both the self-coefficients and foreign-coefficients are stored in tabular form in the FASCODE program. The self-coefficients are stored for two temperatures, 260 K and 296 K, and must be corrected to the temperature of the layer using the equation [9]

$$C_s = C_s^{296} \left( \frac{C_s^{260}}{C_s^{296}} \right)^{\frac{T-296}{260-296}} \tag{3.33}$$

where $C_s^{296}$ is the self-coefficient for 296 K, $C_s^{260}$ is the self-coefficient for 260 K, and $T$ is the equivalent temperature of the layer. The foreign-coefficients are not affected by temperature and need no correction.

The opacity due to the water vapour continuum is given by [26]

$$k_{cont} = \sigma \tanh \left( \beta \frac{100 \times \sigma}{2} \right) \left[ C_s \left( \frac{e}{p_0} \right) + C_f \left( \frac{p-e}{p_0} \right) \right] \tag{3.34}$$

where $\beta = \frac{hc}{k_B T}$, $e$ is the partial pressure of water vapour in Pa, $p$ is the pressure of the atmosphere in Pa, and $p_0$ is the base pressure of $1.013 \times 10^5$ Pa.

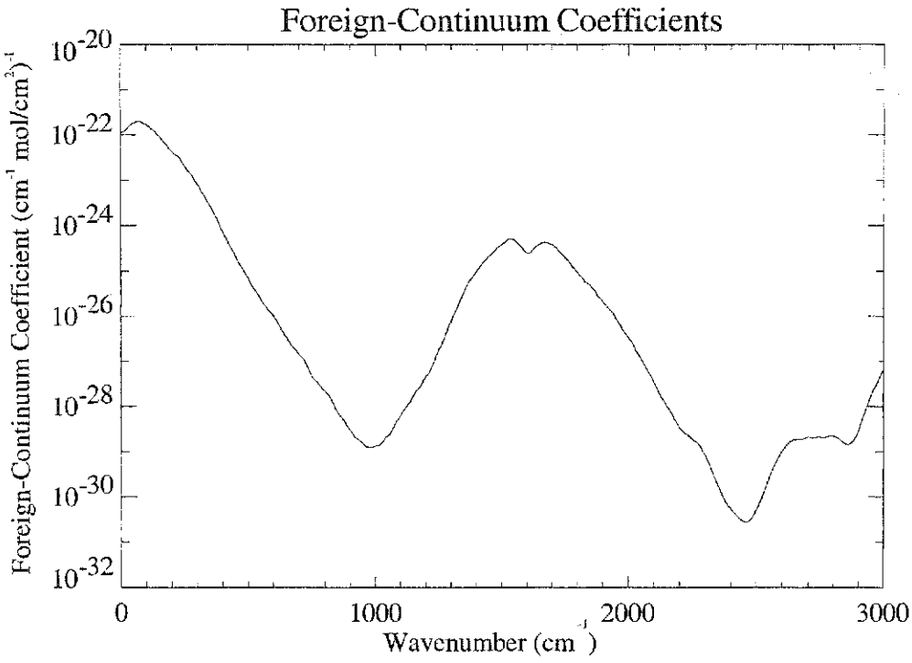


Figure 3.7: A plot of the CKD foreign-continuum coefficients.

## 3.5 University of Lethbridge Transmittance and Radiance Atmospheric Model

### 3.5.1 Model Description

The University of Lethbridge Transmittance and Radiance Atmospheric Model, or ULTRAM, was written in Interactive Data Language 5.4 (IDL 5.4®) [10]. IDL® was chosen as the development language because of its powerful array processing capabilities.

Most radiative transfer models, such as FASCODE and ULTRAM, are known as

*line-by-line, layer-by-layer* radiative transfer models because of the method used. The term 'line-by-line' refers to the fact that the contribution to opacity at a specific wavelength by each spectral line must be calculated separately. These contributions can then be summed together using equation 2.29 to give the overall opacity. The 'layer-by-layer' term refers to the fact that the model approximates the atmosphere as a series of layers, extending from space to ground. The spectral conditions are calculated for each layer in sequence from space to the ground, tracking the absorption and emission of radiation through the layers.

The IDL® array routines are well suited to efficient line-by-line calculations. Most computer languages need to loop through each line to calculate its contribution to opacity at the given wavenumber. This would take a large amount of time since there are thousands of spectral lines contributing to the opacity. IDL® can handle the line-by-line calculation using large arrays of line parameters instead of looping through each line individually. This advantage is due to the specially developed array processing routines that set IDL® apart from other computer languages.

The main goal in the development of ULTRAM was to provide the user with the flexibility to model radiative transfer under local conditions. The compactness of the IDL® code allows users to customize ULTRAM for their own specific purposes while saving them from unpredictable consequences in other parts of the code, as was a danger with FASCODE.

ULTRAM is a user-friendly and flexible program. Users can generate their own model atmospheres using the MAKE_ATMOSPHERE program, select either the radiance or the transmittance of the atmosphere, uses the CKD continuum coefficients from version

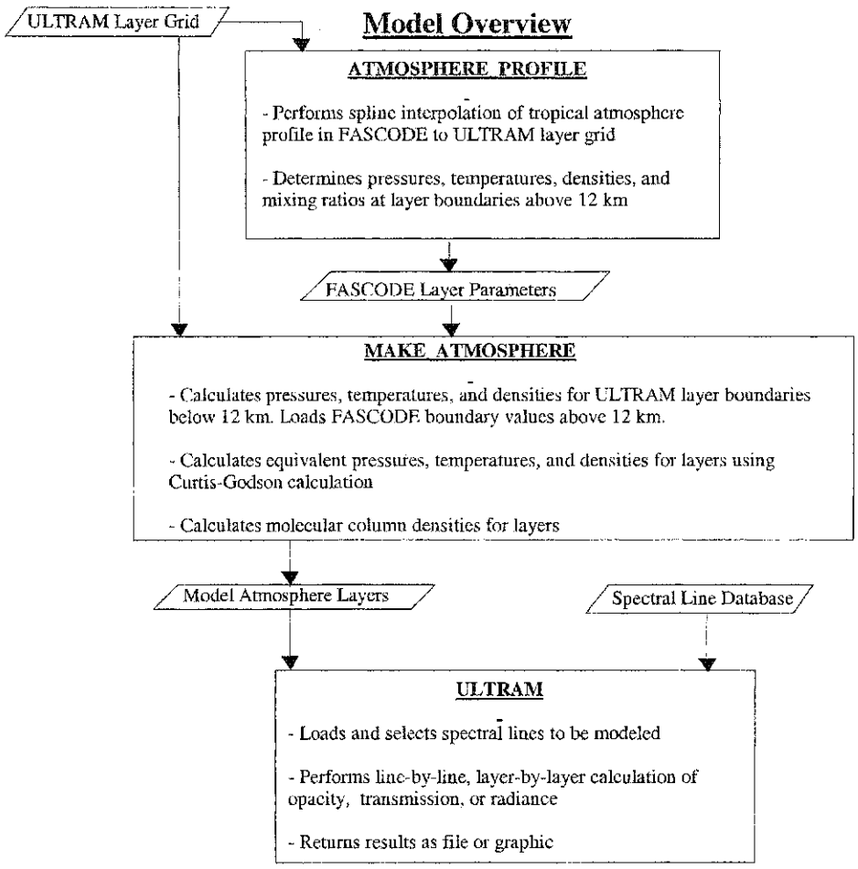


Figure 3.8: Flowchart outlining the general operation of ULTRAM.

3 of the FASCODE program [25] water vapour continuum, or choose not to include the continuum component. Further customizing of features is easily accomplished.

### 3.5.2 Model Algorithm

One of the important inputs to the ULTRAM program are the atmospheric layer boundaries. The default layer boundaries for ULTRAM were defined by iteratively de-

| Layer Altitude | Layer Thickness | Number of Layers |
|---|---|---|
| 4092 - 4500 m | 408 m | 1 |
| 4500 - 12000 m | 500 m | 15 |
| 12 - 30 km | 2 km | 9 |
| 30 - 50 km | 4 km | 5 |

Table 3.1: Default ULTRAM layer thicknesses.

creasing the layer thickness from 5 km to 100 m through the entire atmosphere and making comparisons to determine the difference in the spectra produced. The desire for efficiency in the model required that the number of layers be few enough to produce a spectrum in a reasonable time frame ($\sim$20 minutes) but be thin enough to allow for an accurate spectrum to be produced. It was found that in the lower atmosphere (4092 m to 12000 m), where water vapour is present with a scale height of $\sim$2 km, that layers of 500 m thickness were the optimum size to balance accuracy with efficiency. In the stratosphere, from 12 km to 30 km, layers of 2 km thickness provided the best balance. From 30 to 50 km, layers of 4 km thickness were used. This layering scheme, shown in table 3.1, is the default; however, the user can input whatever layering scheme he or she chooses.

The flowchart in figure 3.8 gives a general outline of the model algorithm. The first step in the modelling program is to perform a spline interpolation of the FASCODE atmospheric parameters to the same layering grid as used by ULTRAM. These parameters will be used to describe the atmosphere above 12 km altitude since the modelling of this region is beyond the scope of this thesis. Next, ULTRAM creates a model atmosphere by calculating pressures, densities, and temperatures for layers below 12 km from the equations in § 3.3 and combining them with the parameters for layers above 12 km from FASCODE. Finally, the model atmosphere file is passed to the main radiative transfer model program

which loads the spectral lines to be used and performs the radiative transfer simulation. Each of these processes is described in more detail in the following paragraphs.

The first step in the modelling process is to create a profile of the various atmospheric parameters ($P$, $T$, $n$, $n_g$, etc.). A program, ATMOSPHERE_PROFILE, was created to perform a natural cubic spline interpolation of the FASCODE tropical atmosphere profile. This interpolates the profile to either the default layer boundaries or boundaries specified by the user. These quantities are stored in a file for use with the MAKE_ATMOSPHERE program. The program accepts a base pressure and temperature and then calculates the pressures at the layer boundaries using equation 3.5 and the boundary temperatures using equation 3.18. Above an altitude of 12 km, the ozone layer begins to affect the temperature and pressure of the layers. At this point the program uses the splined values from the FASCODE tropical atmosphere profile. The MAKE_ATMOSPHERE program performs the Curtis Godson approximation from equation 3.8 to find equivalent pressures for the layers. Using equation 3.7, the average molecular densities for the layers are calculated. Average mixing ratios from the FASCODE profile are used with equation 3.22 to find the layer column abundances for each molecular species. The temperature at the layer boundaries below 12 km is found using equation 3.18 and the mean layer equivalent temperatures are found using equation 3.19. The equivalent values for pressure, temperature, densities, and column abundances are stored in a file for inspection and for use by ULTRAM.

After the model atmosphere has been defined, the main radiative transfer modelling routine begins. The main model program, called ULTRAM, begins by loading in the atmosphere files produced by MAKE_ATMOSPHERE. It also loads the spectral line data

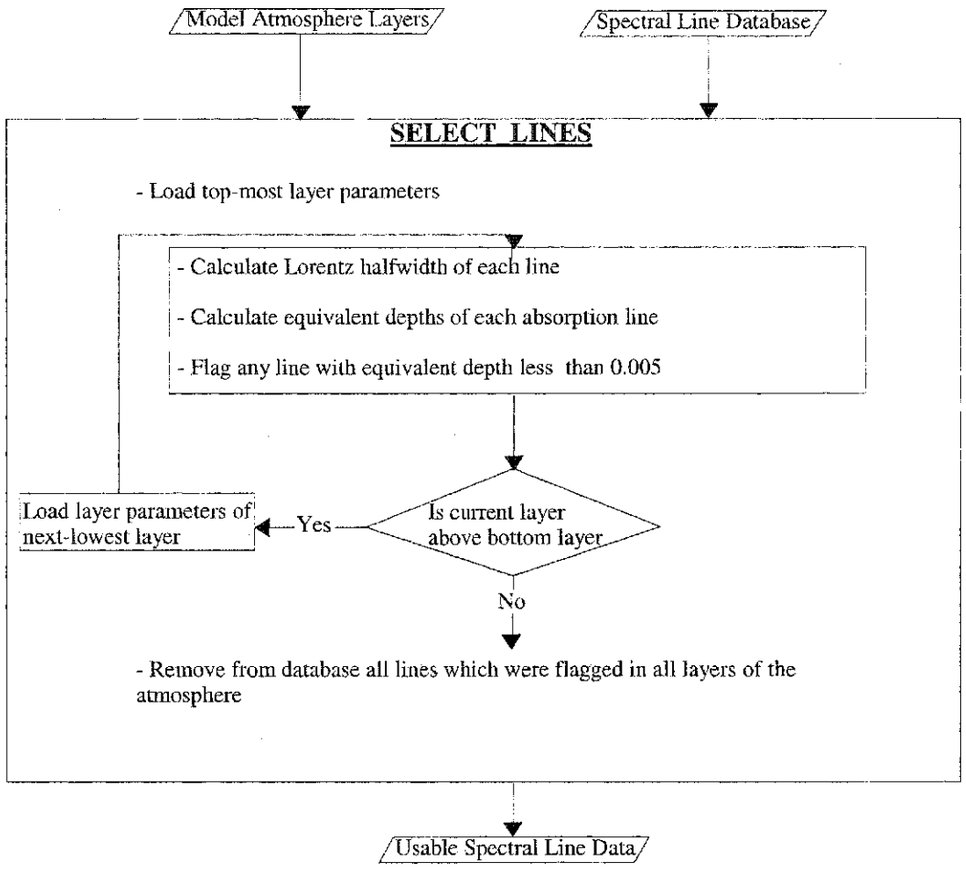


Figure 3.9: Flowchart of the SELECT_LINES function, which selects spectral lines of high enough intensity to include in the radiative transfer calculation.

from a file produced earlier from the Hitran database [16]. Using the function MOLECULAR_LINES, all relevant line data is loaded into a variable for use with the model. This line data is used by the function SELECT_LINES which selects only lines above a certain intensity threshold to optimize the radiative transfer computation.

The function SELECT_LINES, shown in the flowchart in figure 3.9, makes use

of the weak approximation of the *integrated absorptance* (equation 2.41) of an absorption line to determine if it should be included in the modelling run, increasing the efficiency of ULTRAM by removing lines too weak to be seen. Starting with the top layer of the atmosphere, the layer parameters are loaded in to the function. The function calculates the Lorentz half-width of each spectral line using equation 2.35 and uses this to calculate the equivalent depth of the absorption line using the weak approximation from equation 2.41. An arbitrary depth limit is set at 0.005. Any spectral lines with depths less than 0.005 (equivalent to 0.5% absorption) for the layer are flagged. This process is repeated for each layer, moving downwards to ground level, and any spectral lines which were flagged for all of the layers are removed from the spectral line database. This reduced line database is passed back to the main program for use in the radiative transfer calculations.

The main program begins the radiative transfer modelling by passing the spectral line data, atmospheric profile, and molecular abundance data to the LAYERS function, shown in the flowchart in figure 3.10. This function calculates either the transmittance or radiance at the given wavenumber using the radiative transfer method. LAYERS is the *engine* of the program that does the line-by-line, layer-by-layer calculations. The function begins by selecting the spectral lines whose line centers are within 25 $cm^{-1}$ of the current wavenumber since lines outside this range have negligible contributions to the absorption coefficient, $k_\sigma$. In the case of ozone lines with their much narrower Doppler profile, only spectral lines within 1 $cm^{-1}$ of the current wavenumber are accepted, further increasing the efficiency of the computation.

After the lines relevant to the calculation have been selected, the function loads

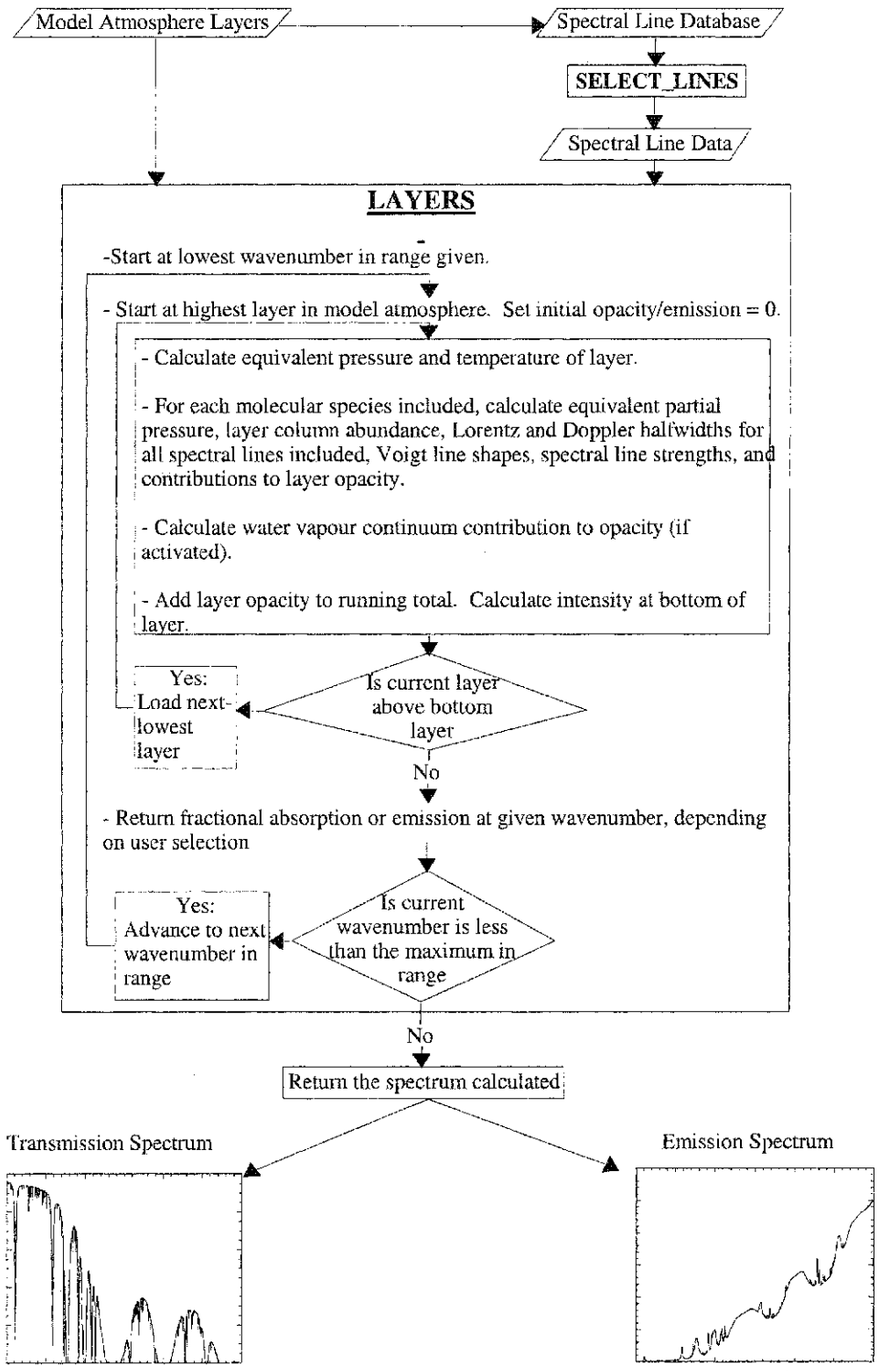


Figure 3.10: Flowchart of the LAYERS function, the main engine of ULTRAM.

the parameters for the top layer of the atmosphere. The function calculates the partial pressure of each species using equation 3.26. Next, the Doppler widths and Lorentz half-widths of all the lines are calculated using equations 2.33 and 2.35 respectively. Then, the values of the line shapes at the given wavenumber are calculated using the Voigt line shape function which is based on equation 3.27. The water vapour spectral line shapes are modified by subtracting the pedestal function given in equations 3.31 and 3.32. The spectral line strength values at the given wavenumber are calculated using equation 2.38. Finally, the contribution of each line to an overall opacity is calculated using equation ?? with equations 3.23 and 2.27. After the opacity contributions of all spectral lines have been calculated, they are summed to give an overall opacity at the current wavenumber due to spectral lines for the layer.

The next step is to calculate the contribution of the water vapour continuum if it is to be included. First, the partial pressure of water vapour and of the remainder of the atmosphere are calculated. Next, the self-continuum coefficient is corrected for the layer temperature. The total opacity contribution of the water vapour continuum for the layer is then calculated using equation 3.34.

The total opacity of the line is then calculated as the sum of the line opacity and the continuum opacity. The opacity for the layer is then added to a running total of the opacity. If the model is set to return radiance, this total opacity is used in equation 2.22 to calculate the intensity of radiation exiting the bottom of the layer. The radiance at the top of the atmosphere is taken to be zero. The algorithm repeats the process for each layer of the atmosphere, moving down one layer at a time.

If the model is set to return radiance, the LAYERS function calculates the intensity exiting from the bottom layer of the atmosphere. If the model is set to give transmittance, the LAYERS function returns the total opacity at the bottom of the atmosphere. The LAYERS function returns to the main program the radiance or transmittance for each sample point in the spectrum. At this stage it is customary to convolve the spectrum with the instrument line shape (ILS) function of a spectrometer, simulating an actual measurement. This allows the user to produce a spectrum that one would expect to observe with a specific spectrometer. In the present case, the spectrum was convolved with a Gaussian ILS having a full-width at half-max of 0.005 $cm^{-1}$. Other common ILS' such as triangle, sinc, or sinc-squared are also available.

### 3.5.3 ULTRAM Results

As was mentioned in § 3.3.3, this thesis is concerned with two main spectral regions: the SCUBA submillimeter range from 5 $cm^{-1}$ to 35 $cm^{-1}$ and the IRMA mid-infrared range from 475 $cm^{-1}$ to 575 $cm^{-1}$. Each of these spectral regions must be modelled accurately in order to obtain a clear understanding of the correlations between water vapour measurements with IRMA and SCUBA. Table 3.2 highlights several parameters involved in modelling each spectral region.

It was considered important as a first step to ensure that ULTRAM gave the same results as FASCODE under the same conditions. Both ULTRAM and FASCODE allow the user to select the output to be returned in terms of transmittance (between 0 and 1)

| | Submillimeter | MIR |
|---|---|---|
| Range ($cm^{-1}$) | 5 – 35 | 475 – 575 |
| Resolution ($cm^{-1}$) | 0.001 | 0.001 |
| Layers | 31 | 31 |
| $H_2O$ Lines | 299 | 551 |
| $O_3$ Lines | 2237 | 120 |
| $O_2$ Lines | 243 | 0 |
| $CO_2$ Lines | 0 | 2107 |
| Total Lines | 2779 | 2778 |
| Time (s) | 738 | 1790 |

Table 3.2: Radiative transfer modelling parameters for the submillimeter and mid-infrared regions.

or in terms of radiance (W $m^{-2}$ $sr^{-1}$ $cm^{-1}$). Astronomers are usually interested in transmittance data because it reveals wavelength ranges which are 'windows' for observations of astronomical objects. Radiance data are more appropriate for applications which involve remotely sensing molecular abundances in the atmosphere. Each of these output selections (transmission or radiance) can be returned by ULTRAM as either a spectrum for a given precipitable water vapour amount or as a three-dimensional data cube with varying precipitable water vapour amounts.

One difference between the models is that FASCODE used the 1986 version of the Hitran molecular line database [27] while ULTRAM used the 2000 version of the Hitran database [18]. This latest version of the Hitran database has updated values for spectral line strengths and half-widths. In particular, one of the improvements is the inclusion of self broadening values. A comparison of spectra obtained using the two databases with the same atmospheric layers will show some subtle differences due to updates in the spectral line parameters.

For the comparison with FASCODE, 1 mm pwv was chosen as the standard column

abundance of water vapour. Since FASCODE is not easily changed, ULTRAM used the same atmospheric layers as those produced by running the FASCODE auto-layering routine. Both models were run with identical layer parameters (i.e. pressures, temperatures, molecular densities, layer boundaries).

Figure 3.11 shows the submillimeter transmission spectra as produced by FASCODE (black) and ULTRAM (red). The ULTRAM spectrum is displaced vertically for clarity. The top panel in the figure shows the entire submillimeter range. Two submillimeter windows can be seen: one from 20 $cm^{-1}$ to 24 $cm^{-1}$ (known as the 450 $\mu$m window) and another from 26 $cm^{-1}$ to 30 $cm^{-1}$ (known as the 350 $\mu$m window). The middle panel shows an expanded view of the 450 $\mu$m window. A strong water vapour line can be seen centered on 20.7 $cm^{-1}$ and an oxygen line can be seen at about 23.85 $cm^{-1}$. The shallow, narrow spectral lines across the top of each spectrum are a manifold of ozone lines. The bottom panel shows a further expansion of the complex manifold of spectral lines. Spectral lines of water vapour, ozone, and oxygen are present in this region. The spectra are seen to be in excellent agreement.

The mid-infrared transmission spectrum is shown in figure 3.12. Again, the ULTRAM spectrum (red) is shifted vertically from the FASCODE spectrum (black) for clarity. The top panel shows the IRMA range from 500 $cm^{-1}$ to 550 $cm^{-1}$. This spectral range includes numerous water vapour lines and carbon dioxide lines. The middle panel is an expanded view of one of the windows in this region. It shows several water vapour lines (such as the one at about 534.25 $cm^{-1}$). A close inspection of this panel shows subtle differences in the lines produced by FASCODE and ULTRAM. For example, the water vapour line at

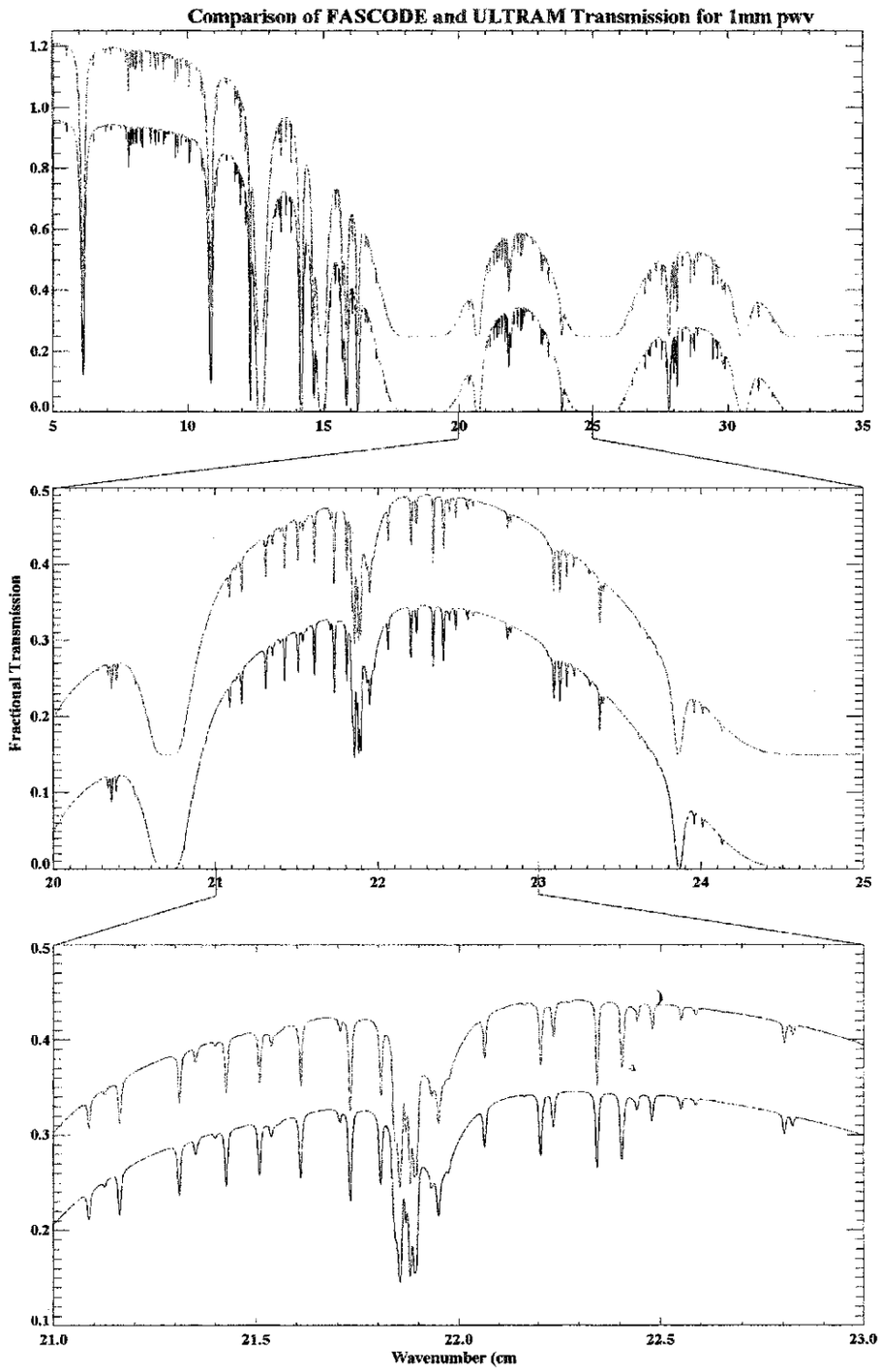


Figure 3.11: Comparison of simulated (sub)millimeter transmission spectra for 1 mm pwv from ULTRAM (red) and FASCODE (black).

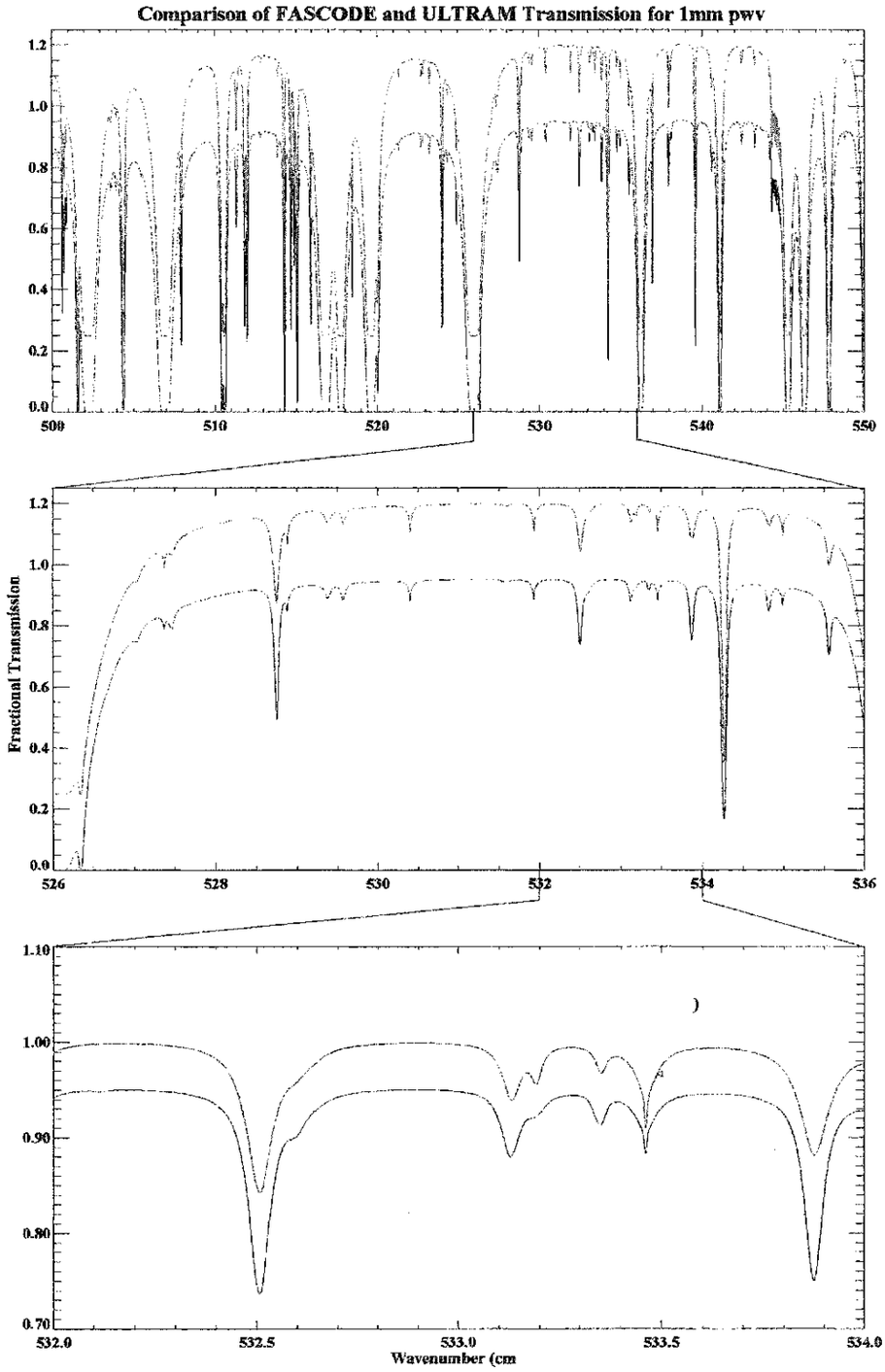


Figure 3.12: Comparison of simulated mid-infrared transmission spectra for 1 mm pwv from ULTRAM (red) and FASCODE (black).

about 528.75 $cm^{-1}$ appears weaker in the ULTRAM output than in the FASCODE output. This is due to an adjustment of the line parameters in the updated Hitran spectral line database. The bottom panel of the figure shows a further expansion of a portion of the window. Again, the spectral lines in the ULTRAM output are subtly different from the FASCODE output due to updates in the line parameters in the newer database. Despite the changes in the spectral line database, ULTRAM shows a high level of agreement with FASCODE in this spectral region.

Figure 3.13 compares the submillimeter emission spectra from ULTRAM and FASCODE. The ULTRAM spectrum (red) is again vertically displaced above the FASCODE spectrum (black) for clarity. The top panel of the figure shows the entire submillimeter region and is populated with spectral lines of water vapour, oxygen, and ozone. The middle panel shows an expanded view of the 450 $\mu$m window with a strong water vapour line at about 21.7 $cm^{-1}$, an oxygen line at about 23.85 $cm^{-1}$, and a manifold of weak ozone lines between them. The bottom panel is a further expanded view of this window, focusing on the complex region between 21.8 $cm^{-1}$ and 22.1 $cm^{-1}$. The models show a high level of agreement in this spectral region.

Figure 3.14 shows the comparison of mid-infrared emission spectra. Good agreement between the models is seen and differences in the line parameters are evident in this figure. An important difference between the spectra in these two regions is in the baseline slopes of the spectra. The slope in the submillimeter region is due to the slope of the Rayleigh-Jeans tail of the Planck function. The mid-infrared region has a smaller slope because the Planck function is near its peak at these wavenumbers.

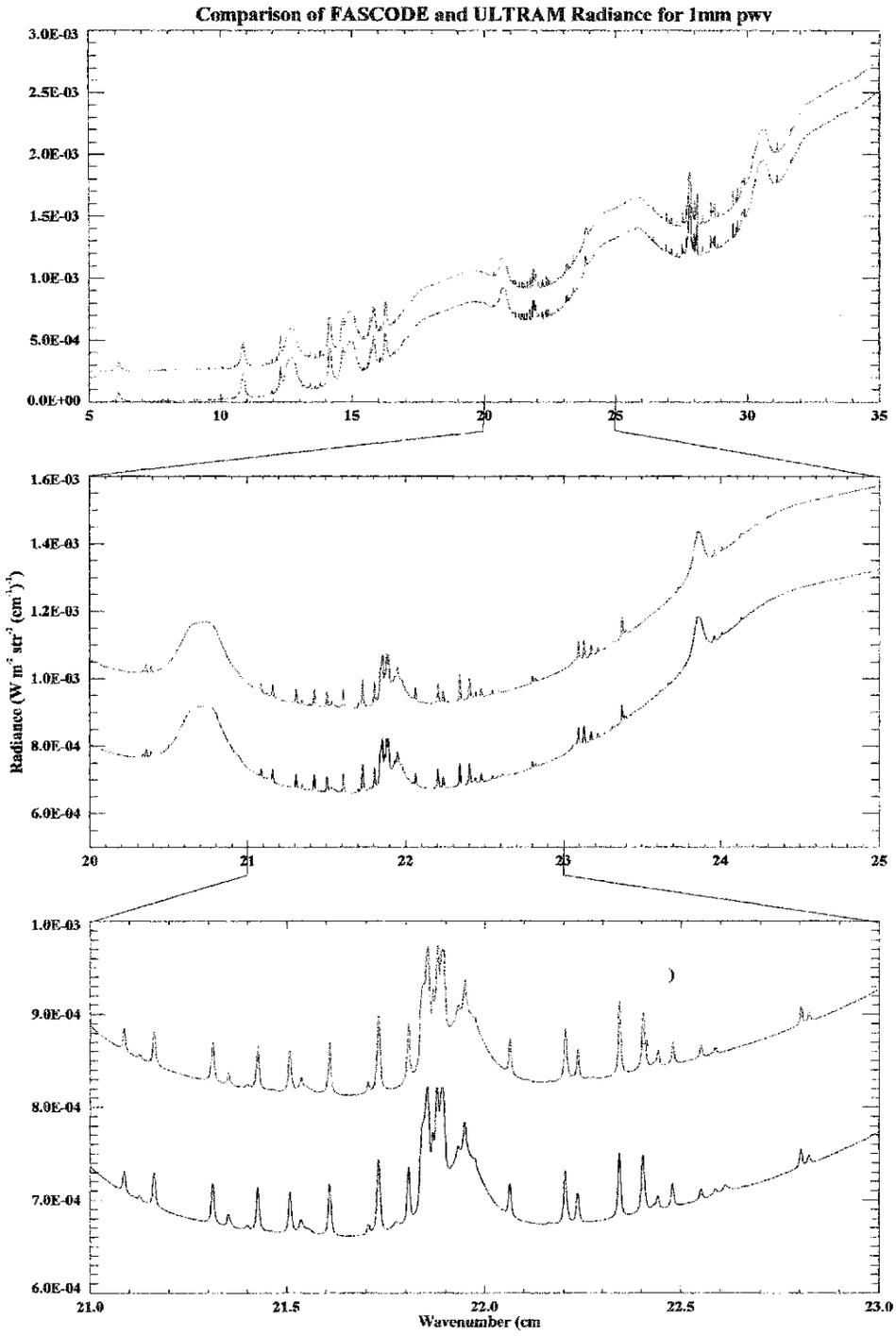


Figure 3.13: Comparison of simulated (sub)millimeter radiance spectra for 1 mm pwv from ULTRAM (red) and FASCODE (black).

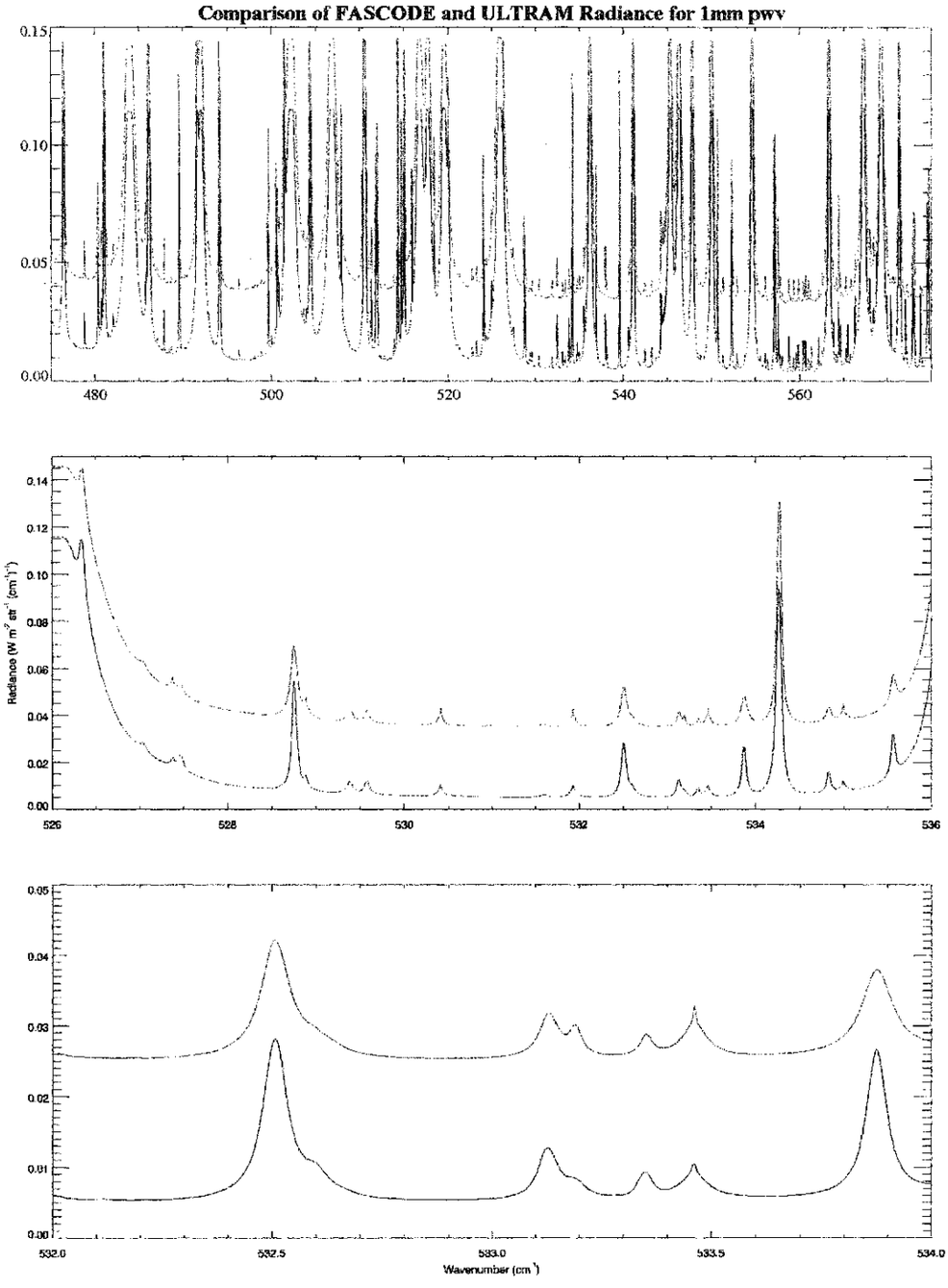


Figure 3.14: A comparison of the simulated mid-infrared radiance spectra produced by ULTRAM (red) and FASCODE (black).

Since ULTRAM has been shown capable of replicating the FASCODE output, it can be used to model spectra at submillimeter and mid-infrared wavelengths. Using ULTRAM, it is possible to investigate the effects of changing the pressure, temperature, and molecular abundance profiles of the atmosphere. To construct a data cube, ULTRAM is run several times, increasing the precipitable water vapour amount by 0.1 mm each time. The resulting data set, covering a range of 0.1 - 2.0 mm pwv, can be plotted in 3 dimensions (wavenumber, transmission or emission, mm pwv), to show the evolution of the spectra with changing water vapour amounts. The data cube forms a comprehensive database which can be used to study radiometer bands under different atmospheric conditions.

ULTRAM has been shown to accurately reproduce results from FASCODE calculations. Because of its flexibility, ULTRAM can be used to investigate theoretically the correlation between measurements of the radiance of water vapour at submillimeter and mid-infrared wavelengths. This investigation provides an independent theoretical basis for a comparison with the results obtained with IRMA II and SCUBA on Mauna Kea as presented in chapter 5.

# Chapter 4

# IRMA II Hardware

## 4.1 Overview

This chapter reviews the design and construction of the IRMA radiometer by a previous graduate student, Mr. Graeme Smith, and describes the upgrades made to the radiometer, which resulted in a second generation instrument, IRMA II. Section 4.2: System Overview discusses the main components of IRMA I. Section 4.3: Upgrades discusses the upgrades of the various components, made after the preliminary test of IRMA I in 1999.

## 4.2 System Overview

Figure 4.1 shows an overview of IRMA. The radiometer consists of three main components: an instrumental platform, the electronic instrumentation, and a laptop control computer.

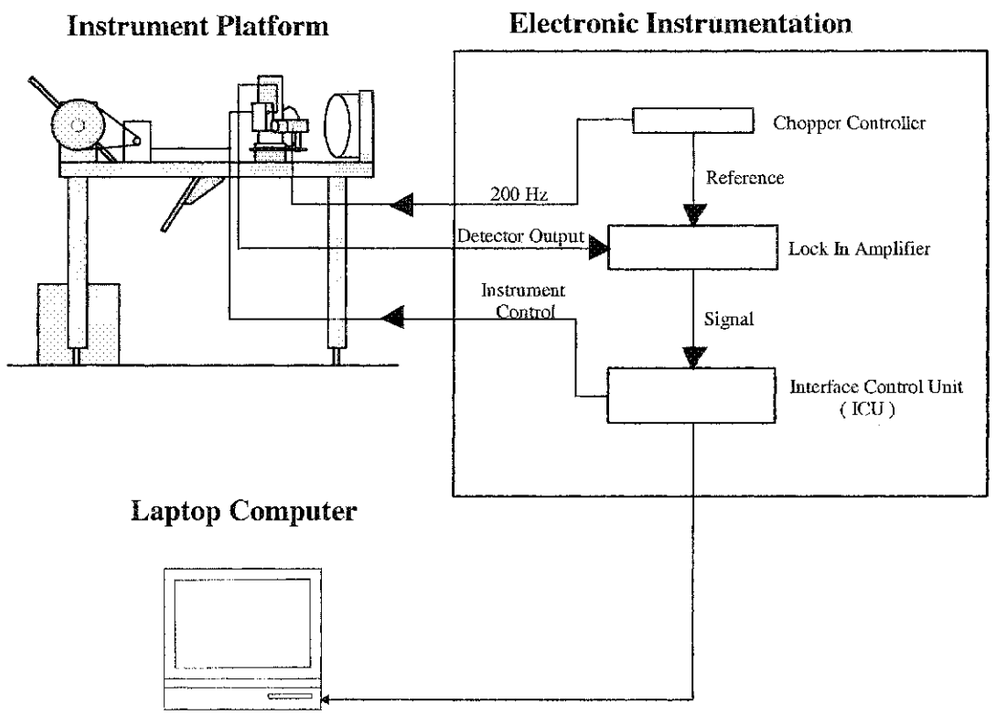


Figure 4.1: A schematic of the radiometer system [2].

The instrument platform, shown in figure 4.2, contains all of the optical components in the system including 2 blackbody calibration sources (ambient and liquid nitrogen ($LN_2$) cooled), an $LN_2$ cooled infrared detector dewar assembly with detector preamplifier and reflective optical chopper, a flat scanning mirror, and an off-axis paraboloid mirror.

The electronic instrumentation consists of a chopper wheel driver unit, a lock-in amplifier, and an interface control unit (ICU) which houses the power supplies, an A/D converter for the signal output from the lock-in amplifier, and a parallel port computer interface. A laptop computer runs the main control software for the radiometer, and performs several functions including driving the scanning mirror and logging data.

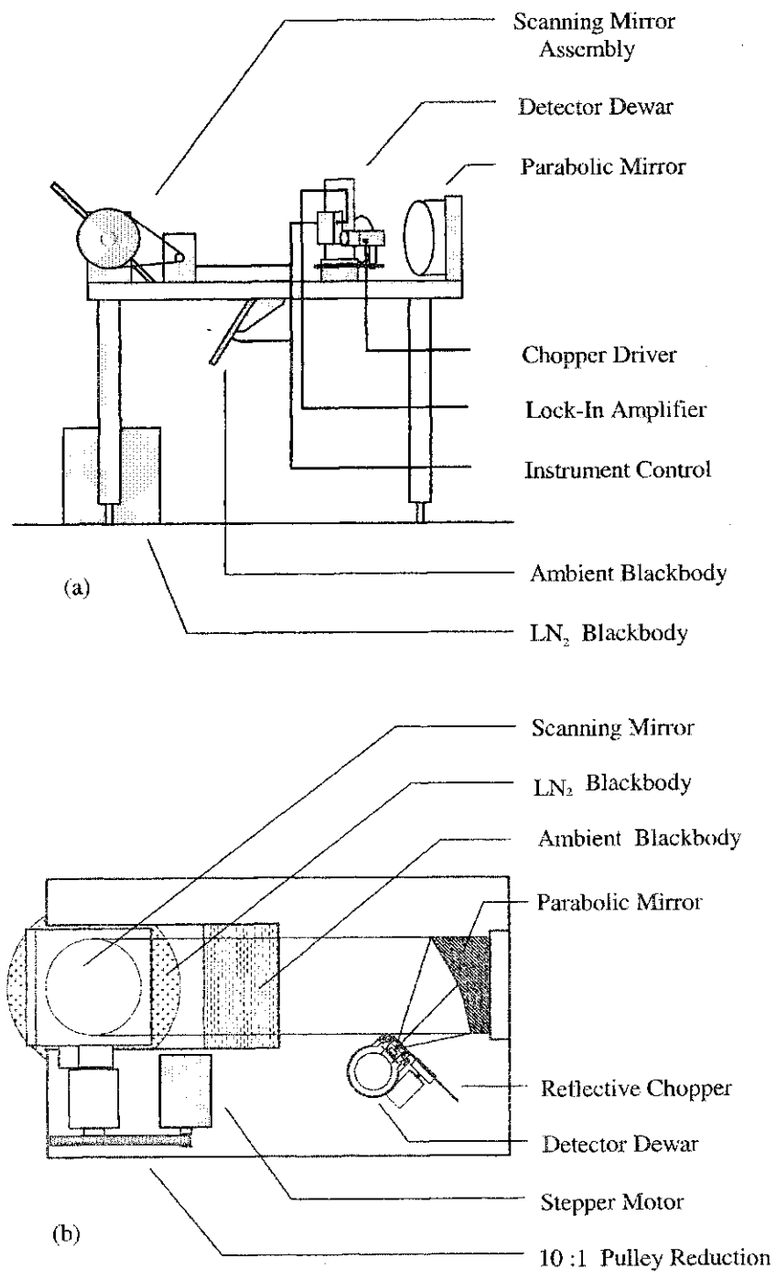


Figure 4.2: (a) A side view of the prototype radiometer instrument platform. (b) A top view of the prototype radiometer instrument platform [2].

### 4.2.1 Instrument Platform Blackbody Calibration Sources

As part of its normal operation, the radiometer periodically views two calibration sources. The cold blackbody consisted of a disc of *Eccosorb*$^{TM}$ [28] submerged in an open flask of $LN_2$ placed on the floor directly below the scanning mirror assembly. At the reduced pressure on the summit of Mauna Kea, the temperature of the cold blackbody was 73 K, the boiling point of $LN_2$ at an atmospheric pressure of 625 mbar.

The second blackbody was allowed to fluctuate with the temperature of the air at the summit of Mauna Kea. This blackbody consisted of an aluminum plate coated with a thermally conductive epoxy (*Epo-Tek 920*) [29] matrix of 2% by weight carbon black. The emissivity of this material in the 500 $cm^{-1}$ spectral region has been measured to be greater than 0.99 [30]. The plate was mounted to the underside of the platform with insulated support brackets. The temperature of the plate was measured using a temperature diode.

### 4.2.2 Parabolic Primary Mirror

An off-axis parabolic mirror, shown in the design schematic in figure 4.3, was chosen as the primary focusing optic in order to maximize the optical energy collected by avoiding occulation of the secondary mirror assembly. This also had the benefit of allowing for a simple and compact radiometer design.

The radiometer was designed to sample a 10 m patch of sky at a range of 1 km, to reflect the typical size of a radio antenna at the approximate scale height of water vapour. Given this field of view (FOV) and the standard detector size of 1 $mm^2$, the diameter of

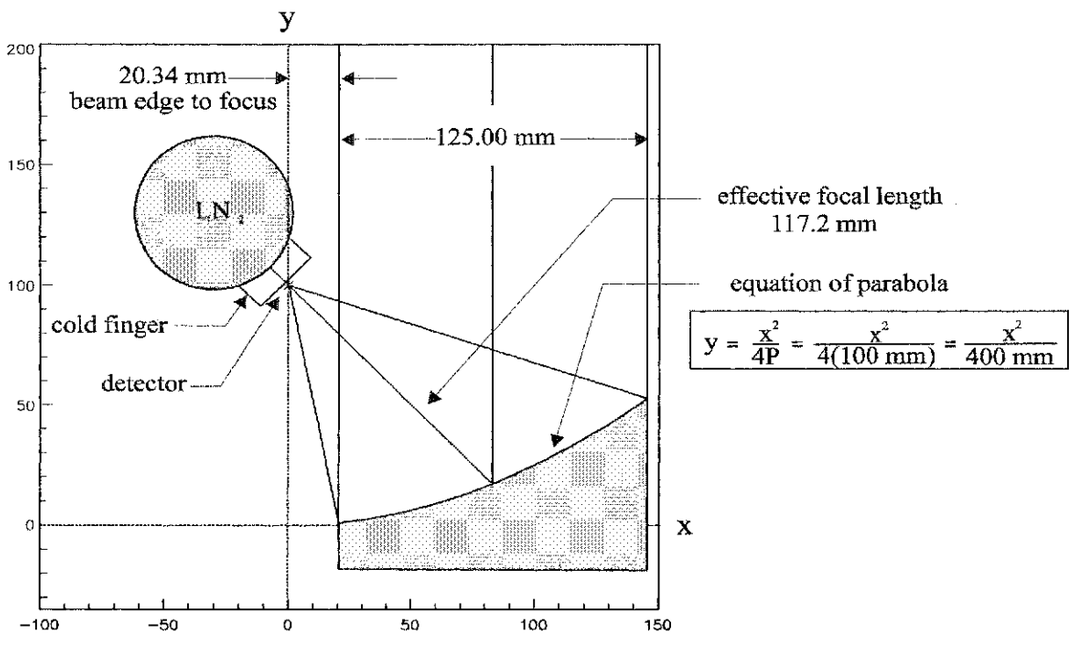


Figure 4.3: A design schematic of the parabolic primary mirror [2].

the paraboloid was chosen to be 125 mm. A summary of the design parameters of the paraboloid is given in table 4.1.

### 4.2.3 Scanning Mirror

The scanning mirror assembly was designed to scan through a zenith angle range of 0° to 70.38° corresponding to an airmass range of 1 to 3. The mirror was actuated via a 200 step/revolution stepping motor (400 step/revolution in half stepping mode) with a 10:1 pulley reduction arrangement. The steps of the motor were tracked by the control

| Design Parameter | Value |
|---|---|
| Diameter | 125 mm |
| Focal Length | 117.5 mm |
| F-Number | 0.937 |
| Focal Point Offset From Beam Edge | 20.34 mm |

Table 4.1: Parabolic mirror design parameters.

| Detector Parameter | Value |
|---|---|
| Active Area | 1 $mm^2$ |
| Responsivity | 45.33 V/W |
| Cut Off Wavelength | 22.15 $\mu$m |
| Resistance @ 77 K | 32 $\Omega$ |
| Nominal Bias Voltage | 0.45 V |
| D* (@ 10 kHz) | $2.88\times10^9$ cm$\sqrt{\text{Hz}}\text{W}^{-1}$ |

Table 4.2: Infrared detector parameters.

computer to provide positional information.

### 4.2.4 Infrared Detector

The infrared detector was a mercury-cadmium-telluride (MCT) device, supplied by *Kolmar Technologies Inc.* [31], designed to operate at 77 K. The detector specifications are shown in table 4.2.

### 4.2.5 Optical Filter

A band-defining CdTe interference filter was purchased from the University of Reading; the spectral response of the filter is shown in figure 4.4. In practice, this response should be modified to take into account a wavelength shift that occurs for radiation incident

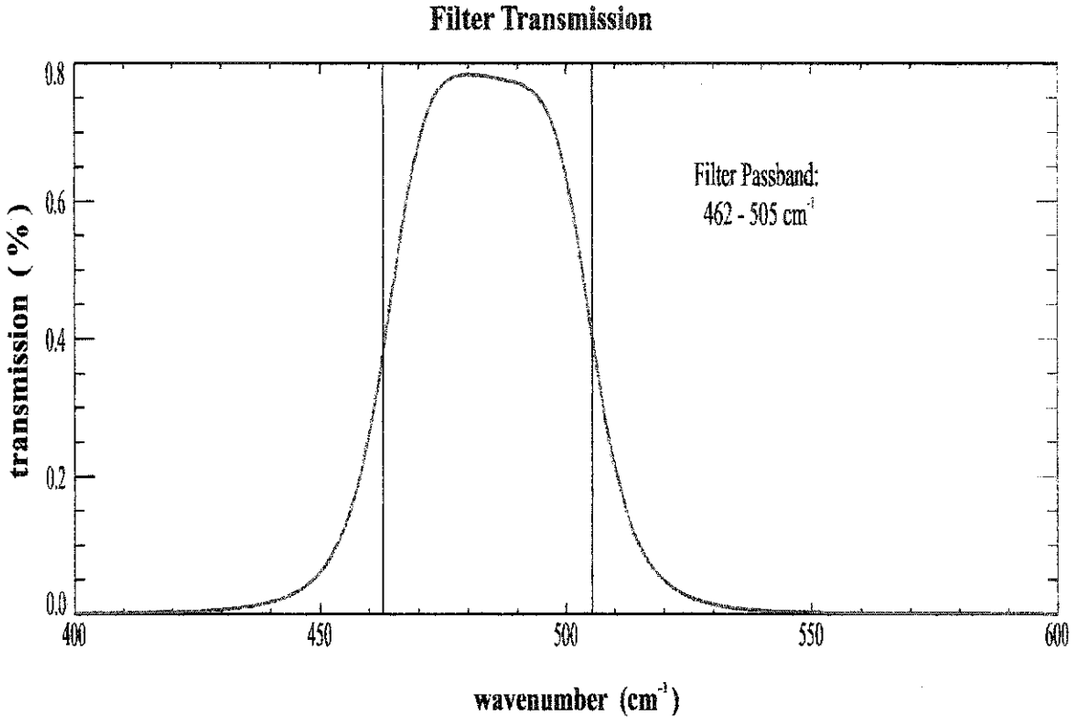


Figure 4.4: A plot of the infrared filter response.

at an arbitrary angle. Without detailed knowledge of the optical properties of the filter to perform the above calculation, the normally incident bandpass response of 462 to 505 $cm^{-1}$ was assumed.

### 4.2.6 Chopping Blade and Dewar Assembly

The optical chopping blade was fabricated from mirror grade stainless steel by the process of *spark erosion machining*. This process eliminates any stress induced flaws and, combined with the mirror-like finish of the steel, produces a blade with a high quality optical

surface. The reflective side of the chopper blade provided the detector, mounted to the cold finger of the dewar and sealed behind a thin polypropylene sheet, with an alternating view of radiation from the paraboloid and an unfocused view of itself (i.e. a 73 K environment). The chopper was machined to have 5 slots, and thus the blade, which rotated at 40 Hz, produced a 200 Hz modulation of the optical beam.

## 4.3 Upgrades

The results from IRMA I showed that the radiometer was capable of resolving at least $\pm$ 3 $\mu$m pwv (1 $\sigma$ in a 1 s integration) [2], equivalent to about $\pm$ 20 $\mu$m of electromagnetic path length. However, a detailed noise analysis suggested that the resolution was closer to 1.6 $\mu$m pwv, which is equivalent to $\pm$ 11 $\mu$m of excess electromagnetic path length. While these results were very close to meeting the challenging requirements for the phase correction of ALMA, several upgrades were subsequently made to the system. These upgrades, which resulted in IRMA II, are discussed below.

### 4.3.1 Improved Detector

A new MCT detector was obtained from Kolmar Technologies Inc. The new detector was similar to the previous one, but had a higher detectivity and responsivity, $5.11\times10^9$ cm $Hz^{-1/2}$ $W^{-1}$ and 136 V $W^{-1}$ respectively, compared with $2.88\times10^9$ cm $Hz^{-1/2}$ $W^{-1}$ and 45 V $W^{-1}$ for the earlier detector.

As a result of the improved detector specification, the expected signal-to-noise

improvement over the original detector was [2]

$$\frac{(S/N)_{New}}{(S/N)_{Old}} = 1.77 \tag{4.1}$$

### 4.3.2 Improved Infrared Filter

Infrared filters are very difficult to fabricate for use at 500 $cm^{-1}$. The filter used in IRMA I was not an optimal match to the spectral region of interest, but was the only one available at the time. Professor Peter Ade of Cardiff University, Wales, recently extended his filter fabrication technology from ~50 $cm^{-1}$ to ~500 $cm^{-1}$. During this development work, Dr. Ade provided two filters using resonant capacitive and inductive micro-elements that provided a better match to the detector and the spectral range of interest. The higher efficiency and better band selection of these filters were expected to make a factor of two improvement in detection efficiency over IRMA I. The filter+detector response, as measured by a *Bomem* Fourier transform spectrometer (Model MB102), is shown in figure 4.5.

### 4.3.3 Improved Electronics

A significant improvement in the electronics was effected by replacing the 12 bit analog-to-digital converter (ADC) with a 24 bit, delta-sigma ADC (Cirrus; CS5534), which provided an equivalent resolution of 18 bits when sampling at 0.3 s. This addressed the problem encountered with IRMA I that the dynamic range of the observed signal was

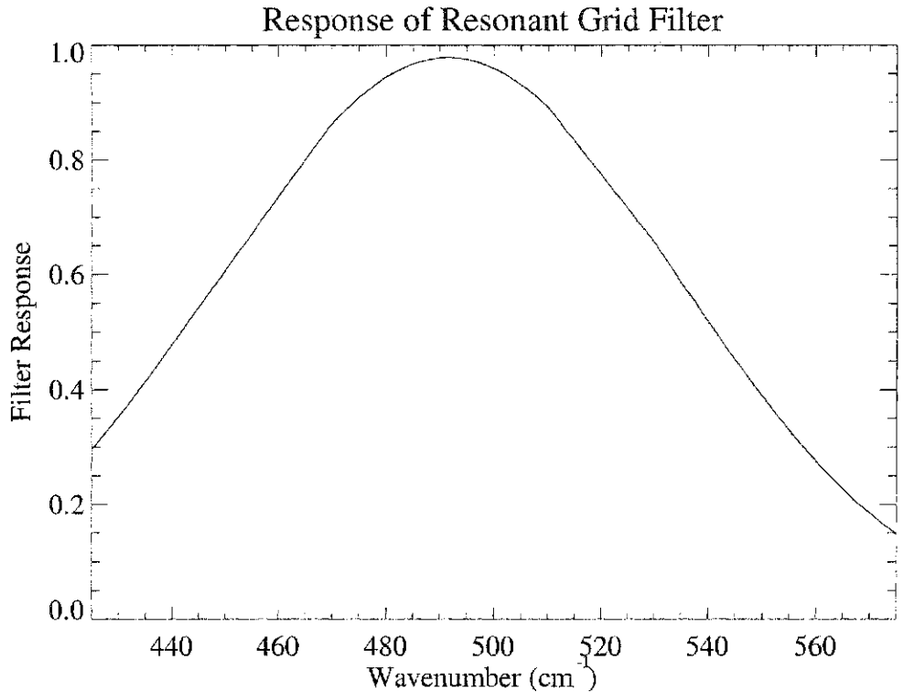


Figure 4.5: Filter response of new infrared filter used by IRMA II.

greater than the dynamic range of the 12 bit ADC. This modification resulted in a seven-fold improvement in signal-to-noise [2].

### 4.3.4 Remote Operation

The most dramatic upgrade to IRMA I was the implementation of web-based control. IRMA II was configured to operate remotely, over the internet, to perform skydips at any time.

The IRMA II skydips are stored on the internet server, compiling a large database

of measurements of atmospheric water vapour abundance above the summit of Mauna Kea. The analysis of these measurements, including a comparison with measurements of atmospheric water vapour by other instruments at the summit of Mauna Kea, follows in Chapter 5.

# Chapter 5

# Results

## 5.1 Overview

This chapter discusses the analysis of data obtained with IRMA II (hereafter referred to as IRMA) on Mauna Kea during its operation in 2001 [32]. Section 5.2: Data Reduction discusses the methods used to reduce the raw data set to contain only those data matching in time with other measures of water vapour above Mauna Kea, as well as the method of removal of poor data from the set. Section 5.3: Calibration shows how the raw data files were calibrated. Section 5.4: Stretch-and-Splice Analysis describes the method used to analyze the data in order to determine water vapour abundance, including the synthesis of a curve-of-growth. Section 5.5: Comparison With Other Measures of Water Vapour compares the IRMA measurements of water vapour above Mauna Kea with other measurements available at the site. Section 5.6: Comparison of Curve-of-Growth With Theory compares the curve-of-growth, synthesized from IRMA skydips, with a curve-of-

growth calculated from ULTRAM.

## 5.2 Data Reduction

Between December, 2000 and March 2001, IRMA performed skydips to measure the atmospheric radiance as a function of zenith angle, or airmass while mounted on the apron of the James Clerk Maxwell Telescope (JCMT) on Mauna Kea, as shown in the photo in figure 5.1. A total of 1893 IRMA skydips were obtained during this time. Although it did not share the same line-of-sight as the telescope, IRMA did point at nearly the same azimuthal angle, sampling the same general area of the sky as the JCMT Submillimetre Common User Bolometer Array (SCUBA) [33]; it was thus expected that the IRMA and SCUBA data would be correlated. However, since it takes SCUBA ~7 minutes to perform a single skydip, during which time IRMA can perform several skydips (typically 4), the comparison of data required matching the times of the independent observations.

The IDL® program FILTER_IRMA was written to select the IRMA skydip data obtained within a 20 minute window of a SCUBA skydip measurement. When this program was executed for all SCUBA skydips obtained during the observing period, the number of matching IRMA skydips was 1226.

The next step was to examine this reduced data set for quality. Several factors affect data quality including: loss of detector cryogen, obstruction of the beam by a foreign object, and high amounts of atmospheric water vapour. The IDL® program WEED_IRMA was written to reject data of such poor quality that it reflected instrumental problems or

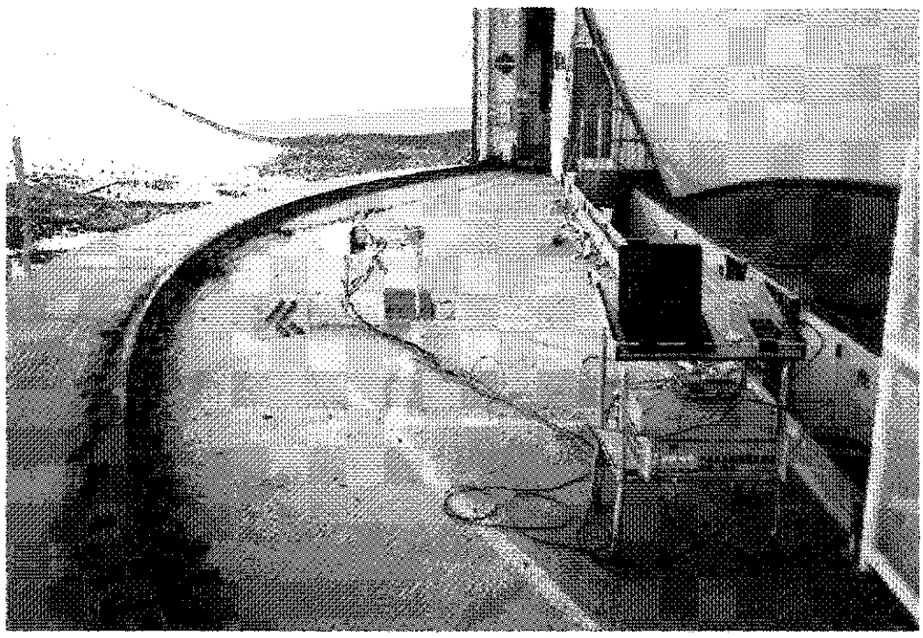

Figure 5.1: A photograph of IRMA on the apron at the JCMT.

extremely poor weather; for example, skydips with maximum voltages less than 0.5 V, which are indicative of the detector losing its cryogen, producing an unrealistically dry measurement, or skydips with minimum voltages greater than 1.5 V which are indicative of extremely wet atmospheric conditions. This program rejected a total of 48 skydips ($\sim$4 % of the time-matched skydips).

The final step in the data selection process was to test the remaining skydips for smoothness by non-linear least squares fitting an exponential curve to the data using the CURVEFIT function from the IDL® library. Departures from smoothness can result from several causes such as thick cloud banks or viewing a nearby cinder cone. The CURVEFIT

function returns a measure of the quality of the fit; through inspection it was found that fit quality measures less than 0.001 produced superior quality fits and this threshold was adopted as the final filtering step. This final step removed 112 skydips (9.1 % of the time-matched skydips). Of the 1226 skydips matched to SCUBA skydips, 1066, or ~87 %, were of high enough quality to be used in the final analysis.

## 5.3 Calibration

As was mentioned in chapter 4, IRMA converts incident spectral radiant power into a detector signal voltage. An *instrumental responsivity*, $R_{inst}$, expressed in $\mathrm{V \cdot W^{-1}}$ relates the instrumental output voltage to the incident spectral power. The relation of the voltage, $V$, to the incident power, $\Phi$, is given by

$$V = \Phi \cdot R_{inst} \qquad \mathrm{V} \tag{5.1}$$

To determine $R_{inst}$, the signal voltage must be measured as a function of incident power. IRMA has a calibration cycle built into its skydip mode, in which it observes a blackbody at ambient temperature and another blackbody submerged in liquid nitrogen. These blackbodies have well-known temperatures, and hence well-known spectral radiances, thus allowing the determination of $R_{inst}$ for each skydip from the calibration cycle.

A time series of calibration measurements made by IRMA shows a general degradation in instrumental responsivity over the months that IRMA was operated. Possible explanations for the degradation include: the loss of vacuum in the detector dewar or dust

build-up on any part of the optical train. In such cases, the instrumental responsivity is effectively reduced and individual skydips must be calibrated to account for this change.

During each skydip, IRMA made five measurements of the radiances and temperatures of its ambient and liquid nitrogen blackbodies. These measurements were averaged and used to calculate the responsivity for the skydip. The incident power, $\Phi$, was calculated using the ambient temperature, $T_{BB}$, of the blackbody and the *throughput*, $\in$, of the system in the equation

$$\Phi = L_{BB}(T_{BB}) \in \qquad \mathrm{W} \tag{5.2}$$

The spectral radiance of the ambient blackbody, $L_\sigma$, is given by the Planck formula

$$L_\sigma(T_{BB}) = \left(2hc^2 100^4 \sigma^3\right)\left(e^{\frac{hc100\sigma}{k_B T_{BB}}} - 1\right)^{-1} \qquad \mathrm{W\ m^{-2}\ sr^{-1}\ (cm^{-1})^{-1}} \tag{5.3}$$

where $T_{BB}$ is the temperature of the blackbody in K. The *radiance* is found by integrating $L_\sigma$ over the spectral range as discussed in § 3.3.3. In practice, the radiance measured also depends on the combined detector-filter spectral response. But to first-order, the passband of the filter is assumed to have 100% transmission over its range of $\Delta\sigma = 500 - 550\ \mathrm{cm^{-1}}$. The radiance of the ambient blackbody, $L_{BB}$, is given by the integral of equation 5.3 over the passband range

$$L_{BB}(T_{BB}) = \int_{500}^{550} L_\sigma d\sigma \qquad \mathrm{W\ m^{-2}\ sr^{-1}} \tag{5.4}$$

If the temperature of the blackbody is taken to be 273 K, which is typical of the temperatures measured at the summit of Mauna Kea, the radiance is 5.8 W $\mathrm{m^{-2}\ sr^{-1}}$.

The total power reaching the detector is found by multiplying the radiance by the throughput of the instrument, $\in$. The throughput is defined as the product of the collecting

area, $A$, and the solid angle, $\Omega$

$$\in = A\Omega \qquad \mathrm{m}^2\ \mathrm{sr} \tag{5.5}$$

The collecting area of IRMA is defined by the radius of the parabolic primary mirror, which was described in § 4.2.2, and is given by

$$A = \frac{\pi}{4}(0.125\ \mathrm{m})^2 = 1.2 \times 10^{-2}\ \ \mathrm{m}^2 \tag{5.6}$$

In the original analysis by Smith [2], the instrumental *field of view* (FOV) was determined by scanning the moon. The analysis showed that IRMA I had a FOV of approximately 0.97°, meaning that it was slightly out of focus since the design called for a FOV of 0.5°. Some effort was made to correct the focus of IRMA II, although no measurements of the corrected FOV were made. However, serendipitously, IRMA II scanned the moon several times between 12PM and 1PM HST on March 20, 2001. These scans, which are shown in figure 5.2, represent a convolution of the instrumental FOV with the moon. The portion of each skydip containing the moon scan was removed including the 'wings' of the profile. To simplify analysis, the profile of the moon was assumed to be Gaussian in shape with a full-width-at-half-maximum (FWHM) of $\sim$0.5°. Since the convolution of two Gaussian profiles produces another Gaussian profile with a FWHM obtained by a quadrature sum of the component FWHM's, the IRMA II beam profile is readily obtained. An IDL® procedure (MOON_ANGLE) was written to extract the FWHM from each scan of the moon and yielded an average value of 0.99° ± 0.06°.

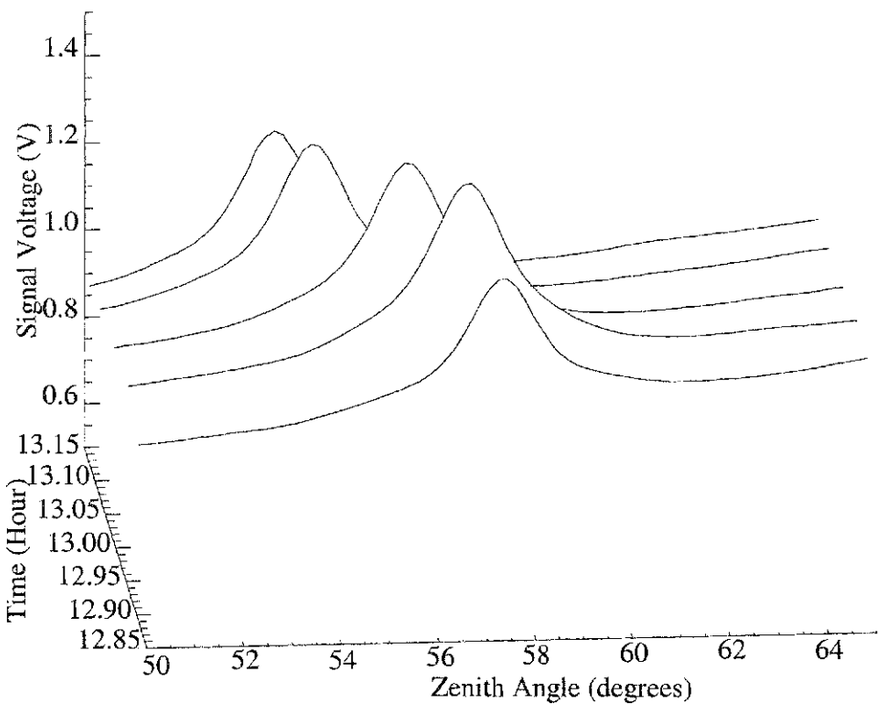


Figure 5.2: Portions of skydips showing serendipitous scans of the Moon.

The instrumental FWHM was determined to be

$$\begin{aligned} FWHM_{inst} &= \sqrt{FWHM_{data}^2 - FWHM_{moon}^2} \\ &= \sqrt{0.99^2 - 0.5^2} = 0.85^\circ = 0.015 \text{ rad} \end{aligned} \tag{5.7}$$

This FWHM can be translated to a solid angle using the equation

$$\begin{aligned} \Omega &= \frac{\pi}{4}\theta^2 \\ &= \frac{\pi}{4}(0.015)^2 = 1.8 \times 10^{-4} \text{ sr} \end{aligned} \tag{5.8}$$

Using equation 5.5 and the values calculated from equations 5.6 and 5.8, the throughput of the radiometer is

$$\in = (1.2 \times 10^{-2}\ \mathrm{m}^2)(1.8 \times 10^{-4}\ \mathrm{sr}) = 2.2 \times 10^{-6}\ \mathrm{m}^2\ \mathrm{sr} \tag{5.9}$$

Finally, the incident power, $\Phi$, can be calculated using equation 5.2 with the radiance, $L_{BB}(T)$, calculated in equation 5.4 and the value of the throughput, $\in$, from equation 5.9. If the radiance is $\sim$5.8 W m$^{-2}$ sr$^{-1}$, then the incident power becomes

$$\Phi = (5.8\ \mathrm{W\ m^{-2}\ sr^{-1}})(2.2 \times 10^{-6}\ \mathrm{m}^2\ \mathrm{sr}) = 1.3 \times 10^{-5}\ \mathrm{W} \tag{5.10}$$

Once average signal voltage and average power are determined, the instrumental responsivity, $R_{inst}$, is found by rearranging equation 5.1 to yield

$$R_{inst} = \frac{V}{\Phi} \quad \mathrm{V\ W^{-1}} \tag{5.11}$$

Using $R_{inst}$, the signal voltages from IRMA can then be converted to radiant power values. The average instrumental responsivity of IRMA was calculated from the data set to be

$$\overline{R_{inst}} = 1.66 \times 10^5\ \mathrm{V\ W^{-1}} \tag{5.12}$$

In this analysis, none of the optical component efficiencies have been included. These efficiencies, however, are not necessary in calibrating the data since the optical train is the same whether IRMA is making an observation of the sky or of its calibration sources and are therefore implicitly included in $R_{inst}$.

## 5.4 Stretch-and-Splice Analysis

As stated in § 2.5, a *curve-of-growth* represents the spectrally integrated emission from an absorbing molecular species as the total amount of that species is varied in a known way. In the case of the atmosphere, varying the amount of water vapour is accomplished by observing the sky at increasing zenith angle, or equivalently, *airmass*. After calibration, the IRMA skydips can be expressed in terms of incident power as a function of airmass. To simplify the analysis it is assumed that the pressure and temperature profiles, and scale height of water vapour above Mauna Kea do not vary significantly from day-to-day, an assumption shown to be valid by the limited variation in the pressure-temperature curves from the Hilo-launched radiosondes (see figure 3.3) . Under these assumptions it is possible to construct a *composite curve-of-growth* from individual skydips by rescaling, or *stretching*, the horizontal axes of the individual scans to reflect the differing amounts of water vapour in the atmosphere at the times of observation. This process is termed *stretch-and-splice.*

The optimum scale factor for a curve was determined by using a numerical minimization technique on the overlap error given by the *chi-squared error*

$$\chi^2 = \frac{\sum[a(i) - b(j)]^2}{N} \tag{5.13}$$

where $a(i)$ are the incident power data of the basis curve, $b(j)$ are the incident power data of the curve being stretched, and $N$ is the number of points in the overlapping region. The summation occurs over the region of overlap of the two curves (i.e. airmass at $a(i)$ = airmass at $b(j)$), which continually changes as one curve is stretched with respect to the other. Using the *AMOEBA* minimization routine of IDL® (which is based on the downhill

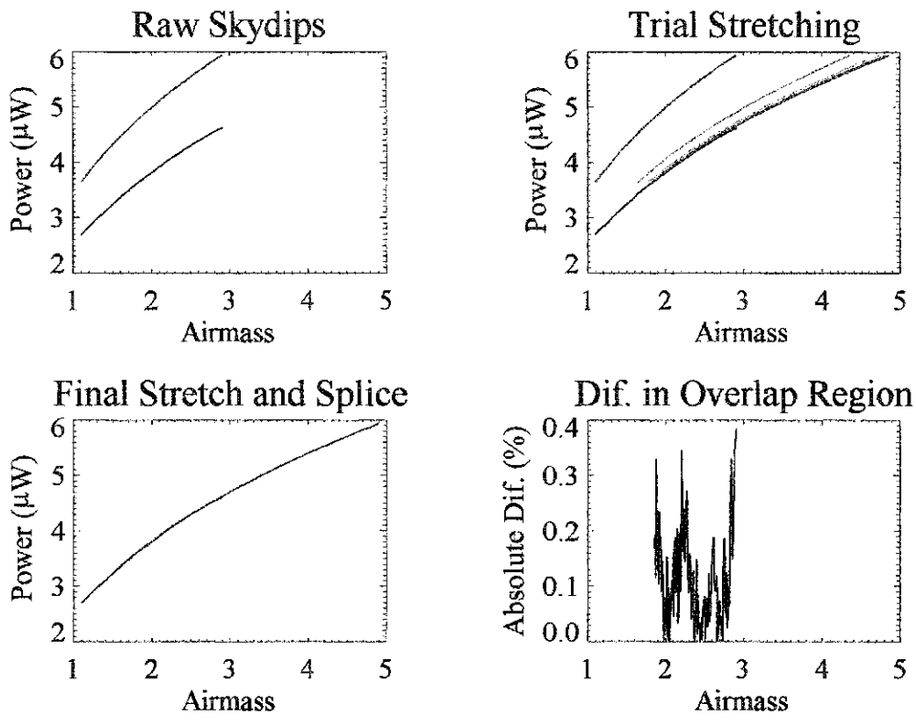


Figure 5.3: Screen shot of the stretch-and-splice routine.

simplex method), the optimum scale factor is found by minimizing the chi-squared error.

The stretch-and-splice procedure is shown graphically in figure 5.3. The upper left panel shows two raw IRMA skydips. In this figure the upper skydip will be stretched to fit with the lower. The upper right panel shows the minimization routine iterating to find the best scale factor. The color of the upper skydip changes with each iteration. The lower left panel shows the upper skydip in the stretched position. The lower right panel shows the absolute percent difference between the skydips in the overlap region.

Before the composite curve-of-growth is constructed, several *basis curves* are cho-

sen from the data set to synthesize a preliminary curve-of-growth, to which all of the skydips will be stretched. This choice is complicated due to the fact that the skydips vary greatly in their incident power measurements. The result of this variation is that skydips with low incident power measurements have either small or no overlapping sections with the skydips with high incident power measurements once they have been stretched.

The stretch-and-splice routine can be used to identify the highest quality skydips in the data set by stretch-and-splicing each curve to all of the rest. Once a skydip is stretched to fit another, the quality of fit is assessed from the $\chi^2$ of the overlapping region. Inspection of the $\chi^2$ measurements showed that the higher quality skydips had $\chi^2 < 2$ when stretched to fit another high quality skydip, so this was chosen as an upper limit for a 'good' stretch. If a skydip was stretched to fit another and its $\chi^2$ was greater than 2, it was considered a poor fit and rejected. If an individual skydip resulted in the rejection of more than a quarter of the total skydips (267), it was not considered as a possible basis curve for the preliminary curve-of-growth. The skydips that rejected the fewest other skydips were inspected, and three of the skydips were chosen to act as basis curves. These basis curves were chosen both for their smoothness (from inspection) and for their positions amongst the remainder of the skydips (one low, one high, and one in the middle of the range), allowing all of the skydips to have large overlaps to perform the fitting routine.

Once the basis curves have been chosen, the stretch-and-splice method is used to synthesize the preliminary curve-of-growth as shown in figure 5.4. First, the middle skydip (shown in green) in figure 5.4 is stretched to fit with the bottom skydip (shown in red). The incident power values of the two curves in the overlapping region are averaged,

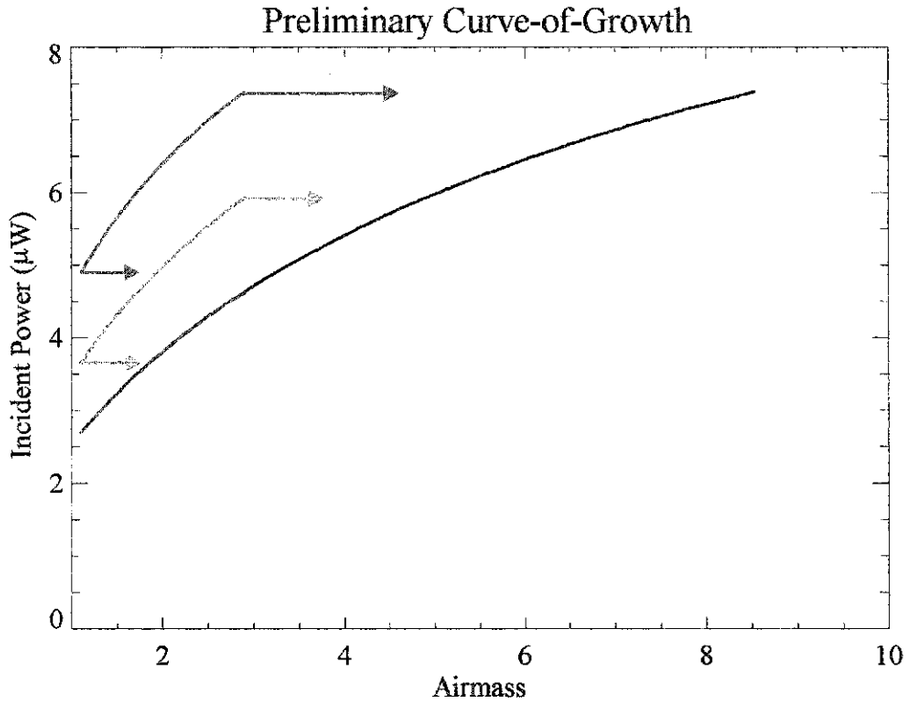


Figure 5.4: Preliminary curve-of-growth and three basis skydips.

splicing the middle skydip to the lower to make the lower portion of the preliminary curve-of-growth. This process is repeated as the top skydip (shown in blue) is stretched to fit with the curve-of-growth. The overlapping incident power values of the curve-of-growth and the top skydip are averaged in the overlapping region, splicing it to the lower portion of the curve-of-growth. This final splicing completes the preliminary curve-of-growth, which is shown as the black curve in figure 5.4.

After the preliminary curve-of-growth is synthesized, all of the skydips in the data set are fitted to the curve using the stretch-and-splice method. The overlapping regions

of the curves are averaged together, producing a mean, *composite* curve-of-growth shown in figure 5.5 as the black curve. A Chebyshev polynomial of degree 6 is then fitted to this composite curve to provide a functional form to the data which is more convenient for comparison with theory. This is shown as the red line in figure 5.5 (displaced vertically by 0.5 $\mu$W for clarity). The green line in the figure shows the difference between the polynomial and the curve-of-growth referred to by the right-hand vertical scale. The low error involved with introducing the Chebyshev polynomial allows its use as a basis curve to determine the final scale factors for individual skydips which are then used to calculate the opacity of the atmosphere for comparison with other instruments.

## 5.5 Comparison With Other Measures of Water Vapour

### 5.5.1 Comparison with SCUBA

The standard calibration procedure for SCUBA [34] uses the skydip method to determine the atmospheric transmission in both the 450 and 850 $\mu$m bands in order to calibrate the flux from an astronomical source. The SCUBA data are analyzed to produce an opacity, or $\tau_{\mathrm{SCUBA}}$ value.

A base opacity for IRMA, or $\tau_{\mathrm{IRMA}}$, is determined by fitting the composite curve-of-growth to an exponential function and taking the value of the exponent as $\tau^{*}_{\mathrm{IRMA}}$. The IRMA skydips are fitted to the composite curve-of-growth as discussed in § 5.4 and the stretch factors, $F$, from the fitting routine are used to determine a $\tau_{\mathrm{IRMA}}$ for the individual

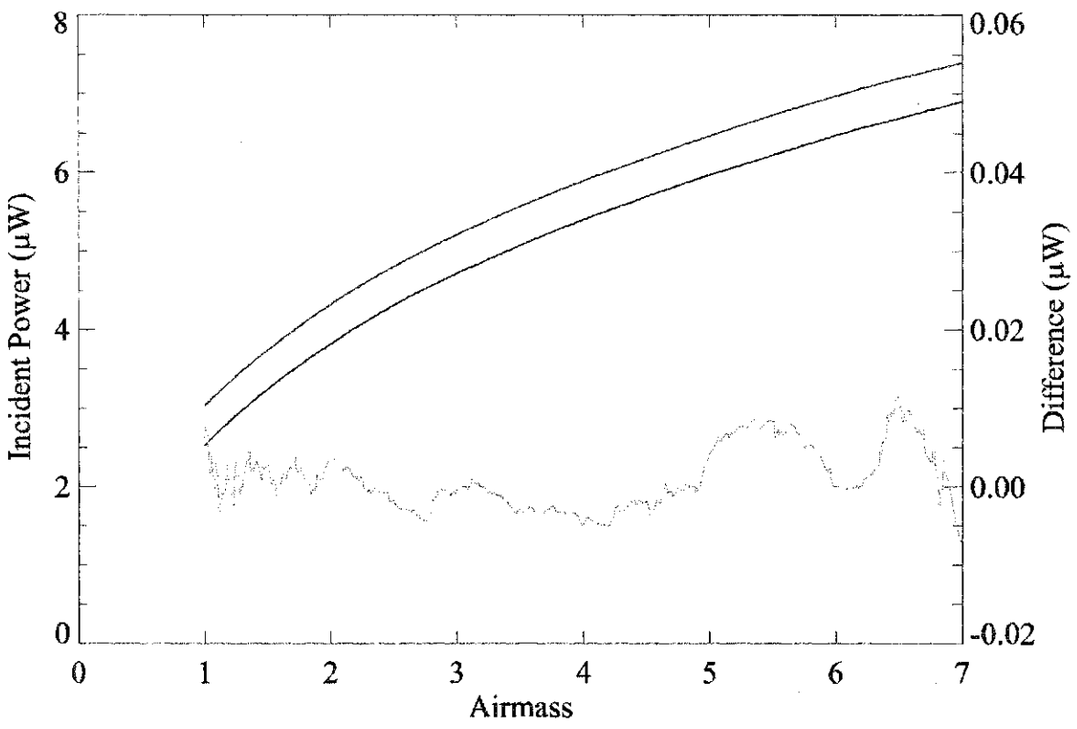


Figure 5.5: Composite curve-of-growth (black) shown with vertically shifted Chebyshev polynomial approximation (red) and the difference between them (green).

skydips using the simple relation

$$\tau_{\mathrm{IRMA}} = \tau^{*}_{\mathrm{IRMA}} \times F \tag{5.14}$$

If both IRMA and SCUBA are measuring water vapour, it is expected that both $\tau$'s are correlated since both instruments perform skydips in essentially the same direction (IRMA is mounted on the carousel floor of the JCMT which generally points in a slightly different azimuth than the telescope).

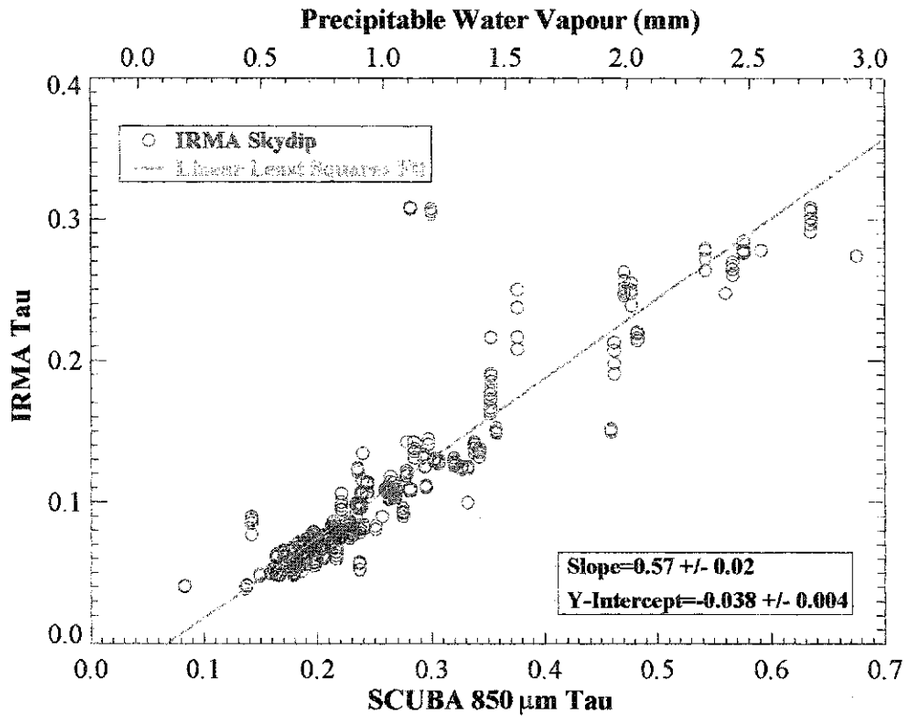


Figure 5.6: Plot of IRMA opacity against corresponding SCUBA 850 $\mu$m opacity.

### IRMA vs. SCUBA 850 $\mu$m

Figure 5.6 shows $\tau_{\mathrm{IRMA}}$ plotted against $\tau_{\mathrm{SCUBA\text{-}850}}$. Each red circle represents the $\tau$ value calculated for a single IRMA skydip. Circles appear in vertical groups because several IRMA skydips can be performed during a single SCUBA skydip. The appearance of columnar grouping in the data indicates that the atmospheric water vapour content is changing appreciably during the time ($\sim$7 minutes) that SCUBA performs a skydip. The linear least squares fit to the data is also shown (green line). Most of the data points are tightly clustered about the line, indicating a high degree of correlation between the

measurements, as expected. The slope of the line shows that the 850 $\mu$m spectral region saturates slightly faster than the infrared region observed by IRMA. The non-zero intercept of the line indicates that water vapour is not the only species responsible for atmospheric opacity in the 850 $\mu$m band. Atmospheric modelling [34] (see figure 3.13) shows this non-zero intercept is to be expected (see top scale) since the 850 $\mu$m region contains numerous ozone and oxygen lines which provide an additional source of opacity not present at 20 $\mu$m.

The $\tau_{\text{SCUBA-850}}$ values can be converted to water vapour column abundances using an atmospheric model [34], and the data in figure 5.6 can be reformulated by rescaling the x-axis, to express the power received by IRMA as a function of water vapour amount (pwv) at the time of observation. This conversion is written as

$$pwv = 20 \times \left( \frac{\tau_{\text{SCUBA-850}}}{4.3} - 0.010 \right) \quad \text{mm} \tag{5.15}$$

After the $\tau_{\text{SCUBA-850}}$ values are converted to water vapour amounts, they can be compared to the zenith power measurements of the corresponding IRMA skydips. Figure 5.7 shows a plot of the precipitable water vapour amounts against the power received by IRMA. Each green triangle in the plot represents a single IRMA skydip corresponding to a pwv measurement made by SCUBA. The triangles appear in columns again because IRMA performs several skydips during the time of a single SCUBA skydip. Included in the figure is the composite curve-of-growth (black), rescaled to fit the data points using a least-squares minimization routine. The horizontal distances from the triangles to the rescaled curve-of-growth are easily measured, and the standard deviation of the distances can be used as a measure of the spread of the data. The red curves in the figure represent

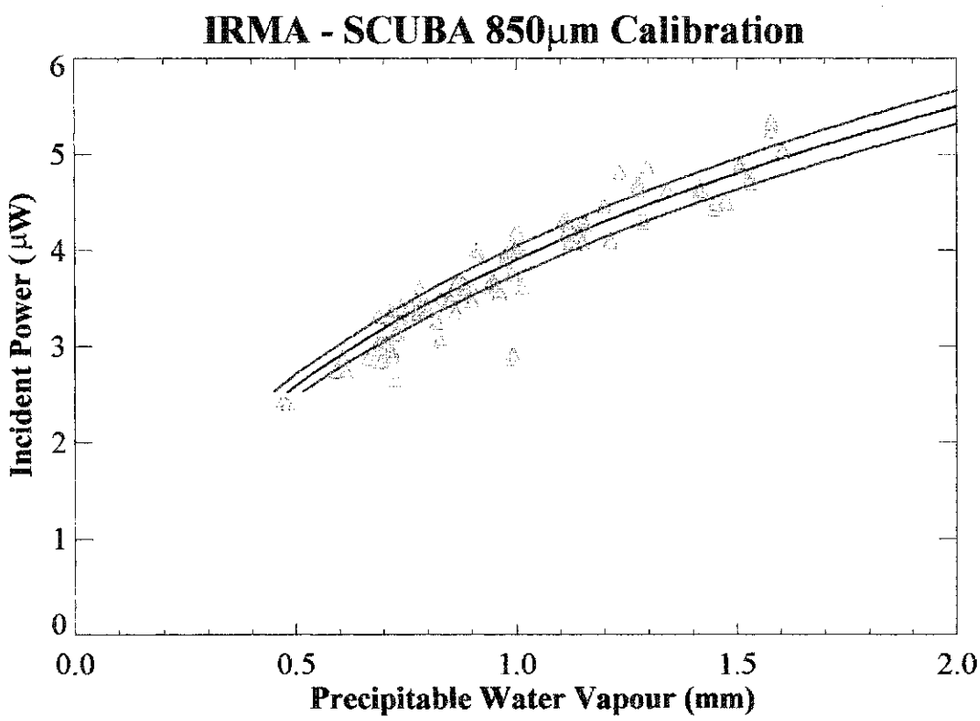


Figure 5.7: The composite curve-of-growth can be reformulated in terms of mm pwv using SCUBA 850 $\mu$m calibration points.

$\pm 1\sigma$ deviations from the curve-of-growth. The small separation of these curves gives an indication of the strong correlation between the IRMA and SCUBA 850 $\mu$m water vapour measurements. The conversion factor relating the airmass and pwv scales from this analysis is determined to be $C_{850} = 0.49 \pm 0.04$.

### IRMA vs SCUBA 450 $\mu$m

Figure 5.8 shows $\tau_{\mathrm{IRMA}}$ plotted against $\tau_{\mathrm{SCUBA\text{-}450}}$. As in figure 5.6, each red circle represents the $\tau$ value calculated for an IRMA skydip. Circles again appear in vertical

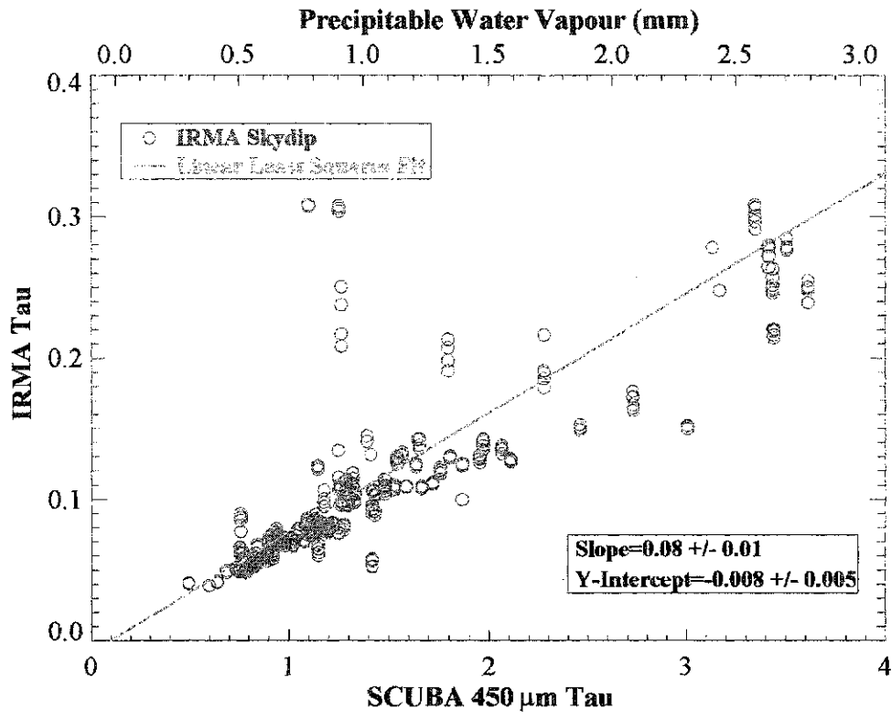


Figure 5.8: Plot of IRMA opacity measurements against corresponding SCUBA 450 $\mu$m opacity measurements.

groups because the atmospheric water vapour content changes appreciably during a single SCUBA skydip. The linear least squares fit to the data is shown (green), and again a high degree of correlation is indicated by the tight clustering of circles about the line. The slope of the line shows that the 450 $\mu$m spectral region saturates much faster than the infrared region observed by IRMA. The small, non-zero intercept of the line indicates that water vapour is the main species responsible for atmospheric opacity in the 450 $\mu$m region (see top scale) with a small amount of opacity due to numerous ozone lines (see figure 3.13). However, this additional opacity due to the stratospheric ozone lines in the 450 $\mu$m region is less significant because the opacity of the tropospheric water vapour is much higher in

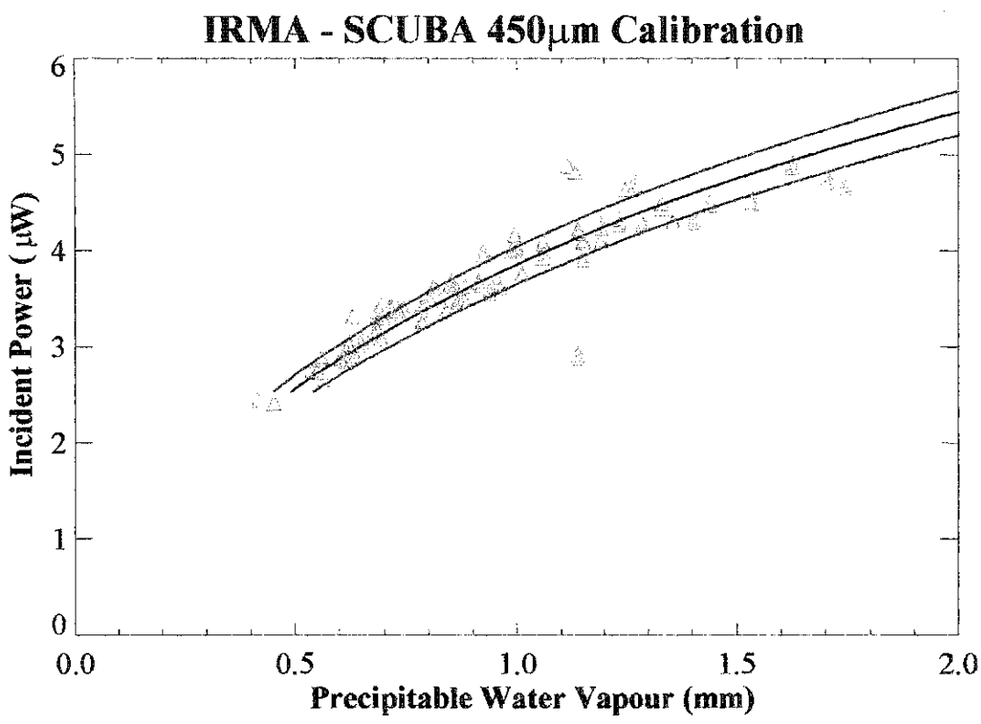


Figure 5.9: The composite curve-of-growth can be reformulated in terms of mm pwv using SCUBA 450 $\mu$m calibration points.

this region.

The $\tau_{\text{SCUBA-450}}$ values can be converted to water vapour column amounts using an atmospheric model [34] in a manner similar to that for the $\tau_{\text{SCUBA-850}}$ values discussed previously. The data in figure 5.8 can be reformulated by rescaling the x-axis to express the power received by the IRMA detector as a function of water vapour (pwv) at the time of observation. The $\tau_{\text{SCUBA-450}}$ values are converted to water vapour amounts using the following equation [34]

$$pwv = 20 \times \left( \frac{\tau_{\text{SCUBA-450}}}{25} - 0.005 \right) \quad \text{mm} \tag{5.16}$$

After the $\tau_{\text{SCUBA-450}}$ values are converted to water vapour amounts, they are plotted against the corresponding zenith power measurements made by IRMA during its skydips. Figure 5.9 shows a plot of precipitable water vapour amount against power received by IRMA. Each green triangle in the figure represents a zenith power measurement made during a single IRMA skydip. The composite curve-of-growth is shown (black), rescaled by applying a least squares minimization routine to fit the data points. The red curves represent $\pm 1\sigma$ deviations from the curve-of-growth. The small spread of the red curves indicates a high degree of correlation between the IRMA and SCUBA 450 $\mu$m water vapour measurements. The conversion factor relating the airmass and pwv scales from this analysis is $C_{450} = 0.50 \pm 0.07$, in excellent agreement with the conversion factor obtained with the 850 $\mu$m measurements.

### 5.5.2 Comparison with CSO Radiometer

The Caltech Submillimeter Observatory (CSO) [35] has two radiometers operating at 225 GHz and 350 $\mu$m, which routinely measure the atmospheric opacity in these bands using the skydip method, albeit at a fixed azimuth direction. The CSO data are analyzed in a similar manner to the SCUBA data to produce opacity or $\tau_{\text{CSO}}$ values in the two spectral regions. Conveniently, $\tau_{\text{CSO-225}}$ values are provided along with the $\tau_{\text{SCUBA}}$ values in the SCUBA calibration files. Although, in general, the CSO radiometers observe a different part of the sky than IRMA, the close proximity of the CSO to the JCMT suggests that $\tau_{\text{IRMA}}$ and $\tau_{\text{CSO}}$ might be correlated.

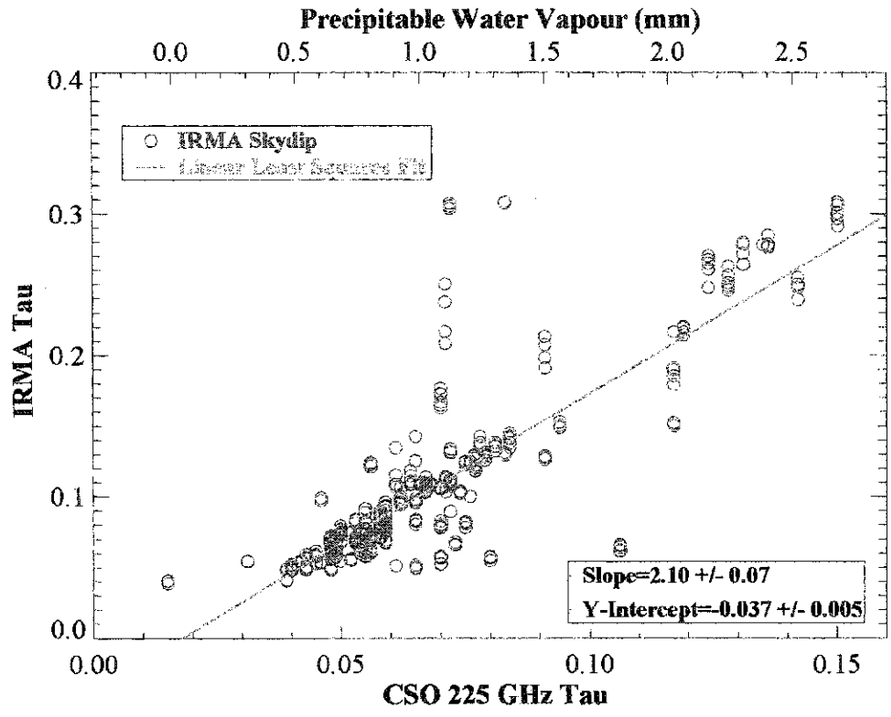


Figure 5.10: Plot of IRMA opacity against corresponding CSO 225 GHz opacity.

### IRMA vs. CSO 225 GHz

Figure 5.10 shows $\tau_{\mathrm{IRMA}}$ plotted against $\tau_{\mathrm{CSO\text{-}225}}$. As with the SCUBA data, there are several IRMA skydips (represented by red circles in the figure) for each CSO measurement. IRMA skydips are associated with a CSO skydip if they take place within a twenty minute period following the CSO skydip. In the figure, the circles again appear in vertical groups because the atmospheric water vapour content changes appreciably during the time of a CSO skydip. The linear least squares fit to the data is also shown (green line). Similar to the previous figures, most of the circles are tightly clustered about the

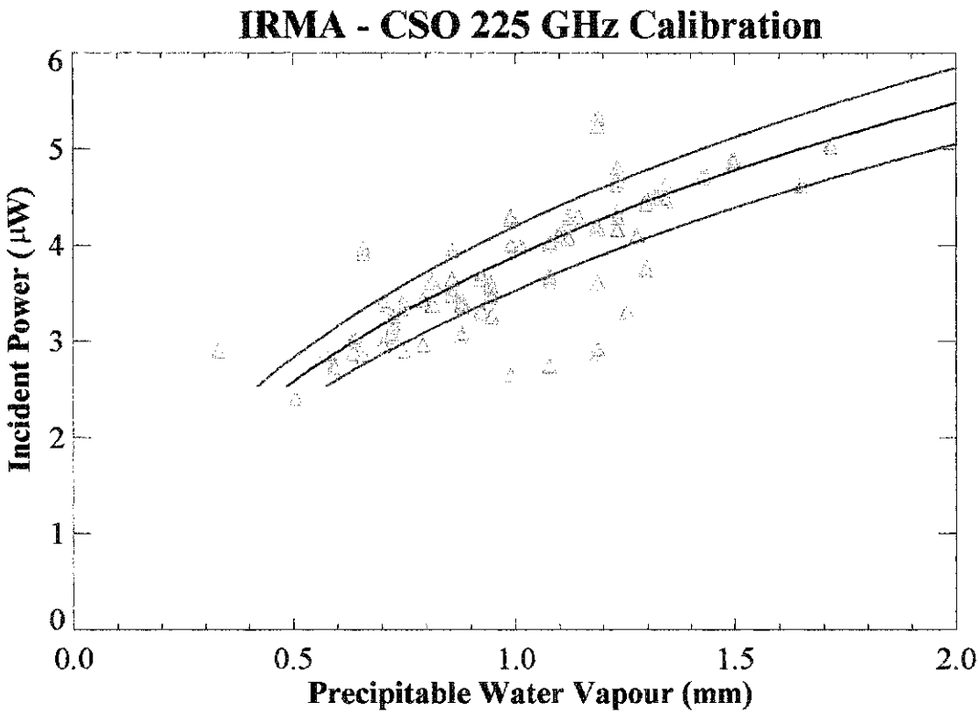


Figure 5.11: The composite curve-of-growth can be reformulated in terms of mm pwv using CSO 225 GHz calibration points.

line, indicating a high degree of correlation between the measures of opacity. However, the correlation between $\tau_{\mathrm{IRMA}}$ and $\tau_{\mathrm{CSO\text{-}225}}$ is less than with SCUBA, which is to be expected since CSO generally observes a different portion of the sky than IRMA. The slope of the line indicates that CSO operates in a spectral region much less opaque than the infrared region. The small, non-zero intercept value indicates that water vapour is the main contributor to opacity in the 225 GHz region (see top scale).

The $\tau_{\mathrm{CSO\text{-}225}}$ values can be converted to water vapour column abundance using an atmospheric model [36]. Figure 5.10 can be reformatted to express the power received

by IRMA as a function of water vapour abundance at the time of observation using

$$pwv = 20 \times (\tau_{\text{CSO-225}} - 0.016) \quad \text{mm} \tag{5.17}$$

as previously discussed. Figure 5.11 (similar to figures 5.7 and 5.9) shows the result of the least squares minimization routine used to rescale the composite curve-of-growth (black) to water vapour abundances derived from the CSO 225 GHz skydips (green triangles). The dashed curves represent $\pm 1\sigma$ deviations from the curve-of-growth, and illustrate a strong correlation between the IRMA and CSO 225 GHz measurements, albeit to a lesser degree than the correlation with SCUBA. The conversion factor relating the airmass and pwv scales from this analysis is $C_{225} = 0.50 \pm 0.07$, which is again seen to be in excellent agreement with the conversion factors found using the SCUBA measurements.

### IRMA vs. CSO 350 $\mu$m

Figure 5.12 shows $\tau_{\text{IRMA}}$ plotted against $\tau_{\text{CSO-350}}$. Again red circles, representing individual IRMA skydips, appear in vertical groups because the atmospheric water vapour content changes appreciably during a CSO skydip. In this figure IRMA skydips are included if they were performed up to 5 minutes after a CSO 350 $\mu$m measurement. The data in this figure show a great deal more scatter than in the previous figures, indicating a low degree of correlation between the measurements of water vapour made by IRMA and those made by CSO 350 $\mu$m. This is primarily due to the high opacity of the 350 $\mu$m band at these water vapour abundances, as indicated by the $\tau_{\text{CSO-350}}$ values.

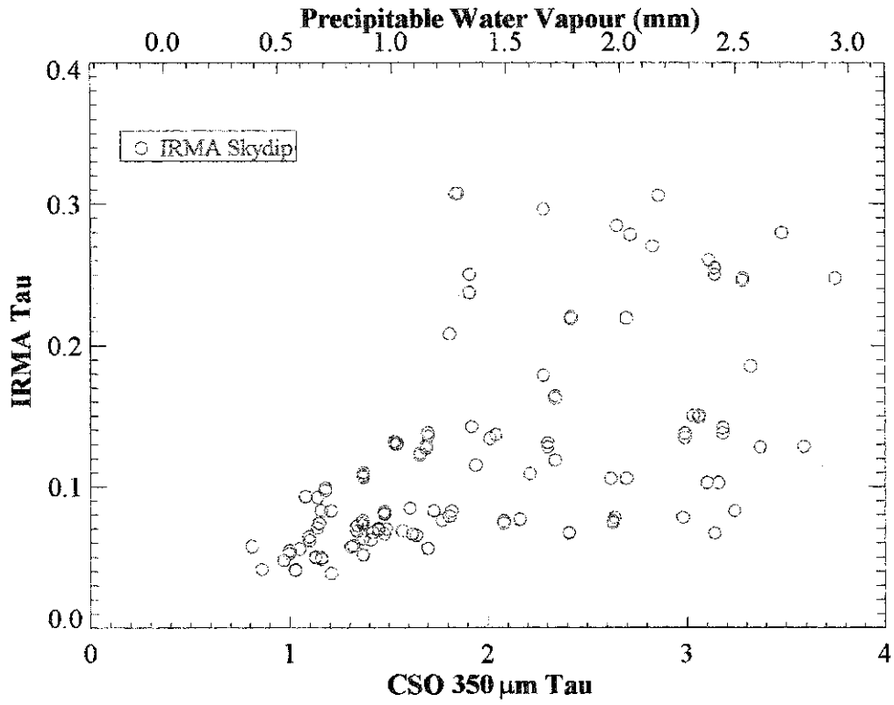


Figure 5.12: Plot of IRMA opacity measurements against corresponding CSO 350 $\mu$m opacity measurements.

The $\tau_{\text{CSO-350}}$ values can be converted to water vapour column abundances using an atmospheric model [37]. The conversion is accomplished using

$$pwv = 20 \times \left(\frac{\tau_{\text{CSO-350}}}{23} - 0.016\right) \quad \text{mm} \tag{5.18}$$

Once the data points are converted, figure 5.12 can be reformulated to express the power received by IRMA as a function of water vapour column abundance (pwv) at the time of observation as was discussed previously. Since the scatter in the CSO 350 $\mu$m data resulted in large uncertainties in the least squares minimization routine, figure 5.13 shows the composite curve-of-growth (black) rescaled by the combined data from SCUBA (850 and 450 $\mu$m) and CSO 225 GHz. The conversion factor from airmass to mm pwv in this

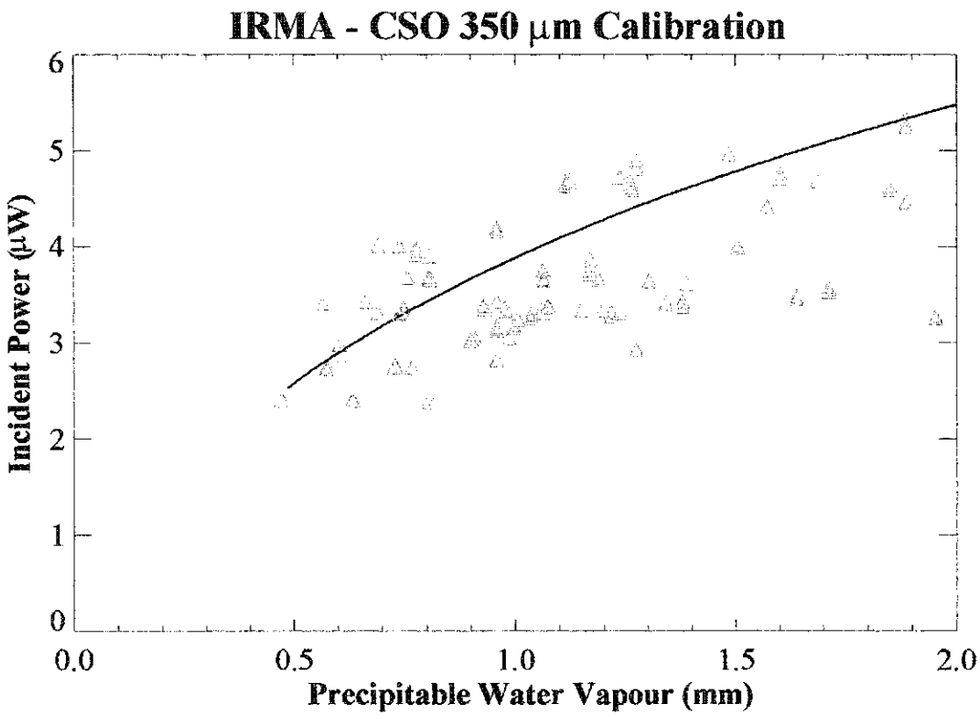


Figure 5.13: CSO 350 $\mu$m data points show a high correlation with the composite curve-of-growth, reformulated in terms of mm pwv using SCUBA 450 and 850 $\mu$m and CSO 225 GHz calibration points.

case is $C_{350} = 0.50 \pm 1.37$. The large error in this conversion factor is due to the large scatter of the CSO 350 $\mu$m data, a result of the inherent difficulties involved in working in this relatively opaque region. The green triangles in the figure represent individual IRMA skydips correlated with pwv measurements from CSO 350 $\mu$m. Even with the large scatter there is a degree of agreement between the water vapour column abundance measurements made by the CSO 350 $\mu$m radiometer and IRMA.

### 5.5.3 Comparison with 183 GHz Water Vapour Meter

A water vapour meter (WVM) radiometer has been developed for operation at the JCMT. This system does not use skydips but, as discussed in § 1.3.1, determines the water vapour abundance along a given line-of-sight from multi-channel radiometric observations of the 183 GHz water line combined with a simple atmospheric model. Although the WVM was not in regular operation between December 2000 and March 2001, some archived WVM data which overlaps with IRMA data is available from the JCMT archive. The WVM data files contain water vapour column abundance measured every 6 seconds and so a figure similar to 5.7 can be produced, expressing the power received by the IRMA detector as a function of water vapour amount (pwv) at the time of observation.

WVM measurements (green triangles in figure 5.14) were compared with an IRMA skydip if they occurred within 1 minute after the start of an IRMA skydip. Triangles appear in horizontal groupings because the atmosphere is changing appreciably during the time of an IRMA skydip. Although there is insufficient data to do a least squares analysis, figure 5.14 shows the composite curve-of-growth (black) rescaled by the average of the SCUBA 850 and 450 $\mu$m and CSO 225 GHz calibration points. The conversion factor in this case is $C_{183} = 0.50 \pm 0.26$. The red curves represent the $\pm 1\sigma$ deviations from the curve-of-growth. The generally poor agreement is interpreted as being due to the statistically small sample size.

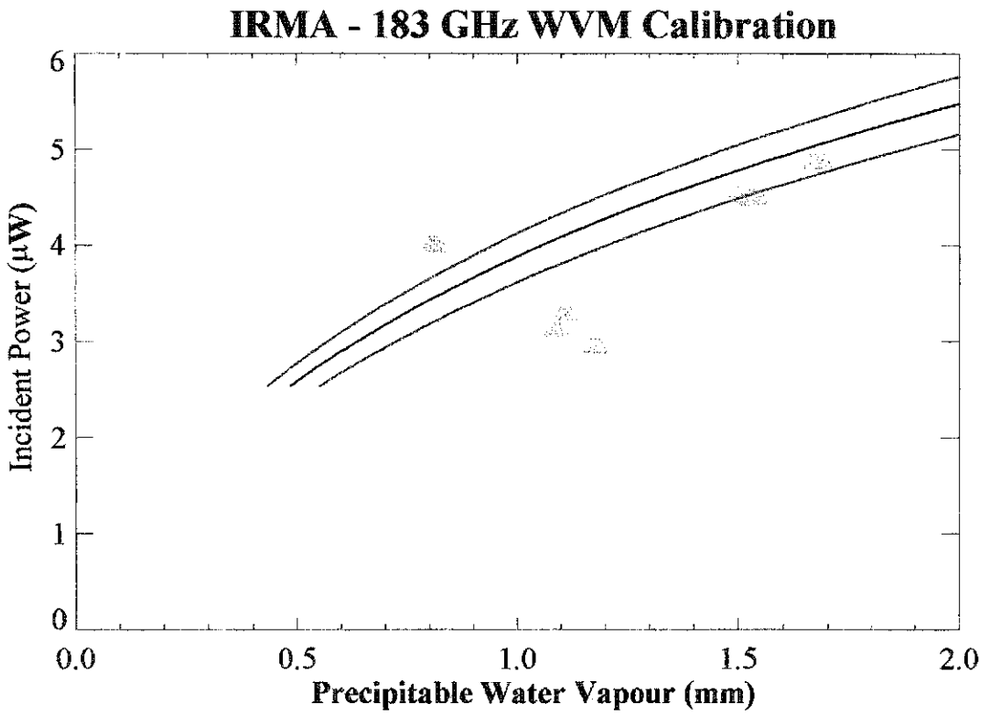


Figure 5.14: There is insufficient 183 GHz data to calibrate the composite curve-of-growth, shown here reformulated in terms of mm pwv using the average of the SCUBA 850 and 450 $\mu$m and CSO 225 GHz calibration points.

### 5.5.4 Comparison with Hilo-Launched Radiosondes

The Hilo airport launches two balloon-borne radiosondes daily (at 0:00 and 12:00 UT), which provide another measure of water vapour in the atmosphere. The correlation between the IRMA and the radiosonde measurements was expected to be low since the radiosondes are launched into a different part of the atmosphere and tend to carry moisture with them as they rise, leading to elevated measurements of water vapour content. Furthermore, the Hilo radiosondes use poor quality humidity sensors that do not perform well at these low pwv amounts. The radiosonde data can be downloaded from

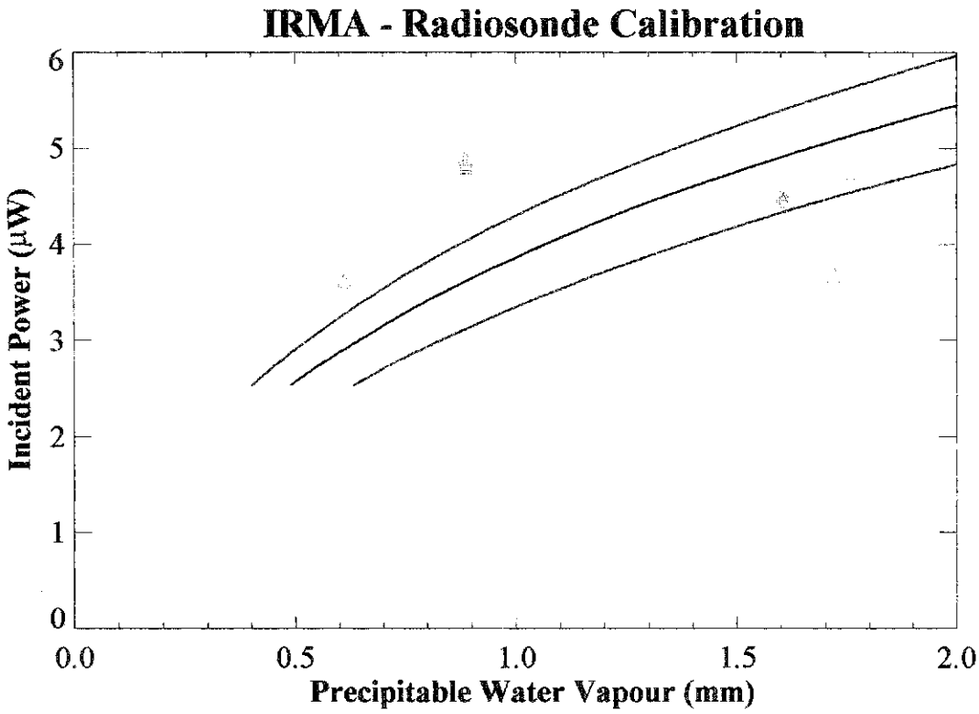


Figure 5.15: There is insufficient radiosonde data to calibrate the composite curve-of-growth, shown here reformulated in terms of mm pwv using the average of the SCUBA 850 and 450 $\mu$m and CSO 225 GHz calibration points.

hokukea.soest.hawaii.edu/current/raob.ito/text and from weather.uwyo.edu/upperair/sounding.html and used to derive water vapour column abundances. From this data, a figure similar to 5.7 can be produced, expressing the power received by the IRMA detector in terms of precipitable water vapour amount.

IRMA scans were compared with the radiosonde data if they were performed within one hour following the launch of a radiosonde. In figure 5.15, which is similar to figure 5.7, IRMA scan data (green triangles) appear in vertical columns because several scans can be performed during the time of a single radiosonde. There was insufficient IRMA data to

| Comparison Instrument | Conversion Factor | Error |
|---|---|---|
| SCUBA 850 $\mu$m | 0.49 | $\pm$0.04 |
| SCUBA 450 $\mu$m | 0.50 | $\pm$0.07 |
| CSO 225 GHz | 0.50 | $\pm$0.07 |
| CSO 350 $\mu$m | *0.50* | $\pm$1.37 |
| 183 GHz WVM | *0.50* | $\pm$0.26 |
| Hilo Radiosondes | *0.50* | $\pm$0.14 |

Table 5.1: Conversion factors for the IRMA curve-of-growth as determined by instrumental zenith pwv measurements.

reliably calibrate the composite curve-of-growth (black), so it was reformulated in terms of precipitable water vapour again using the average of the SCUBA 850 and 450 $\mu$m and CSO 225 GHz calibration factors. In this case, the conversion factor is $C_{\rm radiosonde} = 0.50 \pm 0.14$. The red curves in the figure represent the $\pm 1\sigma$ deviations from the curve-of-growth. There is too little time-matched radiosonde data available to comment on the degree of correlation between the data, but it is possible to say that the radiosonde data are not inconsistent with the IRMA data.

### 5.5.5 Results Summary

Measurements of the column abundance of atmospheric water vapour above Mauna Kea obtained with IRMA show a high degree of correlation with other measures of water vapour available on the summit of Mauna Kea. The results are summarized in table 5.1.

The conversion factors shown in italics represent the average value of the conversion factors calculated using the SCUBA 450 and 850 $\mu$m and CSO GHz calibration points.

As expected, the strongest correlations to IRMA measurements are found with the SCUBA 850 and 450 $\mu$m measures of atmospheric opacity, which are obtained from skydips

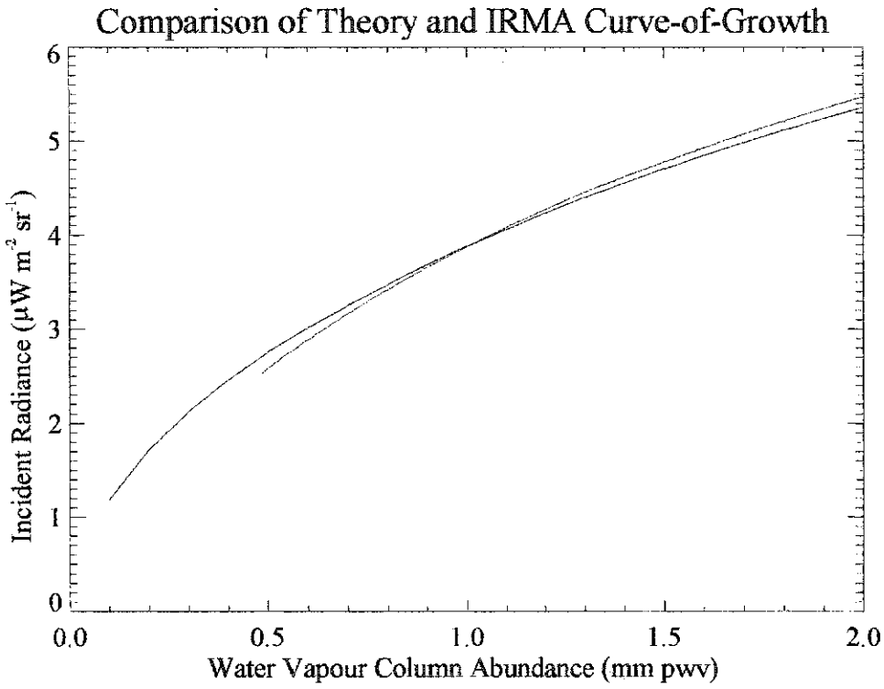


Figure 5.16: A comparison of the theoretical curve-of-growth calculated from ULTRAM (black) with the composite curve-of-growth constructed from IRMA skydips (red).

at approximately the same azimuth angle. The CSO 225 GHz opacity data also show a strong correlation, the increased scatter in these data being attributed to the different azimuth angle of the CSO skydips. The CSO 350 $\mu$m opacity data show a weaker correlation due to the high opacity of the 350 $\mu$m band at these water vapor abundances. While the 183 GHz WVM and Hilo-launched radiosonde data are sparse, they are not inconsistent with the IRMA results.

## 5.6 Comparison of Curve-of-Growth With Theory

The radiance from the mid-infrared data cube produced with ULTRAM was convolved with the filter profile (see § 4.3.2) and then multiplied by the throughput (equation 5.9). The radiance spectra were then integrated with respect to wavenumber to give the total radiance viewed by the detector for increasing water vapour abundances. A theoretical curve-of-growth was plotted from these data, and is shown in figure 5.16 as the black curve. The red curve in the figure is the composite curve-of-growth constructed from IRMA skydips, rescaled from airmass to mm pwv using the conversion factor of $C = 0.50$, calculated from the average of the SCUBA 850 and 450 $\mu$m and CSO 225 GHz calibration factors. The theoretical curve-of-growth in the figure was scaled to the IRMA curve-of-growth at 1 mm pwv by multiplying the radiance by a scale factor of 0.46, indicating that IRMA II has an efficiency of $\eta = 46\%$. This efficiency is much higher than was initially assumed and reflects the simplicity of the radiometer design. The curve-of-growth determined from IRMA data is seen to agree well with the theoretical curve-of-growth. However, a more detailed comparison was not considered meaningful given the uncertainties associated with determining the spectral response of the filter+detector system.

# Chapter 6

# Conclusion

This thesis continues the work begun by a previous graduate student, Mr. Graeme Smith [2], whose work included the design, construction, and field testing of the prototype Infrared Radiometer for Millimeter Astronomy. This thesis presents the analysis of data obtained with the second generation radiometer, IRMA II, and in particular, the development of a radiative transfer modelling program, ULTRAM, which provides a theoretical framework for this analysis.

The results from the measurements IRMA II made from December, 2000 to March 2001 were compared to other measures of water vapour abundance above Mauna Kea. These comparisons showed a high level of correlation between IRMA and the most reliable skydipping instruments on the summit of Mauna Kea. This is illustrated by the similarity in the conversion factor from airmass to mm pwv for the composite curve-of-growth (shown in table 5.1). The data from the less reliable instruments were not inconsistent with the water vapour amounts measured by IRMA.

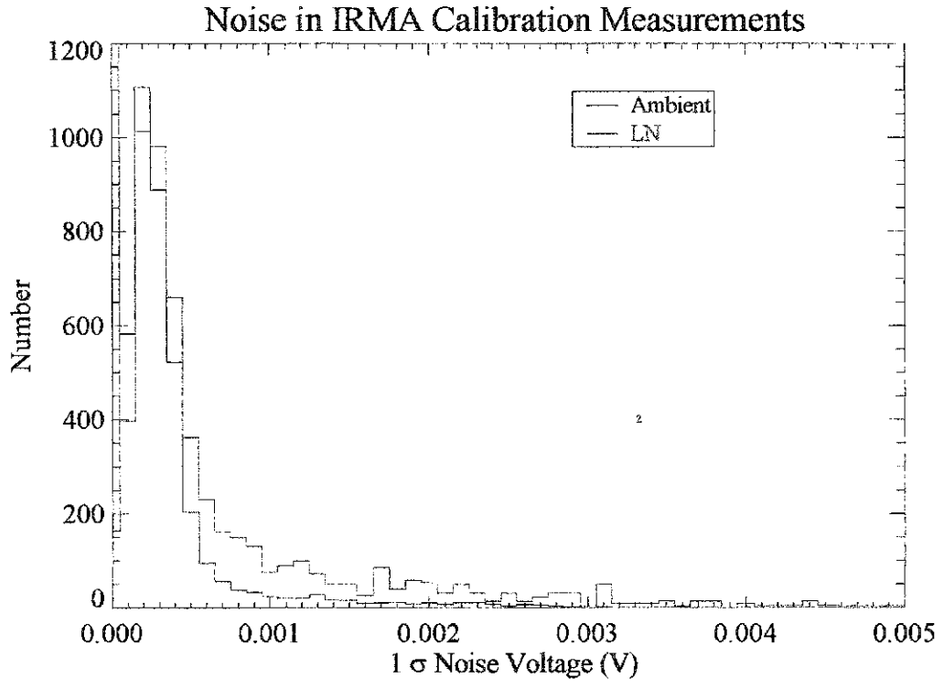


Figure 6.1: Noise from the ambient (black) and $LN_2$ blackbodies (red), determined from the calibration measurements made during IRMA skydips.

ULTRAM was used to calculate a theoretical curve-of-growth to verify the curve-of-growth constructed from the IRMA skydips. Upon rescaling, the theoretical and experimental curves-of-growth were found to show good agreement, from which the optical efficiency of IRMA was found to be $\sim 46\%$.

Measurements of noise, shown in figure 6.1, were made during the IRMA calibration cycles. Noise was defined as the standard deviation of the voltage measured while IRMA viewed its ambient blackbody (black) and its cold blackbody (red). Most of the noise seen in these measurements is below 0.5 mV. Since the noise was measured in a time

interval of 0.1 s, the noise voltage, $\Delta$V, for a 1 second integration is given by

$$\Delta \mathrm{V} = \frac{0.0005 \text{ V}}{\sqrt{10}} = 0.16 \text{ mV} \tag{6.1}$$

The composite curve-of-growth, see § 5.4, was reformulated in terms of volts using the average instrumental responsivity from equation 5.12, and mm pwv using the average of the SCUBA 850 and 450 $\mu$m and CSO 225 GHz calibration factors, $C = 0.50$. An error in the IRMA voltage measurement of $\Delta$V gives an error in the calculated water vapour abundance, $\Delta$pwv, of

$$\Delta\text{pwv} = \frac{1}{\text{slope}} \times \Delta\text{V} \tag{6.2}$$

which can then be reformulated into an error in excess electromagnetic path length, $\Delta d$, using equation 1.5.

The slopes of the curve-of-growth, which is shown in figure 6.2, at 0.5 and 1 mm pwv were determined to be 0.60 and 0.36 V (mm pwv)$^{-1}$ respectively. These slopes allowed the calculation of the resolution of IRMA II in terms of column abundance and excess electromagnetic path length. The results of these calculations are compared with the resolution of IRMA I [2] in tables 6.1 and 6.2. The resolutions achieved by IRMA II show a marked improvement over the previous generation radiometer, and more than meet the phase correction requirements for ALMA.

While the results of this thesis give further credibility to IRMA as a phase correction device for high altitude radio interferometers, there is still vital work to be done. One of the main issues still outstanding is the infrared emission from ice crystals in high

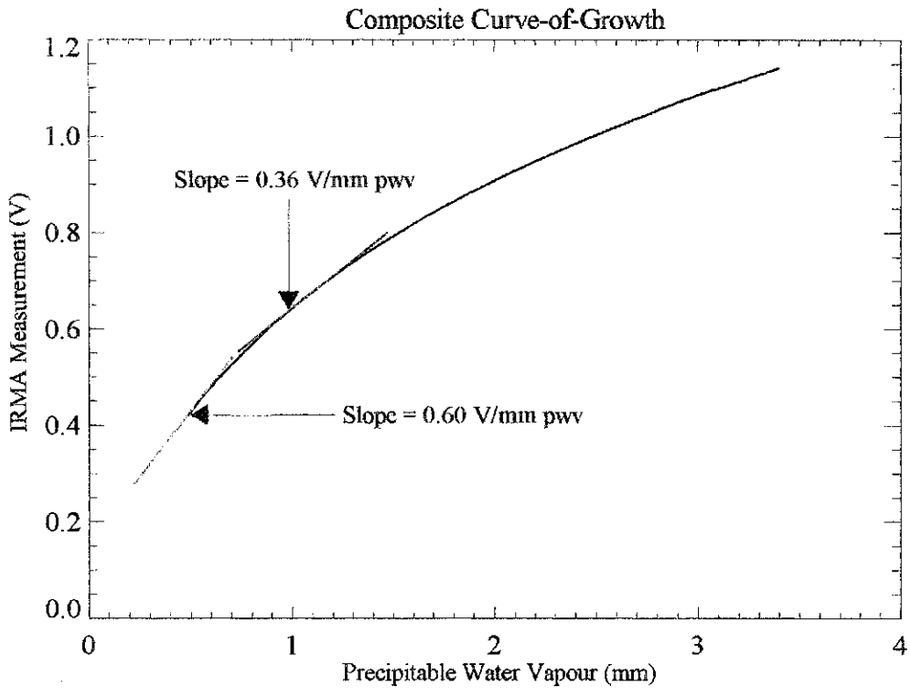


Figure 6.2: The composite curve-of-growth constructed from IRMA skydips (black) and its slope (red), corresponding to an error in measured pwv, at 1 mm pwv.

altitude cirrus clouds. Further investigation into the nature of this emission is required in order to determine the effect of cirrus clouds on IRMA, and how this might in turn affect measurements of water vapour abundances.

The IRMA project continues to be refined with a new version of the instrument, IRMA III, scheduled for testing in 2003. ULTRAM is also a continuing project, with

| | Resolution at 0.5 mm pwv | Resolution at 1.0 mm pwv |
|---|---|---|
| IRMA I | 1.8 $\mu$m | 3.0 $\mu$m |
| IRMA II | 0.26 $\mu$m | 0.44 $\mu$m |

Table 6.1: Comparison of IRMA I and IRMA II water vapour column abundance resolutions at 0.5 and 1.0 mm pwv.

| | Resolution at 0.5 mm pwv | Resolution at 1.0 mm pwv |
|---|---|---|
| IRMA I | 12 $\mu$m | 20 $\mu$m |
| IRMA II | 1.7 $\mu$m | 2.9 $\mu$m |

Table 6.2: Comparison of IRMA I and IRMA II excess electromagnetic path length resolutions at 0.5 and 1.0 mm pwv.

effort being made to model the atmosphere above Chajnantor, to allow us to predict the performance of IRMA III from the Chilean site. These future developments are discussed in this chapter.

## 6.1 Development of IRMA III

The development of IRMA III, the grey box in figure 6.3, has been largely influenced by the desire for site testing at Chajnantor, site of the future ALMA observatory. A number of considerations in the design of the new instrument are due to the remoteness of the location [38].

There is no surplus electrical power available at Chajnantor, so IRMA III must provide its own power using a solar panel array and battery storage. Both IRMA I and IRMA II depended on personnel at the JCMT to fill daily the detector dewar and calibration source with liquid nitrogen. At Chajnantor, the detector, which must operate at 77 K, is cooled by a Stirling cryocooler. By eliminating the need for liquid cryogens, there is no need for personnel to service each IRMA instrument individually. Finally, IRMA III had to be designed to accommodate the hostile environment of the plateau.

Another design consideration of IRMA III arose from a problem which ultimately

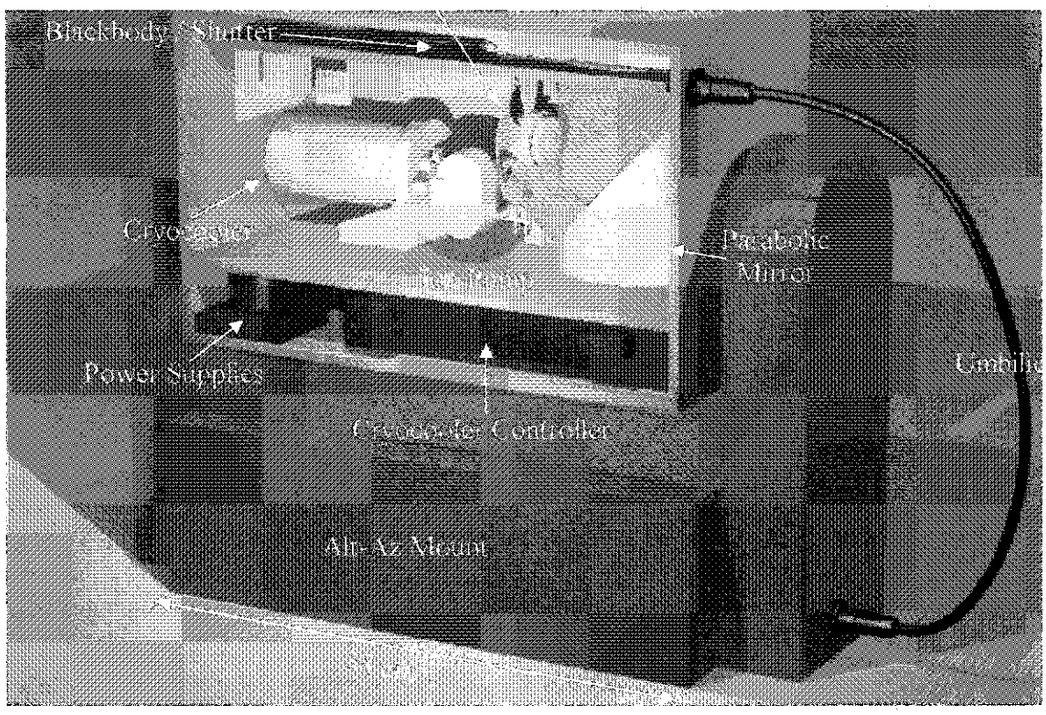


Figure 6.3: Cut-away rendering of IRMA III on alt-az mount, showing the major components.

brought about the end of IRMA II. By chance, IRMA II was made to skydip close to the Sun, focusing an intense beam of light on the filter over the detector. This beam destroyed the filter and rendered IRMA II useless until a repair was effected in June of 2001. Regrettably, shortly after IRMA II was repaired, the instrument again happened to point close to the Sun, again destroying filter and bringing a permanent end to its operation. To avoid the possibility of this happening again, IRMA III is equipped with a shutter mechanism which closes whenever IRMA III points within 5 degrees of the Sun. This shutter also acts as a protection against the harsh environment and acts as a calibration source.

## 6.2 ULTRAM Upgrades

We are in the process of using ULTRAM to generate data cubes similar to those modelled for the atmosphere above Mauna Kea (see §3.5) to model the atmosphere above Chajnantor. ULTRAM will use actual data from radiosondes launched from Chajnantor, to ensure the atmosphere is modelled as close to reality as possible. From these data cubes, and from the design specifications of IRMA III, the performance of IRMA III under various, real atmospheric conditions can be predicted, allowing the design team to evaluate instantly the performance of IRMA III during testing.

The ULTRAM program continues to be refined. A *graphical user interface* (GUI) is being developed to render the program more user-friendly. With the introduction of a GUI to ULTRAM, it will be released to the public via the University of Lethbridge website.

ULTRAM already is finding use in support of operations at the JCMT, Hawaii, the Astronomy Technology Centre (ATC) in Edinburgh as a part of the SCUBA2 project, and at the Rutherford Appleton Laboratory (RAL) as a part of ESA's Herschel SPIRE project.

# Bibliography

[1] D. A. Naylor, R. T. Boreiko, T. A. Clark, R. J. Emery, B. Fitton, and M. F. Kessler, "Atmospheric Emission in the 20-micron Window from Mauna Kea," Publications of the Astronomical Society of the Pacific 96 (1984).

[2] G. J. Smith, *An Infrared Radiometer for Millimeter Astronomy* (Master's Thesis, University of Lethbridge, 2001).

[3] C. L. Carilli and M. A. Holdaway, "MMA Memo 262: Tropospheric Phase Calibration in Millimeter Interferometry," ALMA Memo Series: http://www.alma.nrao.edu/memos/index.html (1999).

[4] M. C. Wiedner, *Atmospheric Water Vapour and Astronomical Millimeter Interferometry* (PhD Thesis, Cambridge, UK, 1998).

[5] G. J. Smith, D. A. Naylor, and P. A. Feldman, "Measurements of Atmospheric Water Vapour Above Mauna Kea Using an Infrared Radiometer," International Journal of Infrared and Millimeter Waves 22 (2001).

[6] E. Hecht, *Optics*, 4th ed. (Addison Wesley, 2002).

[7] C. L. Carilli, O. P. Lay, and E. C. Sutton, "ALMA Memo 210: Radiometric Phase Correction," ALMA Memo Series: http://www.alma.nrao.edu/memos/index.html (1998).

[8] D. Delgado, A. Otarola, V. Belitsky, D. Urbain, R. Hills, and P. Martin-Cocher, "ALMA Memo 271.1: The Determination of Precipitable Water Vapor at Chajnantor from Observations of the 183 GHz Water Line," ALMA Memo Series: http://www.alma.nrao.edu/memos/index.html (1999).

[9] G. P. Anderson *et al.*, "Reviewing Atmospheric Radiative Transfer Modeling: New Developments in High- and Moderate-Resolution FASCODE/FASE and MODTRAN," In *Optical Spectroscopic Techniques and Instrumentation for Atmospheric and Space Research II*, (1996).

[10] "The Interactive Data Language," Research Systems Inc., 4990 Pearl East Circle, Boulder, CO 80301, USA.

[11] J. T. Houghton, *The Physics of Atmospheres, 2nd ed.* (Cambridge University Press, Cambridge, 1986).

[12] W. Hu and S. Dodelson, "Cosmic Microwave Background Anisotropies," Annual Review of Astronomy and Astrophysics 40 (2002).

[13] R. Eisberg and R. Resnick, *Quantum Physics of Atoms, Molecules, Solids, Nuclei, and Particles* (John Wiley and Sons, Inc., 1985).

[14] W. Gordy and R. Cook, *Molecular Spectra, 3rd ed.* (John Wiley and Sons, New York, 1984).

[15] H. J. P. Smith, D. J. Dube, M. E. Gardner, S. A. Clough, F. X. Kneizys, and L. S. Rothman, "FASCODE: Fast Atmospheric Signature Code (Spectral Transmittance and Radiance)," Scientific Report 2, Air Force Geophysics Laboratory, Hanscom AFB, Massachusetts (1978).

[16] "Hitran2000 Spectral Line Database," http://www.hitran.com.

[17] "JPL Spectral Line Catalogue," http://spec.jpl.nasa.gov.

[18] L. S. Rothman *et al.*, "The HITRAN Molecular Spectroscopic Database, 1996 Edition," J. Quant. Spec. Rad. Trans. 60 (1998).

[19] S. D. Lord, "A New Software Tool for Computing Earth's Atmospheric Transmission of Near- and Far-Infrared Radiation," Technical report, National Aeronautics and Space Administration (1992).

[20] E. J. McCartney, *Absorption and Emission by Atmospheric Gases* (John Wiley and Sons, New York, 1983).

[21] J. W. Chamberlain and D. M. Hunten, *Theory of Planetary Atmospheres: An Introduction to Their Physics and Chemistry*, Vol. 36 of *International Geophysics Series*, 2nd ed. (Academic Press Inc., Orlando, 1987).

[22] J. R. Pardo and E. Serabyn, "Calibration Procedures for Planetary Measurements with a Mm/Submm FTS," FTS and ORS Topical Meeting, FMB 2-1, Optical Society of America (2000).

[23] G. B. Rybicki and A. P. Lightman, *Radiative Processes in Astrophysics* (John Wiley and Sons, New York, 1979).

[24] S. A. Clough, F. X. Kneizys, and R. Davies, "Line Shape and the Water Vapor Continuum," Atmospheric Research 23 (1989).

[25] S. A. Clough, "Private Communication".

[26] S. A. Clough, "The Water Vapor Continuum and its Role in Remote Sensing," Optical Remote Sensing of the Atmosphere, OSA Technical Digest Series, Optical Society of America 2 (1995).

[27] L. S. Rothman *et al.*, "The HITRAN Database: 1986 Edition," Applied Optics 26 (1987).

[28] Eccosorb, Emerson and Cuming, 604W 182 St, Gardena, CA 90248, USA.

[29] "Epo-Tek," http://www.promatech.co.uk/prod/epotek.

[30] P. Ade, "Private communication," (2000).

[31] Kolmar Technologies Inc., 1400 E General Arts Rd., Conyers, GA 30012, USA.

[32] D. A. Naylor, I. M. Chapman, and B. G. Gom, "Measurements of Atmospheric Water Vapour Using an Infrared Radiometer," SPIE Proceedings: Annual Meeting, 2002, Atmospheric Radiation Measurements and Applications in Climate 4815 (2002).

[33] W. S. Holland *et al.*, "SCUBA: A Common-User Submillimetre Camera Operating on the James Clerk Maxwell Telescope," Monthly Notices of the Royal Astronomical Society 303 (1999).

[34] E. Archibald, J. Waggs, and T. Jenness, "Calculating Sky Opacities: A Re-Analysis for SCUBA Data," Technical report, Joint Astronomy Centre (2000).

[35] "Caltech Submillimeter Observatory," http://www.submm.caltech.edu/cso/.

[36] G. R. Davis, D. A. Naylor, M. J. Griffin, T. A. Clark, and W. S. Holland, "Broadband Submillimeter Spectroscopy of HCN, $NH_3$ and $PH_3$ in the Troposphere of Jupiter," Icarus 130 (1997).

[37] "The CSO Tau monitor webpage," http://puuoo.submm.caltech.edu/.

[38] D. A. Naylor, B. G. Gom, I. S. Schofield, G. T. Tompkins, and I. M. Chapman, "Remotely Operated Infrared Radiometer for the Measurement of Atmospheric Water Vapour," SPIE Proceedings: Annual Meeting, 2002, Atmospheric Radiation Measurements and Applications in Climate 4815 (2002).